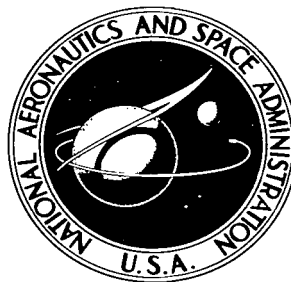


NASA TECHNICAL NOTE



NASA TN D-2303

c.1

LOAN COPY: RETL
AFWL (WLIL);
KIRTLAND AFB, N



NASA TN D-2303

GODDARD SPACE FLIGHT CENTER CONTRIBUTIONS TO THE COSPAR MEETING JUNE 1963

*Goddard Space Flight Center
Greenbelt, Md.*

TECH LIBRARY KAFB, NM



0154959

GODDARD SPACE FLIGHT CENTER
CONTRIBUTIONS TO THE COSPAR MEETING

JUNE 1963

Goddard Space Flight Center
Greenbelt, Maryland

NATIONAL AERONAUTICS AND SPACE ADMINISTRATION

For sale by the Office of Technical Services, Department of Commerce,
Washington, D.C. 20230 -- Price \$2.25

GODDARD SPACE FLIGHT CENTER CONTRIBUTIONS TO THE COSPAR MEETING JUNE 1963

FOREWORD

The Committee on Space Research (COSPAR) held its fourth International Space Science Symposium in June 1963 in Warsaw, Poland. This volume presents a collection of 8 papers co-authored or presented at the meeting by personnel of NASA's Goddard Space Flight Center, Greenbelt, Maryland.

There has been no attempt to arrange the papers in any particular sequence. Their publication within a single NASA Technical Note, rather than as separate ones, was prompted by recognition of the growing need for more inter-disciplinary communication. It is to be hoped, therefore, that readers of any of these papers will find material of interest in all of them.

Technical Information Division
Goddard Space Flight Center
Greenbelt, Maryland

CONTENTS

Foreword	i
"The Atmospheres of Mars, Venus, and Jupiter"	
S. I. Rasool and R. Jastrow	1
"Percentage Cloud Cover from TIROS Photographs"	
A. Arking	23
"An Interpretation of a Rocket Measurement of Electron Density in the Lower Ionosphere"	
A. C. Aikin, Jr., J. A. Kane, and J. Troim	33
"Lifetime and Time Histories of Trapped Radiation Belt Particles"	
W. N. Ness	39
"The Solar Spectrum from 50 Å to 400 Å"	
W. M. Neupert, W. E. Behring and J. C. Lindsay	53
"Emission of Extreme Ultraviolet Radiation from Solar Centers of Activity"	
W. M. Neupert	63
"Preliminary Solar Flare Observations with a Soft X-Ray Spectrometer on the Orbiting Solar Observatory"	
W. E. Behring, W. M. Neupert and J. S. Lindsay	75
"Solar X-Rays: Slow Variations and Transient Events"	
W. A. White	81

THE ATMOSPHERES OF MARS, VENUS, AND JUPITER

by

S. I. Rasool and R. Jastrow

Goddard Institute for Space Studies

SUMMARY

The general properties of the atmospheres of Mars, Venus, and Jupiter are reviewed. The evolutionary processes of planetary atmospheres are outlined as an introduction to a detailed discussion of the structure of the atmospheres of other planets.

The most recent observational results indicate that the surface pressure on Mars may be about 20 mb, and the abundance of CO_2 in the atmosphere of Mars about 25% by volume. For Venus there are indications that the surface pressure is about 100 atm., with the atmosphere mainly composed of N_2 . In the case of Jupiter, recent theoretical investigations of the atmosphere below the clouds suggest that there may be regions in the atmosphere of very high density and pressure but at relatively low temperature, creating conditions possibly favorable to the occurrence of complex organic reactions.

THE STRUCTURE OF A PLANETARY ATMOSPHERE

Composition, temperature and pressure are the three parameters which determine the structure of a planetary atmosphere.

Composition

In order to discuss the composition of a planetary atmosphere, we shall go quite far back into the history of our subject and deal first with the processes by which we believe the planetary atmospheres have evolved. By this approach we can hope to gain an understanding of the conditions which limit the structure and composition of the atmospheres of different planets.

If we assume that the planets condensed from a contracting solar nebula, then the initial composition of the planetary atmospheres would be, in general, governed by the relative abundances of elements in the sun. These are now fairly well known and the abundances compiled by Aller (Reference 1) are plotted in Figure 1.

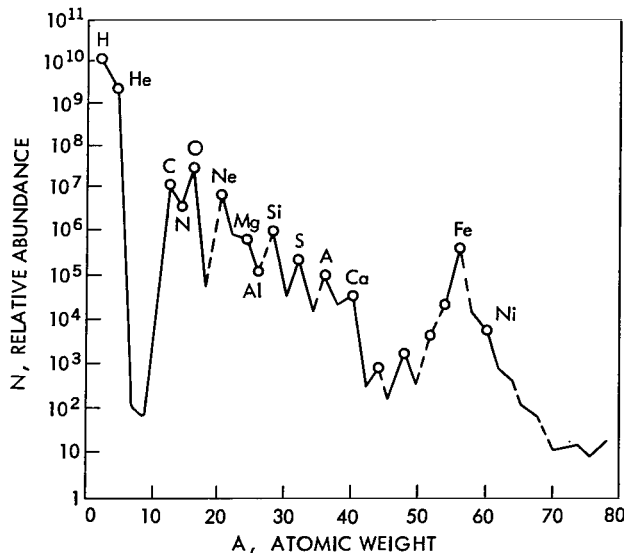


Figure 1—Abundance of the elements in the sun (Reference 1): A is the atomic weight and N is the relative abundance compared to Si = 10^6 .

The peaks in the curve reflect the stability of the respective nuclear species, as is expected for equilibrium concentrations produced by nucleosynthesis. In addition to H and He, the C, N, O group is strong; the Mg, Al, Si group is also strong, with Si the strongest, and Fe is very high. The heavier-than-iron elements fall off rapidly by 3 or more orders of magnitude, with fractional concentrations running about 10^{-9} or 10^{-10} .

These abundances give an indication of the composition to be expected in the contracting cloud which formed the primitive sun. Apart from hydrogen and helium, which should be the most abundant constituents, H_2O , perhaps NH_3 and CH_4 , oxides of C, N, Mg, Si, and Fe, all loosely joined in complex and irregular chains, are expected to form macromolecules and dust

particles. It is presumably aggregates such as these which provided the original material of the planets. On this basis, it is understandable that the composition of the earth should be dominated by silicon oxides plus oxides and carbonates of Mg and Ca.

From these considerations it also seems very probable that the initial composition of the planetary atmospheres will be dominated by H_2 , He, CH_4 , NH_3 , H_2O , CO_2 , N_2 , etc.

Given this primitive composition, the atmospheres will then have evolved through four primary processes:

1. The gravitational escape of gases into the interplanetary space;
2. The exhalation of gases from the interior of the planets;
3. Chemical reactions of gases in the atmosphere with the solid material of the planet; and
4. The photodissociation and ionization of gases by the solar radiation.

Also contributing secondarily are the radioactive decay products and the capture of gaseous constituents from the interplanetary medium.

At any level in an atmosphere a number of atoms and molecules will be moving upward with speeds in excess of that required for escape from the gravitational attraction of this planet. The critical escape velocity, v_c , from a planet is

$$v_c = \sqrt{\frac{2MG}{R}},$$

where M is the mass of the planet, R its radius, and G the universal gravitational constant. For the earth,

$$v_c = 11.3 \text{ km/sec};$$

and for other planets,

$$v_c = 11.3 \sqrt{\frac{M}{R}} \text{ km/sec}$$

where M and R are in units of the earth's mass and radius. For the moon, Mars, Venus, and Jupiter the values of v_c are 2.3, 5.0, 10.4, and 61.0 km/sec, respectively.

The escape of gases can only take place effectively at high altitudes where the density and the probability of collisions are small. These requirements define the region of the atmosphere known as the *exosphere*, a region in which the mean free path for collisions is very large—for a particle moving outward the probability of collision is only one-half. Atmospheric particles in the exosphere therefore execute ballistic trajectories in the gravitational field of the planet.

Knowing the temperature and density at the base of the exosphere, the number of particles can be calculated which will be escaping from the planet per unit time. The classical formula (e.g., Reference 2) for the time of escape t_e in which the density of an atmospheric constituent of molecular or atomic weight ' m ' will fall to e^{-1} of its original value is given by

$$t_e = \left[B(6\pi)^{1/2} \bar{v}/3g \right] \frac{e^y}{y}, \quad (1)$$

where $B = n_o T_o / n_c T_c$, $y = mv_c^2 / 2kT_c$, n_o and T_o are the particle number density and temperature respectively at the ground level, n_c the hypothetical number density at the ground if the whole atmosphere was isothermal at the escape level temperature T_c , \bar{v} the root mean square velocity of the escaping particles, and v_c the velocity of escape.

In the case of the earth, the average temperature of the exosphere has recently been determined to be about 1650°K. For this value of the exospheric temperature, the time of escape of hydrogen from earth is approximately 1000 years. As the age of the planets is about 5 billion years, the absence of hydrogen in the atmosphere of the earth is comprehensible. Gases like CH_4 and NH_3 , which are readily dissociated by solar ultraviolet radiation, would also lose their hydrogen and their relative scarcity in the atmosphere is therefore understandable.

However water is still present on the Earth. Due to the low temperature of the tropopause, almost all the terrestrial water vapor remains confined to the troposphere. The extreme ultraviolet

which can dissociate water vapor does not reach the troposphere because it is being attenuated by ionizing and dissociative processes at the top of the atmosphere. An extremely minute amount of water vapor, corresponding to the saturated vapor pressure of water at 200°K, will traverse the tropopause and will be susceptible to dissociation in the upper atmosphere. This special circumstance preserves the water on the earth.

For helium the time of escape from the earth calculated from Equation 1 will be of the order of 10^7 years. The equilibrium amount of helium in the atmosphere at any time will, however, depend both on the rate of outgassing of helium from the crust and the rate of its escape from the exosphere. Such calculations indicate that the amount of helium in the earth's atmosphere should be higher than observed. This discrepancy is not for the present very well understood (Reference 3).

From the above discussion it is clear that atmospheric constituents of molecular or atomic weight greater than 6 have probably been retained by the earth up to the present time, but, as almost all hydrogen must have escaped, the present atmosphere of the earth should be in a highly oxidized state.

In Figure 2, the times of escape of elements for Earth, Mars and Venus are plotted as a function of their atomic weights.* These calculations have been made on the assumption that the exospheric temperature of Mars is 1100°K (Reference 4) and that of Venus is 2600°K (Reference 5).

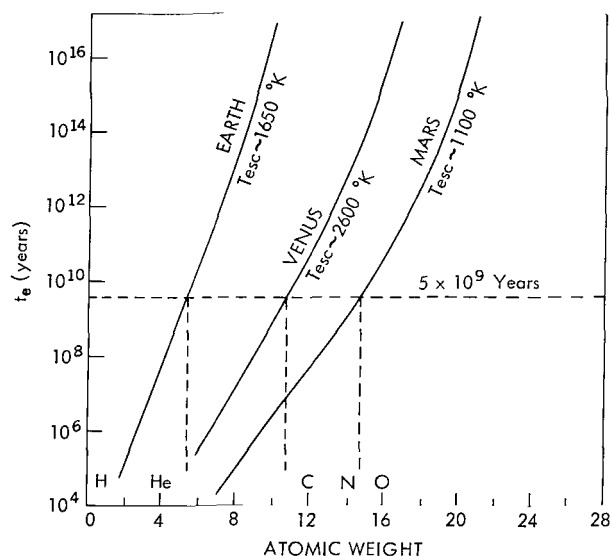


Figure 2—Effective time of escape of gases as a function of atomic weight for Earth, Venus, and Mars.

traces of CO₂, H₂O and argon. However, in the atmosphere of another planet, which may have a similar molecular composition, the relative abundances of these molecules may be entirely

Venus, according to these considerations, must have also lost its hydrogen, while still retaining all the heavier elements. Mars loses its lighter elements at a still faster rate but the escape calculations suggest, however, that some atomic oxygen may have been retained on Mars till the present time.

The curve for Jupiter is not shown in Figure 2, because the time of escape, even for hydrogen, is of the order of 10^{200} years. We therefore expect that the atmosphere of Jupiter and of other giant planets would still have a composition similar to that of the solar atmosphere.

The atmosphere of the earth is composed of 78% nitrogen and 21% oxygen, with only

*Stewart, Private communication, 1963.

different. On the earth the presence of free oxygen is probably a special circumstance which is connected with the presence of life. The CO_2 abundance in the atmosphere is limited by the reaction of the gas with the crust and the formation of carbonates, while the amount of water vapor is extremely sensitive to the temperature environment of the planet.

Therefore, although from the considerations of gravitational escape of gases we may expect the same molecular composition for Mars and Venus, no predictions can be made regarding the relative abundances of these gases in the atmospheres of these planets.

The earth's atmosphere is "mixed" up to the altitude of 90 km, and therefore on an average the composition does not vary as a function of height. The mean molecular weight is approximately 29, and the total pressure at the surface is 10^6 dynes/cm². The number density at the ground is 2×10^{19} molecules/cm³.

For an isothermal atmosphere in hydrostatic equilibrium, the variation of density with height is given by the formula

$$\rho = \rho_0 e^{-(h-h_0)mg/kT},$$

where ρ and ρ_0 are the densities at height h and h_0 , m is the average molecular weight per particle, T the temperature between h and h_0 , g the acceleration of gravity, and k Boltzmann's constant.

The quantity kT/mg is the scale height H of the isothermal atmosphere; at an altitude of one scale height the density is reduced by a factor of e . For a mean temperature of 250°K in the first 80 km of the atmosphere, the atmospheric scale height is approximately 8 km.

Above 120 km the diffusive separation sets in and the pressure of each constituent varies in accordance with the scale height calculated for its own molecular weight. Figure 3 shows the change in composition in the earth's atmosphere with altitude as deduced from the recent experimental results obtained by means of satellites.

For Mars, Venus, and Jupiter, we expect the lower atmospheres to be mixed also while the upper atmospheres of these planets will be in diffusive equilibrium; the major constituent of the atmosphere at the extremity will, in each case, be hydrogen.

Temperature

The temperature of a planet depends on its distance from the sun. In the case of the earth, the solar radiation flux, reaching the

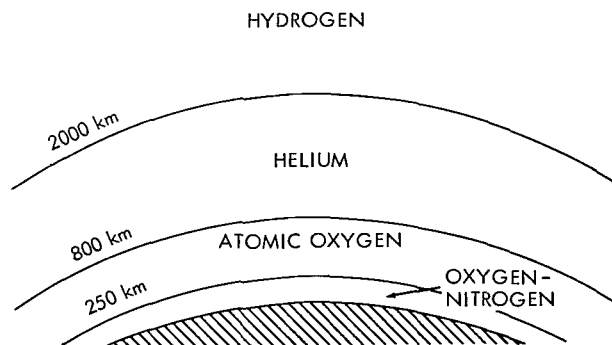


Figure 3—Composition of the upper atmosphere of Earth.

top of the earth's atmosphere has a value of about 1.4×10^6 ergs/cm²-sec. Part of this radiation (39%) is immediately "reflected" back to space by clouds and the atmosphere and does not play any role in the energy balance of the planet. Most of the remaining 61% of the solar radiation, mainly composed of the visible part of the spectrum, penetrates down to the ground and heats the surface to a certain temperature denoted as T_e , the effective temperature of the planet. In the case of rapidly rotating planets (e.g., Earth, Mars, Jupiter),

$$T_e^4 = \frac{SC}{4\sigma} (1 - A) ,$$

where SC is the solar constant or the radiation flux received at the top of the atmosphere, and A is the albedo of the planet over the whole solar spectrum. For the values of SC and albedo given above, the T_e for earth is 245°K.

The surface radiating at this relatively low temperature emits primarily in the far infrared. A large fraction of the radiation emitted by the surface is immediately absorbed by molecules of CO₂ and H₂O present in the lower layers of the earth's atmosphere. A part of this absorbed energy in the infrared is returned to the surface and provides extensive heating of the ground, raising the surface temperature to the observed value of approximately 290°K.

This additional heating of the surface (about 45°K) by the return of infrared radiation from the atmosphere is referred to as the "greenhouse effect" and is an essential element in understanding the radiation budget of the planet.

The magnitude of the "greenhouse effect" caused by a planetary atmosphere can be estimated by approximating the solution to the radiative transfer equation. The ground temperature T_g is then given by the equation

$$T_g^4 = T_e^4 (1 + 3/4 \tau) \quad (2)$$

where T_e is the effective black body temperature of the planet and τ is the total optical thickness of the atmosphere in the infrared. This solution is based on the assumption that the atmosphere is in radiative equilibrium. In the case of earth for the observed value of average ground temperature of 300°K, the total optical thickness of the atmosphere from Equation 2 is about 1.7 which corresponds to the infrared absorption of about 82%. It is fairly well known that the amount of water vapor and the CO₂ in the earth's atmosphere do actually have an average opacity of about 80% over the entire infrared spectrum.

In Table 1 the values of the effective black body temperatures are given for other planets and also the most reliable values of the observed surface temperatures. In the case of Jupiter, T_g is the cloud top temperature and for that reason the factor $(1 + 3/4 \tau)$ in Equation 2 becomes $(1/2 + 3/4 \tau)$. The differences give the magnitude of the greenhouse effect for each planet which in turn provide an estimate of the optical thickness of the atmosphere in the infrared.

On Mars the greenhouse effect is very small which gives an optical thickness of the atmosphere of only 0.6, indicating that the atmosphere is optically thin; therefore, we do not expect excessively large amounts of polyatomic gases like H_2O , CO_2 , etc., which have intense absorption bands in the far infrared. On the other hand, for Venus, the magnitude of the greenhouse effect is extremely large compared to the earth or

Mars, and the atmosphere must be almost completely opaque to the far infrared radiation from the planet. Large amounts of polyatomic gases should be abundant on Venus.

The atmosphere of Jupiter above the clouds should have an optical thickness of approximately 2.4 in order to explain the cloud top temperature of $130^\circ K$. Therefore we expect polyatomic gases, which absorb in the far infrared, at wavelengths greater than 20μ where most of the planetary radiation will be confined.

With these considerations in mind, we now turn to the observed properties of the atmospheres of these planets.

MARS

The reliable physical data for Mars can be summarized as follows:

Mean Distance from sun	1.52 AU
Mean Equatorial diameter	6790 km
Length of day	1.0012 earth day
Length of year	1.8808 earth year
Mass	0.1078 (earth = 1)
Mean Density	3.90 gm/cm^3
Gravity	377 cm/sec^2
Total integrated albedo	0.26
Effective black body temperature	$209^\circ K$

Composition and Surface Pressure

The only gases that have been, up to now, spectroscopically detected in the atmosphere of Mars are carbon dioxide and water vapor. Their abundances have been estimated by several authors, but generally accepted values of the amounts of these gases in the atmosphere of Mars are not yet available. The best estimates, at the present time, vary within the following ranges:

$$CO_2 = 70 \pm 30 \text{ m-atm}^*$$

*L. D. Kaplan, Private communication, 1963.

Table 1
Greenhouse Effect on Planets

Planet	T_e (°K)	T_G (°K)	$T_{(Greenhouse)}$ (°K)	Optical Thickness of Atmosphere in the Infrared
Mars	209	230	21	0.6
Earth	245	300	55	1.7
Venus	235	600	365	55.4
Jupiter	105	130	25	2.4

Precipitable water vapor = $10^{-3} - 10^{-2}$ gm/cm² (References 6 and 7),

where m-atm is the thickness of a homogeneous atmosphere in meters at normal temperature and pressure, 0°C and 760 mm.

The search for the presence of other gases in the atmosphere of Mars has failed to give positive results. The upper limits on their possible abundances are presented in Table 2.

Earlier photometric studies by de Vaucouleurs (Reference 8) and polarimetric measurements by Dollfus (Reference 9) had given consistent estimates of the surface pressure on Mars as 85 ± 10 mb. Recently, however, from the analysis of the pressure-dependent absorption bands of CO₂ observed in the Martian atmosphere*, it has been suggested that the total pressure at the surface of Mars may be as low as 20 ± 10 mb. If this value is taken to be correct, then CO₂ will make up for about 25% of the total atmosphere.

The probable composition of the Martian atmosphere is presented in Table 3. This atmosphere has a mean molecular weight of 32. With a surface pressure of 20 mb and an approximate temperature of 210°K, the surface density would be approximately 5×10^{17} particles/cm³ which, for an isothermal atmosphere, should decrease exponentially with altitude with a scale height of 14.5 km. The vertical distribution of pressure for this model is shown in Figure 4. Results of a similar computation for earth, assuming an isothermal atmosphere at 250°K, are also shown in Figure 4. It is interesting to note that although the pressure at the surface of Mars is about 1/50 of the earth's, at an altitude of approximately 50 km the two atmospheres have the same pressure, and above this height the pressure in the Martian atmosphere is greater than the pressure at the corresponding height in the earth's atmosphere. Because the decrease of density with height of Mars is almost two times slower than in the earth, the levels of the ionosphere and thermosphere on Mars would be much higher than on the earth.

*L. D. Kaplan, Private communication, 1963.

Table 2
Trace Constituents on Mars

Gas	Upper Limit of Abundance (m-atm)
O ₂	< 2.4
N ₂ O, NO ₂ or N ₂ O ₄	< 2.0
NH ₃	< 0.2
CH ₄	< 0.1
O ₃	< 5×10^{-4}
SO ₂	< 3×10^{-5}

Table 3
Probable Composition of Martian Atmosphere

Gas	Volume (Percentage)
N ₂	72
CO ₂	25
A	2
O ₂	< 0.5
H ₂ O	very small

Temperature

Planetary temperatures are usually estimated by measuring the infrared radiation emitted by the planet. A large part of the infrared spectrum is, however, absorbed by the water vapor and CO₂ present in the earth's atmosphere. Ground based observations of the planets in the infrared are therefore confined to the 8-12 μ region where the earth's atmosphere is relatively transparent. This spectral region in the infrared is known as the atmospheric "window".

Extensive temperature measurements of Mars by infrared radiometry in this window of the terrestrial atmosphere have been made since 1926, and the results to date are quite consistent. Since the Martian atmosphere should also be largely transparent in the 8-12 μ window, it is assumed that the radiation intensity measurements in this wavelength region refer to the surface of the planet.

Some of the earlier investigators were also able to scan the planetary disc latitudinally and longitudinally so as to obtain the diurnal and seasonal variation of temperature as a function of latitude. The up-to-date information can be summarized as follows:

Maximum temperature at equator	~300°K
Mean amplitude of diurnal variation	~ 60°K
noon to sunset (on earth in desert)	~ 30°K
Night side temperature cannot be measured but can probably be estimated at the equator	~200°K
Day side temperature at poles	~220°K
Mean temperature of day side	~260°K
Mean temperature of whole planet	~230°K

Surface Features

As seen by telescope the outstanding features of Mars are (1) the dark areas (maria), (2) the general reddish-orange background ("deserts"), and (3) the polar caps.

The nature of the dark maria is not very well understood because, apart from showing fairly regular seasonal changes, they are also subject to erratic variations which make the hypothesis of earth-type vegetation somewhat doubtful. Moreover, the infrared spectrum does not have

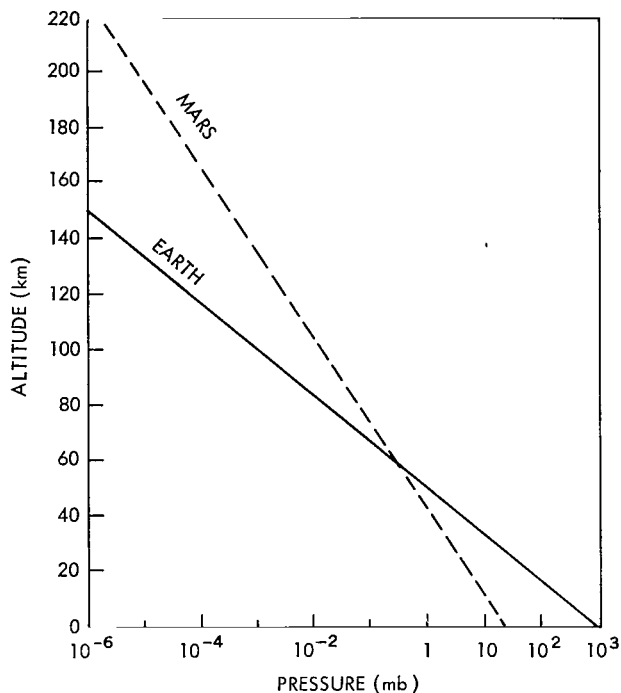


Figure 4—Pressure vs. altitude for Earth and Mars. (Martian surface pressure about 20 mb, atmospheric scale height = 14.5 km.)

characteristic absorption bands of chlorophyll. The presence of organic material in these regions has, however, been reported by Sinton (Reference 10) who detected C-H vibration absorptions in the 3.5μ region which were absent in the reflection spectrum of the desert areas.

The probability of the existence of life on Mars is controversial and beyond the scope of this review; but it will be desirable to see the observations of C-H bands on Mars repeated and probably substantiated by infrared spectroscopic measurements of the terrestrial "dark and bright" areas from an earth satellite.

The large orange areas of Mars are responsible for the reddish color of the planet seen by the naked eye. According to Kuiper (Reference 11) they are composed of felsitic rhyolite.

The polar caps are rather reliably known to be a layer of H_2O frost a few centimeters thick deposited on the surface. These caps are observed to expand to lower latitudes during fall and winter and to recede to high latitudes during spring and summer. The observed evaporation of the polar caps in summer and the almost immediate transport of the water vapor towards the winter pole across the equator is a special meteorological phenomenon peculiar to Mars. In the earth's atmosphere the hemisphere to hemisphere mixing is extremely small. The average speed of this "humidity wave" across the planet has been estimated to be about 45 km/day. This pole to pole circulation can perhaps only be understood by the greater length of the Martian year and the increased temperature differences between the cold and warm poles. In the summer the pole is the warmest region on the planet.

Blue Haze Layer

Photographs of Mars taken through blue filters indicate no surface features, and it is therefore believed to be covered with a haze layer known as "blue haze", absorbing at these wavelengths. Sometimes during the opposition, however, it clears over certain regions, and surface features become observable in the blue. These "blue clearings" last usually a few days. Conflicting arguments have been advanced to explain the nature of the blue haze, but an explanation which satisfies all the observed features is yet to be found.

Clouds

Several types of thin clouds have been frequently observed on Mars. They can be divided into three types:

Blue clouds are visible only in blue light. They appear in patches near the poles and the terminator. Polarization measurements indicate their particle size to be approximately 0.1μ . They probably occur at altitudes less than 100 km. According to Goody (Reference 12), they may be composed of ice crystals formed on the nuclei fed by the haze layer, while others believe them to be of the same material as the blue haze.

White clouds are visible both in blue and yellow light. The polarization studies of these clouds suggest their nature to be the same as ice crystal clouds of a particle size of about 1μ . Being composed of larger particles, they probably lie at lower altitudes than the blue clouds.

Yellow clouds visible only in yellow, are very rare and variable in size. They have been seen drifting several hundred miles across the planet at a velocity of 60 km/hr. According to Goody (Reference 12), they are composed of the same blue absorbing material as the blue haze. Hess (Reference 13) estimates their height to be approximately 5 or 6 km.

Vertical Distribution of Temperature

The atmosphere of Mars is optically thin in the infrared, and the probable absorbing gases are CO_2 and H_2O , which are also present in the earth's atmosphere. The vertical temperature profile in the atmosphere of Mars, therefore, cannot be determined by observation from the surface of the earth. Only theoretical estimates exist for the vertical temperature structure of Mars. The most recent computations of this nature are by Arking, Ohring, and Chamberlain (References 14, 15, and 4, respectively).

Arking has calculated a model atmosphere for Mars, allowing for convection and using the exact equation of radiative transfer for frequency independent absorption. A total optical thickness of 0.5 was chosen to obtain a surface temperature of 235°K , consistent with the observed mean surface temperature. Assuming an effective black body temperature of 217°K , an adiabatic gradient of -3.7°K/km in the convection zone and an exponential dependence of absorption on altitude with a scale height of 17 km, the temperature profile shown in Figure 4 (insert) is obtained. The convection zone is found to extend up to 8 km.

Ohring also has recently investigated the vertical temperature profile for a model Martian atmosphere containing 2% CO_2 , 98% N_2 and no water vapor. The ground temperature was assumed to be 230°K and the transfer of radiation in the atmosphere was calculated for frequency dependent absorption by the CO_2 . The tropopause in this case was found to be at 9 km at a temperature of 196°K . In the stratosphere the temperature keeps on decreasing to a value of as low as 90°K at an altitude of 42 km, where the total pressure is 2.5 mb.

Now that the mixing ratio of CO_2 in the Martian atmosphere is known to be much higher, new calculations for a "non-grey" atmosphere are desirable.

The above mentioned results of the temperature distributions in the Martian atmosphere do not take into account possible heating of the lower atmosphere by direct absorption of solar radiation in the ultraviolet. In the case of the terrestrial atmosphere, the ozone heating produces a temperature maximum at 50 km, but on Mars, with much less oxygen compared to earth, ozone would be confined to lower layers of the atmosphere. The solar radiation in the region of 2500 Å, responsible for ozone dissociation and atmospheric heating, will therefore penetrate to a much lower depth in the Martian atmosphere. Due to a higher atmospheric density at this level (compared to the density in the earth's atmosphere at 50 km) and because of the lower intensity of the

solar radiation at the distance of Mars, the heating rates will probably not be as important as in the ozonosphere on earth. Still they may affect the temperature gradients substantially and limit the extent of the convection zone.

Assuming an atmospheric composition of 98% N_2 and 2% CO_2 , and a Martian stratospheric temperature of 134°K (Reference 12), Chamberlain (Reference 4) recently computed the mesospheric cooling and thermospheric heating for Mars. With the assumed model atmosphere and from the considerations of CO_2 dissociation into CO and O and the consequent CO cooling at the mesopause, Chamberlain deduces the height of the mesopause as about 130 km at a temperature of 76°K. The considerable CO cooling at the mesopause level acts as "an effective thermostat, keeping the temperature at the exospheric or escape level (1500 km) from exceeding 1100°K."

Figure 5 shows the vertical distribution of temperature in the Martian atmosphere. The temperatures up to an altitude of 100 km are based on the results obtained by Arking. Above this altitude, the upper atmospheric model developed by Chamberlain has been used.

VENUS

Venus is our nearest planetary neighbor and, after the sun and moon, the brightest object in the sky. It has therefore attracted the attention of man since the beginning of civilization. Despite the great interest, however, very little is known about the atmosphere of this planet, especially when compared with the information we have about Mars. The main reason for this deficiency is that Venus is covered with a layer of white clouds, and the surface remains permanently invisible. Observations have, however, been made in the infrared and radiofrequency regions, and new information regarding the composition and temperature distribution in the Venus atmosphere has been obtained in the last few years. These new data on the temperature and pressure at the various levels in the Venus atmosphere have forced a complete revision of ideas regarding the atmospheric structure of this planet. We shall try to summarize our present-day knowledge regarding the Venus atmosphere by first giving the physical constants of the planet (Table 4) and then reviewing the current hypotheses regarding its structure.

Composition

From the analysis of the reflected solar spectrum, the only constituent of Venus atmosphere established beyond question is CO_2 . Its abundance above the effective "reflecting level" of the sunlight has been estimated by several workers. Recent reinterpretations of the old spectra of Venus by Spinrad (Reference 16) give a CO_2 /atmosphere ratio of only 5% by mass.

The scattering and polarizing properties of the clouds correspond to fine droplets of about 2μ in diameter with the refractive index of water. However, Spinrad has carefully examined a high dispersion spectrogram of Venus taken by Adams and Dunham (Reference 17) at a time when there were apparently "breaks" in the clouds, and he has concluded that the mixing ratio of water vapor down to a pressure of 8 atmospheres was less than one part in 10^5 .

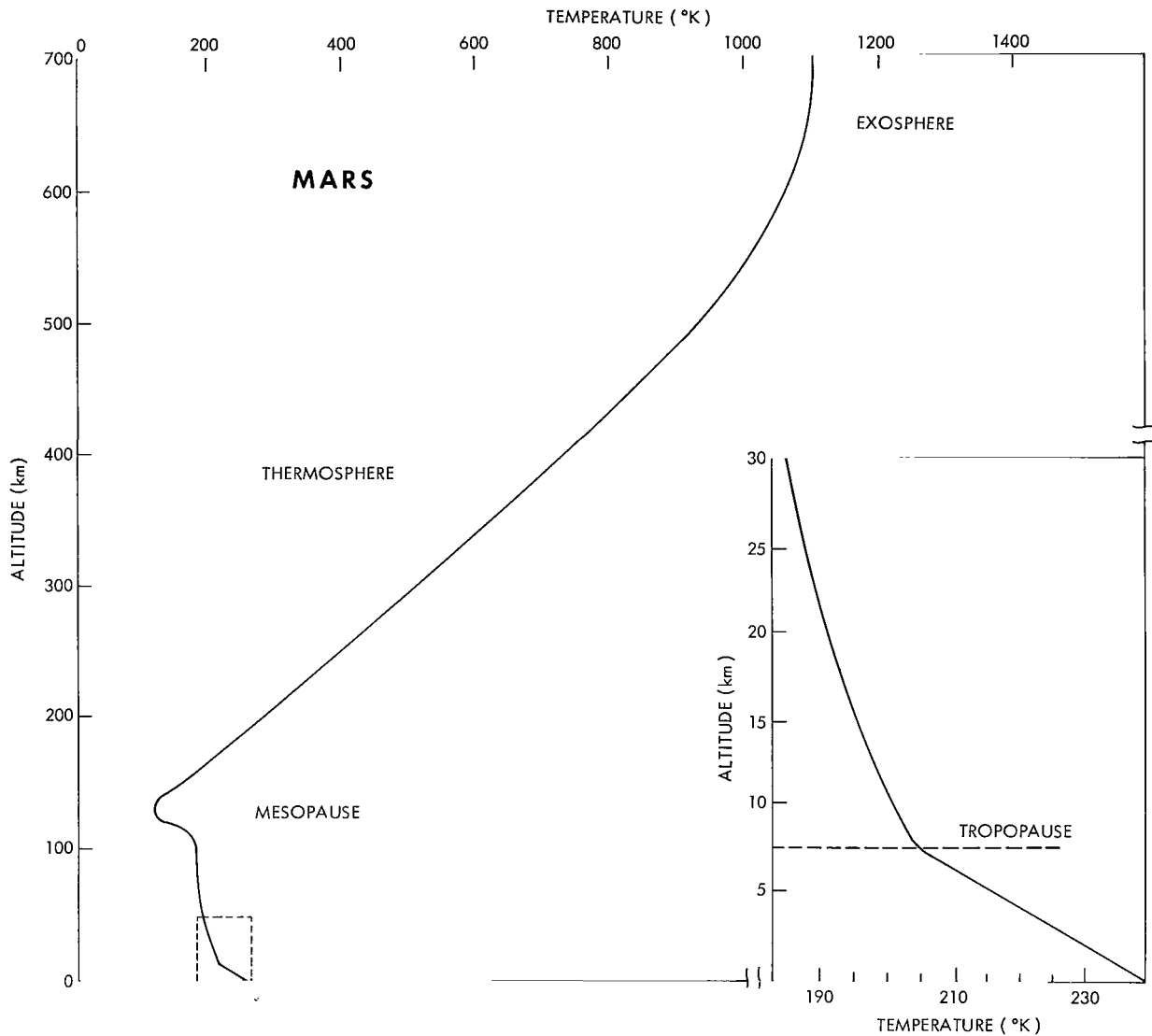


Figure 5—Vertical temperature structure of the Martian atmosphere (from References 4 and 14).

Table 4
Physical Constants of Venus and Earth.

Planet	Mass	Radius	Distance (AU)	Density (gm/cm ²)	Albedo	T _e (°K)	g (cm/sec ²)
Earth	1	1	1	5.5	0.39	245	980
Venus	0.81	0.97	0.72	5.0	0.73	235	842

At the same time, Dollfus (Reference 18) has identified water vapor absorption in the upper atmosphere of Venus, and obtains a mixing ratio of 10^{-4} or 10^{-5} by mass, depending upon the cloud top pressure.

From the observed equality in the radar reflectivity of Venus at 68 and 12.5 cm (Reference 19), Thaddeus* has recently calculated an upper limit of 3 gm/cm^2 to the total amount of water vapor which could be present in the atmosphere of Venus. From these results the atmosphere of Venus seems to be extremely dry, but a generally accepted value for the amount of water vapor present is not yet available.

Sinton (Reference 20) has presented evidence for the existence of CO above the reflecting level of two micron photons. However, Kuiper (Reference 21) has not detected this gas in his recent analysis of high resolution spectra of Venus.

Urey (Reference 22) has noted that as much as 80 m-atm of oxygen could exist above the clouds without having been detected. Also according to Urey, CH_4 and NH_3 cannot be important constituents of the atmosphere in the presence of CO_2 , and the oxides of nitrogen cannot be expected in any planetary atmosphere because they are unstable against decomposition into N_2 and O_2 . It seems likely that the bulk of the atmosphere is composed of N_2 . Rare gases may also be present as minor constituents.

The likely composition of the atmosphere of Venus is therefore as follows: N_2 , 95%; CO_2 , 5%; and H_2O less than $10^{-3}\%$ by mass.

Pressure

There is conflicting evidence concerning the pressure at the cloud top level. A difference in the polarization of red and green light reflected from the cloud top has been interpreted by Dollfus (Reference 23) as the result of molecular scattering in an atmosphere 800 m. thick at STP, which corresponds to a cloud top pressure of 90 mb. Sagan (Reference 24) has analyzed Spinrad's results on the temperature-pressure combinations indicated by CO_2 lines on different plates, and he concludes that the cloud top pressure on the illuminated side lies between 0.53 and 0.83 atm. This is consistent with Kaplan's (Reference 25) discussion of the pressure broadening of the $1.6\mu \text{ CO}_2$ bands.

From other considerations Sagan also derives a cloud top pressure of 90 mb for the night side of Venus with an uncertainty of a factor of 3.

Estimates for the pressure at the surface of Venus range from 7 to 200 atm. These will be discussed in more detail in a later section.

*P. Thaddeus, Private communication, 1963.

Temperature

Cloud top

Sinton and Strong (Reference 26) have repeatedly measured the planetary emission from the cloud top in the $8\text{--}12\mu$ region and find a temperature value of $235 \pm 10^\circ\text{K}$. This temperature probably refers to the cloud top level of the Venus atmosphere. Recent results from Mariner II seem to confirm this conclusion (Reference 27).

From this value of temperature it is possible to construct a model for the atmosphere of Venus above the clouds. Figure 6 shows a temperature profile computed by Rasool (Reference 28) on the assumption that the atmosphere is in radiative equilibrium above the clouds.

The temperature should reach an asymptotic value of 197°K above an altitude of about 20 km. The mesopause will probably occur above 60 km, and then the temperature will rise in the thermosphere because of heating by photodissociation and photoionization reactions. Lack of knowledge of the composition prevents predicting whether heating should occur below the mesopause by such mechanisms as ultraviolet absorption by ozone.

Surface

Determinations of the surface temperature of Venus by optical astronomy have been prevented by the cloud cover. However, the small amount of thermal radiation emitted by the planet in the centimeter wavelength region should penetrate through the clouds without significant attenuation, and therefore it can be used to determine the temperature of the surface of the planet.

First attempts to measure radiation from Venus in the microwave region were made in 1956 by the radiotelescope of the Naval Research Laboratory. The temperature inferred from the measured radiation intensity, was, however, unexpectedly high—of the order of 600°K , which is certainly too hot to support any imaginable form of life. Repeated measurements in following years have confirmed this result (Reference 29).

The observed temperatures are plotted as a function of wavelength in Figure 7. At longer wavelengths the brightness temperature is observed to increase when the Venus-sun-earth angle

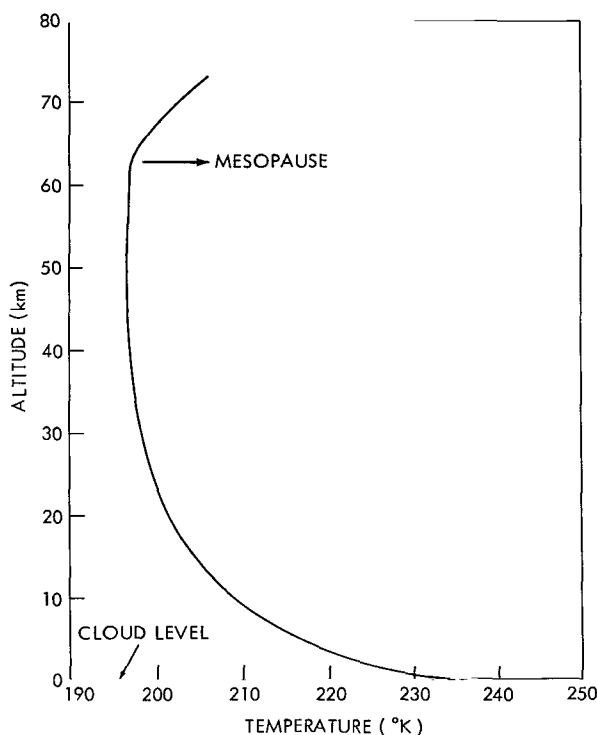


Figure 6—Temperature profile in the Venus atmosphere above the clouds (from Reference 28).

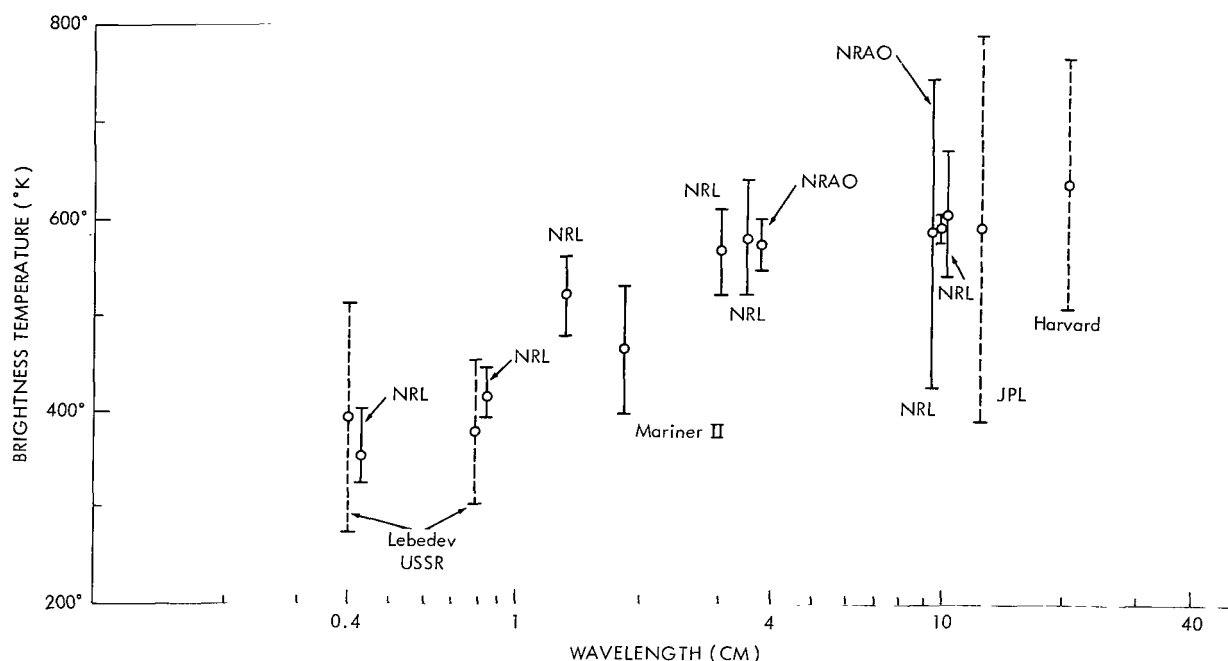


Figure 7—Observed microwave brightness temperatures of Venus at different wavelengths.

becomes appreciable, indicating that the illuminated hemisphere is significantly hotter than the dark side. (The 10 cm. brightness temperature may exceed 700°K on the bright side.) Three models of Venus have been considerably discussed in connection with these measurements.

Greenhouse Model

First is the greenhouse model originally discussed by Sagan (Reference 30) in which it is assumed that the 600°K radio-brightness temperature actually exists at the surface of the planet and is maintained by a very effective greenhouse effect. The solar radiation in the visible penetrates up to the surface; the planet, thereby being heated up to a temperature T_e , emits in the infrared; but due to the presence of triatomic molecules like CO_2 and H_2O , which have strong absorption bands in the infrared region, most of the radiation remains trapped in the atmosphere and heats up the surface.

Jastrow and Rasool (Reference 31) have recently pointed out that in such a model an extremely high infrared opacity of the atmosphere (optical thickness of 42, meaning a transmission of only 10^{-18}) will be required in order to obtain a Venus ground temperature of 600°K.

It is very difficult to understand how the lower Venus atmosphere can be so opaque in the infrared and still be transparent in the visible. Tri-atomic molecules are good infrared absorbers, but they have "windows" at certain wavelengths which must be blocked by other molecules if the opacity is to be significant. Jastrow and Rasool have also shown that the combination of CO_2 and small amounts of H_2O at pressure of the order of 3 atm. still contains significant windows.

However, the situation alters if the atmospheric pressure at ground level is many tens or hundreds of atmospheres. Then pressure broadening may close all the windows. Plass and Stull (Reference 32) have shown that the optical thickness approaches 5 if the ground pressure is about 30 atms. and the pressure broadening of CO_2 alone is considered. At the high temperatures on Venus there may be many trace constituents in the atmosphere that significantly increase the opacity.

Aeolosphere

The second model, called the aeolosphere model, is due to Öpik (Reference 33) who suggests that the blanketing must be due to dust, wind friction of the surface being the main source of energy for the high temperature. The dust is probably made of calcium and magnesium carbonates and the atmosphere is mainly composed of CO_2 and N_2 . No water vapor is necessarily present in the atmosphere. Due to the blanket of dust there is no sunlight penetrating to the surface. This model predicts that the microwave brightness temperatures of Venus should not change with the phase of Venus, which is apparently contradicted by the observations.

Ionospheric Emission

A third model invokes a dense ionosphere of Venus which is assumed to emit the observed microwave radiation. This model predicts that the radio observations should show a "brightening" at the limb of Venus, whereas the observations made by Mariner II have recently indicated "limb darkening" (Reference 34).

JUPITER

Relatively little is known about the structure of the atmosphere of Jupiter.

Being five times farther removed from the sun than the earth, but having a comparable albedo of 0.47, the effective temperature of the planet is only 105°K . The high surface gravity and low temperature together suggest that the gravitational escape of gases from the planet should be extremely inefficient and the chemical composition of the atmosphere should still be primitive, containing large quantities of hydrogen and helium.

Composition

The only gases detected spectroscopically in the atmosphere of Jupiter are NH_3 , CH_4 and hydrogen. The abundances of these gases have been estimated by various authors, and Table 5 gives the approximate composition of the atmosphere of Jupiter (Reference 35).

Helium is spectroscopically not observable from the earth and has been added due to its cosmic abundance and to account for the estimates of the cloud top pressure of 3 atms.

Table 5
The Approximate Composition of the Jovian Atmosphere.

Gas	Volume (Percent)
H ₂	60
He	36
Ne	3
CH ₄ and NH ₃	< 1

Table 5 indicates that the Jovian atmosphere may not be as rich in hydrogen as expected from the discussion of gravitational escape.

Measurements of the scale height of the atmosphere of Jupiter have been made by observing the occultation of σ -Arietis by Jupiter. These observations yield a scale height of about 8 km. For a mean atmospheric temperature of 120°K, the corresponding molecular weight would be approximately 4. This requires more helium than Table 5

indicates. However, according to Gallet (Reference 36) the relative abundance of H and He given in Table 5 could also account for a mean molecular weight of 4 if the Jovian atmosphere had a substantial amount of neon.

Temperature

The calculated black body temperature of Jupiter for a visual albedo of 0.47 is 105°K. Spectroscopic measurements in the infrared indicate a temperature of 130°K (Reference 37) which probably refers to the cloud top level.

Gallet (Reference 36) has made extensive theoretical analyses of the atmospheric structure of Jupiter below the clouds. The visible clouds have been assumed to be made of NH₃ crystals, which condense at the temperature and density of the cloud top. With allowance for the heat released in this condensation, Gallet calculates a relatively slow increase of temperature going down from the clouds to the surface and thus arrives at high densities and pressures at low temperatures. Gallet has also suggested that the observed cloud layer may be NH₃ of thickness 50 km, below which there is another deck of clouds composed of H₂O. Between these two clouds is a region where NH₃ rain storms can occur. In such a model the surface of Jupiter would be a few hundred km below the clouds, at a temperature of about 1000°K and a pressure of several thousand atmospheres.

REFERENCES

1. Aller, L. H., "The Abundance of the Elements," New York: Interscience Publishers, 1961.
2. Spitzer, L., Jr., "The Terrestrial Atmosphere above 300 Km," in "The Atmospheres of the Earth and Planets," (G. P. Kuiper, ed.): 211-247, Chicago: University of Chicago Press, 1952.
3. MacDonald, G. J. F., "The Escape of Helium from the Earth's Atmosphere," *Revs. Geophys.* (In press, 1963).
4. Chamberlain, J. W., "Upper Atmospheres of the Planets," *Astrophys. J.* 136(2):582-593, September 1962.

5. Walker, J. C. G., and Jastrow, R., "The Thermospheres of the Planets," *Amer. Geophys. Union Trans.* 44(1):85, March 1963.
6. Spinrad, H., Münch, G., and Kaplan, L. D., "The Detection of Water Vapor on Mars," *Astrophys. J.* 137(4):1319-1325, May 1963.
7. Dollfus, A., "A Measurement of the Quantity of Water Vapour Contained in the Atmosphere of the Planet Mars," (In French), *C. R. Acad. Sci.* 256(14):3009-3011, April 1963.
8. Vaucouleurs, G. H. de, "Physics of the Planet Mars," London: Faber and Faber, 1954.
9. Dollfus, A., "Études des planètes par la polarisation de leur lumière," *Ann. de Astrophysique* Supp. no. 4, 1957.
10. Sinton, W. M., "Further Evidence of Vegetation on Mars," *Science* 130(3384):1234-1237, November 6, 1959.
11. Kuiper, G. P., "Planetary Atmospheres and Their Origins," in "The Atmospheres of the Earth and Planets," (G. P. Kuiper, ed.): 306-405, Chicago: University of Chicago Press, 1952.
12. Goody, R. M., "The Atmosphere of Mars," *Weather*, 12(1):3-15, January 1957.
13. Hess, S. L., "Mars as an Astronautical Objective" in *Advance in Space Science and Technology*, v. 3 New York: Academic Press, 1961, pp 151-193.
14. Arking, A., "Non-Grey Convective Planetary Atmospheres," *Soc. Roy. Sci. Liège Mem.* 7 (spec. no.): 180-189, 1963.
15. Ohring, G., "A Theoretical Estimate of the Average Vertical Distribution of Temperature in the Martian Atmosphere," *Icarus* 1(4):328-333, January 1963.
16. Spinrad, H., "Spectroscopic Temperature and Pressure Measurements in the Venus Atmosphere," *Astron. Soc. Pacific Publ.* 74: 187-201, June 1962.
17. Adams, W. S., and Dunham, T., Jr., "Absorption Bands in the Infra-Red Spectrum of Venus," *Astron. Soc. Pacific Pub.* 44(260):243-245, August 1932.
18. Dollfus, A., "Observations of Water Vapour on the Planet Venus," (In French), *C. R. Acad. Sci.* 256(15):3250-3253, April 8, 1963.
19. Muhleman, D. O., "The Electrical Characteristics of the Atmosphere and Surface of Venus from Radar Observations," *Icarus* 1(5/6):401-411, April 1963.
20. Sinton, W. M., "Infrared Observations of Venus," *Soc. Roy. Sci. Liège Mem.* 7(spec. no.):300-310, 1963.
21. Kuiper, G. P., "Infrared Spectra of Planets and Cool Stars," *Onzieme Colloque International d'Astrophysique, La Physique des Planètes*, Université de Liège, 1963.
22. Urey, H. C., "The Atmospheres of the Planets," in "Handbuch der Physik," (S. Flügge, ed.), 52: 363-418, Berlin: Springer Verlag, 1959.
23. Dollfus, A., "Polarization Studies of Planets," in "The Solar System III, Planets and Satellites," (G. P. Kuiper and B. M. Middlehurst, eds.): 343-399, Chicago: The University of Chicago Press, 1961.

24. Sagan, C., "Structure of the Lower Atmosphere of Venus," *Icarus* 1(2):151-169, September 1962.
25. Kaplan, L. D., "A New Interpretation of the Structure and CO₂ Content of the Venus Atmosphere," *Planet. Space Sci.* 8(1):23-29, October 1961.
26. Sinton, W. M., and Strong, J., "Radiometric Observations of Venus," *Astrophys. J.* 131(2):470-490, March 1960.
27. Chase, S. C., Kaplan, L. D., and Neugebauer, G., "Mariner II: Preliminary Reports on Measurements of Venus: Infrared Radiometer," *Science* 139: 907-908, March 8, 1963.
28. Rasool, S. I., "Structure of Planetary Atmospheres," *Amer. Inst. Aeronaut. Astronaut. J.* 1(1):6-19, January 1963.
29. Mayer, C. H., "Radio Emission of the Moon and Planets," in "The Solar System, Vol. III, Planets and Satellites," (G. P. Kuiper, and B. M. Middlehurst, eds.): 442-472, Chicago: University of Chicago Press, 1962.
30. Sagan, C., "The Radiation Balance of Venus," JPL Tech. Rep. No. 32-34 (NASA Contract No. NASw-6), Pasadena: California Institute of Technology, September 15, 1960.
31. Jastrow, R., and Rasool, S. I., "Radiative Transfer in the Atmospheres of Venus and Mars," in *Space Research III*, ed. by W. Priester, Amsterdam: North Holland Publishing Co., 1963.
32. Plass, G. N., and Stull, V. R., "Carbon Dioxide Absorption for Path Lengths Applicable to the Atmosphere of Venus," *J. Geophys. Res.* 68(5):1355-1363, March 1, 1963.
33. Öpik, E. J., "The Aeolosphere and Atmosphere of Venus," *J. Geophys. Res.* 66(9):2807-2819, September 1961.
34. Barath, F. T., Barrett, A. H., Copeland, J., Jones, D. E., and Lilley, A. E., "Mariner II: Preliminary Reports on Measurements of Venus: Microwave Radiometers," *Science*, 139: 908-909, March 8, 1963.
35. Spinrad, H., and Trafton, L. M., "High Dispersion Spectra of the Outer Planets. I. Jupiter in the Visual and Red," *Icarus* 2(1):19-28, June 1963.
36. Gallet, R., "The Structure of the Cloud Layers and the Deep Atmosphere of Jupiter," in "Proc. Conf. on the Planet Jupiter," (H. J. Smith, ed.), (In press).
37. Murray, B. C., and Wildey, R. L., "Stellar and Planetary Observations at 10 μ ," *Astrophys. J.* 137(2):692-693, February 15, 1963.

BIBLIOGRAPHY

- Cameron, A. G. W., "Physics of the Planets," in *Space Physics* (In press, 1963).
- Hess, S. L., "Mars as an Astronautical Objective," in "Advances in Space Science and Technology," v. 3 (F. I. Ordway, ed.): 151-193, New York: Academic Press, 1961.

- Jastrow, R., "Results of Experiments in Space," *J. Aerospace Sci.* 29, 377 (1962).
- Kellogg, W. W., and Sagan, C., "The Atmospheres of Mars and Venus," Washington, D. C.: Nat. Acad. Sci.-Nat. Res. Coun. Publ. 944, 1962.
- Newburn, R. L., Jr., "The Exploration of Mercury, the Asteroids, the Major Planets and Their Satellite Systems, and Pluto," in "Advances in Space Science and Technology," v. 3 (F. I. Ordway, ed.): 195-272, New York: Academic Press, 1961.
- Sagan, C., and Kellogg, W. W., "The Terrestrial Planets," *Ann. Rev. Astron. Astrophys.* 1: 235-266, 1963.
- Wildt, R., Smith, H. J., Salpeter, E. E., and Cameron, A. G. W., "The Planet Jupiter," *Phys. Today*, 16(5):19-23, May 1963.

PERCENTAGE CLOUD COVER FROM TIROS PHOTOGRAPHS

by

Albert Arking

Goddard Institute for Space Studies

SUMMARY

The analysis of approximately 1500 Tiros pictures, on a digital computer, has yielded statistical data on the global distribution of cloud cover from 12 July to 30 September 1961, between 60°S and 60°N. The latitudinal distribution of percentage cloud cover for that period is compared with a fifty-year mean based upon ground observations; the broad features of the two distributions are in agreement.

INTRODUCTION

There is presently a program to study the heat balance of the earth's atmosphere, using the observational data now available on a global scale from the Tiros meteorological satellites.

To understand the dynamical processes in the atmosphere, it is now clear that we must first understand the large scale, global patterns of motion, which serve as the underlying base upon which weather phenomena are superimposed. The large scale patterns are determined by the energy balance—an important aspect being the variations in incoming and outgoing radiation around the globe. The uneven heating of the earth and atmosphere by solar radiation, supplies the primary driving force behind the general circulation.

The net input of radiant energy at any point on the globe is determined by:

1. *The solar flux incident at the top of the atmosphere.* This is determined purely by geometrical considerations, viz., the angle of the sun with respect to the zenith. Aside from seasonal variations, this leads to a cosine law in the latitudinal distribution of solar flux.
2. *The fraction of the solar flux reflected back into space, i. e., the reflective albedo.* This is determined to a very large extent by the cloud cover. The reflectivity of a cloud-covered region can range up to 80%, depending upon the thickness of the cloud. On the other hand, the reflectivity of water and most land terrain varies from about 3 to 15%, the exceptions being desert areas, which may have reflectivities as high as 25%, and snow, which has reflectivities comparable to thick clouds. The average albedo of the earth is 35%, the main contribution coming from the approximately 50% cloud cover which prevails over the earth. The global cloud cover, therefore, causes a significant

departure from the simple cosine law in the latitudinal distribution of solar heating and has an important effect on the general atmospheric circulation.

3. *Emission of infrared radiation from the earth and atmosphere.* The infrared emission is determined by the amount and distribution of the infrared absorbing constituents of the atmosphere. In the so-called "window region," 8 to 12μ , a cloudless atmosphere is essentially transparent, but even a relatively thin layer of clouds is opaque. Hence, the radiation that emanates from the earth in the 8 to 12μ region is characteristic of the temperature of the cloud top, or the ground, if there are no clouds. Since the temperature of the cloud top depends upon its height, there is a strong relationship between the energy radiated in the 8 to 12μ region and the extent and height of the cloud cover.

Although the window contains only a fraction of the total infrared energy, nevertheless, the *variations* of the total infrared energy from time to time and point to point on the globe, are due almost entirely to variations in the 8 to 12μ region. Therefore, the cloud cover is an extremely important factor in the loss of energy through infrared radiation, in addition to its direct control over the solar energy admitted into the lower atmosphere.

The Tiros meteorological satellites contain equipment for monitoring both the radiation and the cloud cover. Radiometers measure the outgoing radiation from the earth in the infrared and visible regions of the spectrum, while two television cameras photograph the cloud cover.

The analysis and interpretation of the radiation data is presently being pursued at Goddard Space Flight Center, the U. S. Weather Bureau, and at the University of Chicago. A preliminary report of the work at the Goddard Institute for Space Studies was presented last year by Prabhakara and Rasool (Reference 1).

Until now, the cloud cover photographs have been used primarily for the purposes of day-to-day forecasting and for tracking storms and hurricanes. These were the purposes in mind when the camera and television systems were designed.

However, we have been primarily interested in the large scale energy balance of the atmosphere. In view of the important role that cloud cover plays in this problem, we have set out to process the Tiros photographs to obtain statistical data on the global cloud cover distribution. We have analyzed 1447 Tiros III photographs for this purpose, using an IBM 7090 computer. The end product of the analysis is a magnetic tape containing a synopsis of each of the 1447 pictures. By means of a computer program, the tape can be interrogated to give the mean cloud cover over any geographical region during any interval of time.

The Tiros III photographs were taken during daytime from 12 July to 30 September 1961. The inclination of the satellite orbit restricted the photography to the region between latitudes 60°S and 60°N .

The use of satellite photographs to determine mean cloud cover percentage is based upon the assumption that each picture is an independent random sample of the cloud cover situation. It is

therefore necessary to take cognizance of the distribution of photographs with respect to geographic location and time, when interpreting the results. The fact that pictures within a sequence overlap and are therefore correlated should not invalidate the results, which are based upon treating each picture as an independent sample. The overlapping simply means that regions photographed twice are given twice as much weight in computing averages; this procedure is reasonable because the uncertainty in determining the extent of cloud cover in any region decreases with the number of available photographs of that region.

PROCESSING THE PICTURES

The cloud cover pictures are transmitted from the satellite to the ground station by means of a video system. The image consists of 500 scan lines forming a square pattern on a cathode ray television screen. Photographs of the television image are recorded on film. In addition to the film record, the video signal is recorded on magnetic tape.

To convert the pictures into digital form for insertion into the computer, the taped video signal is sampled at 500 points along each scan line. The result is a 500×500 array of numbers representing the brightness levels in the picture. Brightness is represented by a six-bit code, allowing 64 different brightness levels.

That the quality of the picture is retained after the digitization process, can be seen in Figure 1, which compares the original TV image (Figure 1a) with the digitized image which is displayed on the SC-4020 digital cathode ray plotter, (Figure 1b). Only ten different grey levels were available on the 4020 plotter.



(a) A Tiros III photograph taken over the Pacific Ocean southwest of Japan 21 August 1961, is shown as it appears on a video screen.



(b) The same picture is displayed using ten grey levels on an SC-4020 digital cathode ray plotter after digitization into a nominally 500×500 matrix.

Figure 1—Effect of digitization on the quality of a Tiros TV image.

The cameras are oriented with the optical axes parallel to the spin axis of the satellite. Since the satellite is spin-oriented, the direction of the cameras is fixed with respect to space. When the camera is pointed along the normal to the earth, the area viewed is approximately 1000 km square. In general, the camera axis forms an angle with respect to the normal to the earth, called the *nadir angle* (Figure 2). Distortions due to the perspective view of the camera and the earth's curvature are properly corrected, taking into account the satellite's position, the spin axis orientation, and the roll angle.

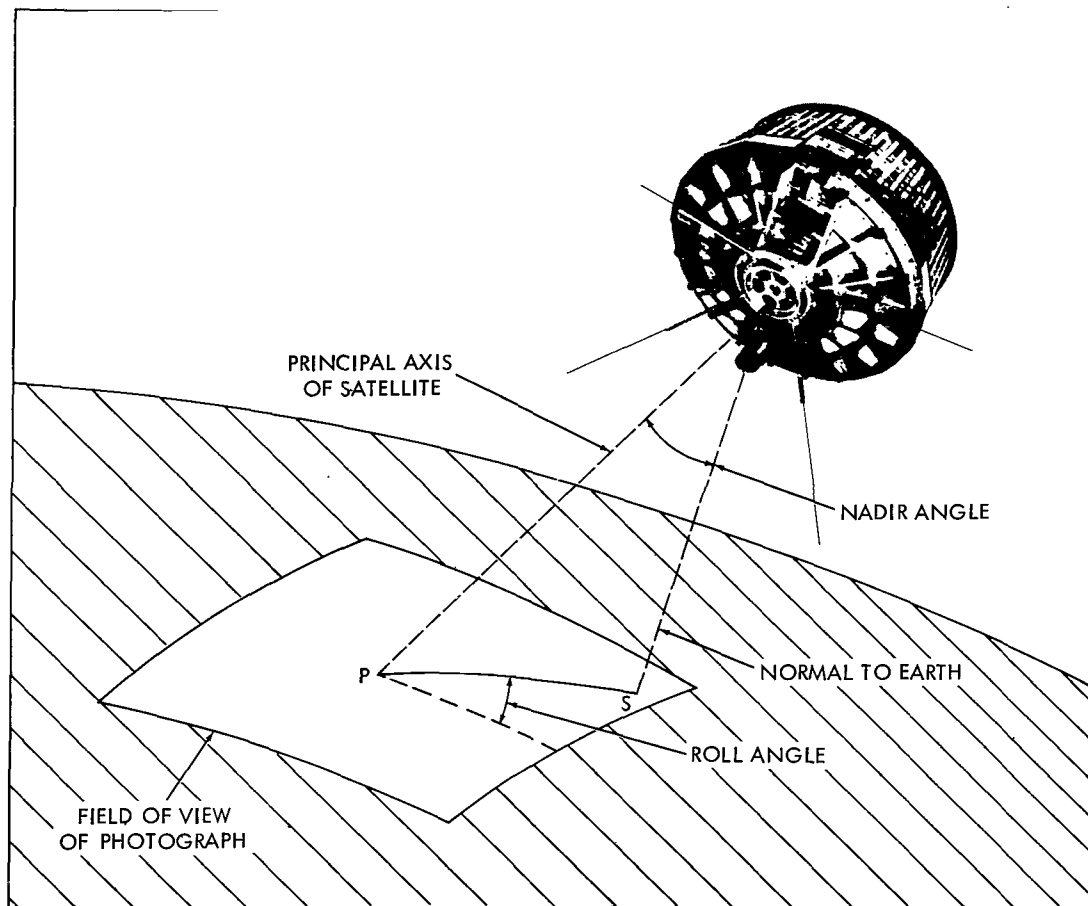


Figure 2—Geometry of Tiros photography. The two television cameras point along the principal or spin axis of the satellite, which is fixed in space. The angle between the principal axis and the normal to the earth, the nadir angle, changes as the satellite orbits the earth. The intersection of the principal axis with the earth is called the principal point, denoted by P, and the point immediately below the satellite, called the sub-satellite point, is denoted by S. As the satellite rotates, the image on the vidicon tube appears to rotate about the point P. The angle between PS and a fixed reference line on the vidicon tube defines the roll angle γ , the value of which is required, in addition to the geographic positions of P and S, to transform from picture coordinates to geographic coordinates.

DETERMINATION OF CLOUD BOUNDARIES

The main problem in the analysis of cloud pictures on a computer is the choice of a criterion for distinguishing clouds from clear areas. Reflectivity would be a suitable criterion, for clear areas

will have lower reflectivities than clouds except in snow covered regions. The relation between reflectivity and brightness, however, depends upon several factors: the relative angles of the sun and camera with respect to the surface appearing in the photograph, the structure and thickness of clouds, and the nature of the underlying terrain. In addition, there may be variations in the characteristics of the television system during the lifetime of the satellite. The reflectivities of clouds, however, are so much higher than those of the underlying terrain, that the brightness of regions as they appear in a photograph is found to be a reliable criterion. For any one picture it is possible to choose a brightness threshold which distinguishes clouds from other features; furthermore, the threshold is found to vary only slightly from picture to picture within the set of pictures transmitted during any one pass of the satellite over the read-out station. It is therefore necessary to determine a threshold for each read-out orbit. The intent is to choose a threshold which will reproduce the same cloud boundaries that would appear to a human observer studying the picture.

The technique for finding the proper threshold involved use of the SC-4020 cathode ray digital plotter. For a given threshold, a two-level image is produced on the SC-4020, in which grey levels above the threshold are white and other levels are black. For a number of different thresholds, the SC-4020 produces a series of such two-level images—for example, the five images in the bottom row of Figure 3. The original picture (Figure 1a is reproduced in the upper portion of Figure 3) is then compared by the observer with each of the two-level images, and the observer selects the two-level image in which the boundary most closely resembles his impression of the cloud boundaries as seen in the original picture. This establishes the threshold for that picture and the same threshold is applied to all other pictures transmitted during the same orbit. The list of threshold values for the various orbits forms a threshold table which is used in estimating the cloud cover.

CLOUD COVER PERCENTAGE

Each picture is divided into 121 equal square blocks after eliminating portions of the picture along each border where distortion and noise tend to be excessive. The geographical coordinates of each picture block and the total earth area covered by the block are calculated using the data on the satellite's position, attitude, and roll angle. The distribution of brightness levels—i. e., the fraction of area versus brightness—is determined for each block and entered onto a final magnetic tape along with the geographical data and the time the picture was taken. For each block of every picture that was processed, the final magnetic tape contains latitude, longitude, earth area, time and the brightness level distribution.

Given any geographical region and period of time, the mean percentage cloud cover is determined by scanning the final magnetic tape with a computer program containing the threshold table. All picture blocks that fall into the given geographical region and time interval are used in the analysis. The brightness distribution of each block is summed over all brightness levels above the threshold; the product of this sum with the total earth area gives the cloud area. The cloud area and the total area of each block are then summed to give the percentage cloud cover.

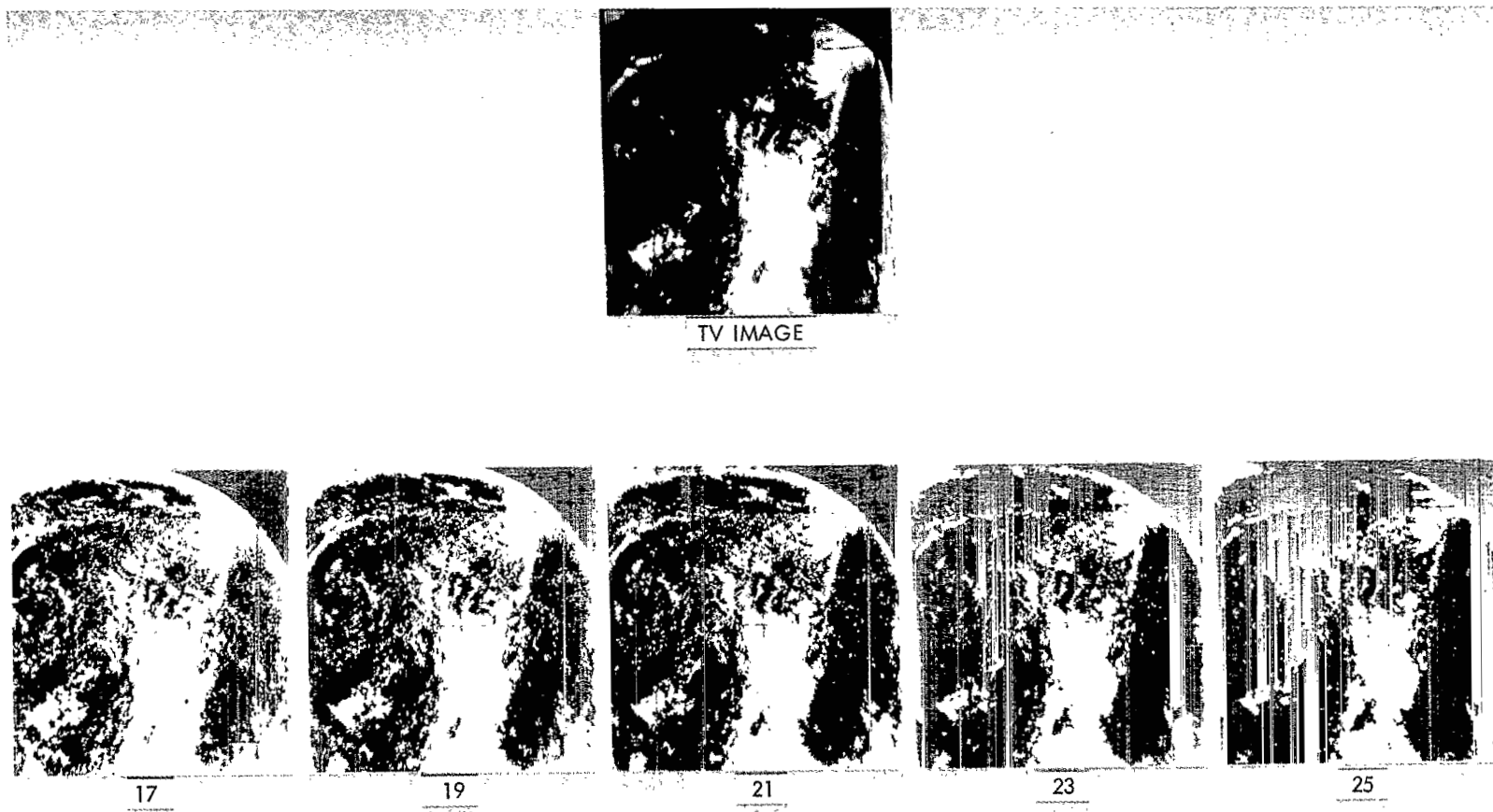


Figure 3—Brightness criteria used in discriminating clouds from clear areas. A series of two-level images, in which intensities greater than a given threshold appear white and all others black, is shown in the bottom row for five different thresholds. The number underneath each two-level image is the brightness level used as the threshold for the discrimination. The original half-tone picture, on top, is compared with each two-level image to find the threshold that most closely reproduces the cloud boundaries that the human observer finds in the half-tone image.

RESULTS

There were 1447 TIROS III photographs available on video tape which were free from excessive noise and for which we were able to obtain all the data required for the transformation to geographical coordinates. All the pictures were processed on the 7090 computer and are the basis of the results presented here.

The geographical distribution of the pictures is shown in Figure 4; each asterisk on the map represents a single photograph. All were taken in the daytime between 12 July and 30 September, 1961 between latitudes 60°S and 60°N . The number of pictures in the Southern Hemisphere is appreciably less than in the Northern Hemisphere and, consequently, errors due to statistical sampling will be greater for southern latitudes. There may also be some statistical bias in northern latitudes due to the sparseness of photographs over Asia.

The average latitudinal distribution of cloud cover is shown in Figure 5 for the period 12 July to 30 September 1961. The solid horizontal bars give the mean percentage of earth area covered by clouds in 10° latitude intervals as determined from the TIROS III photographs. The vertical

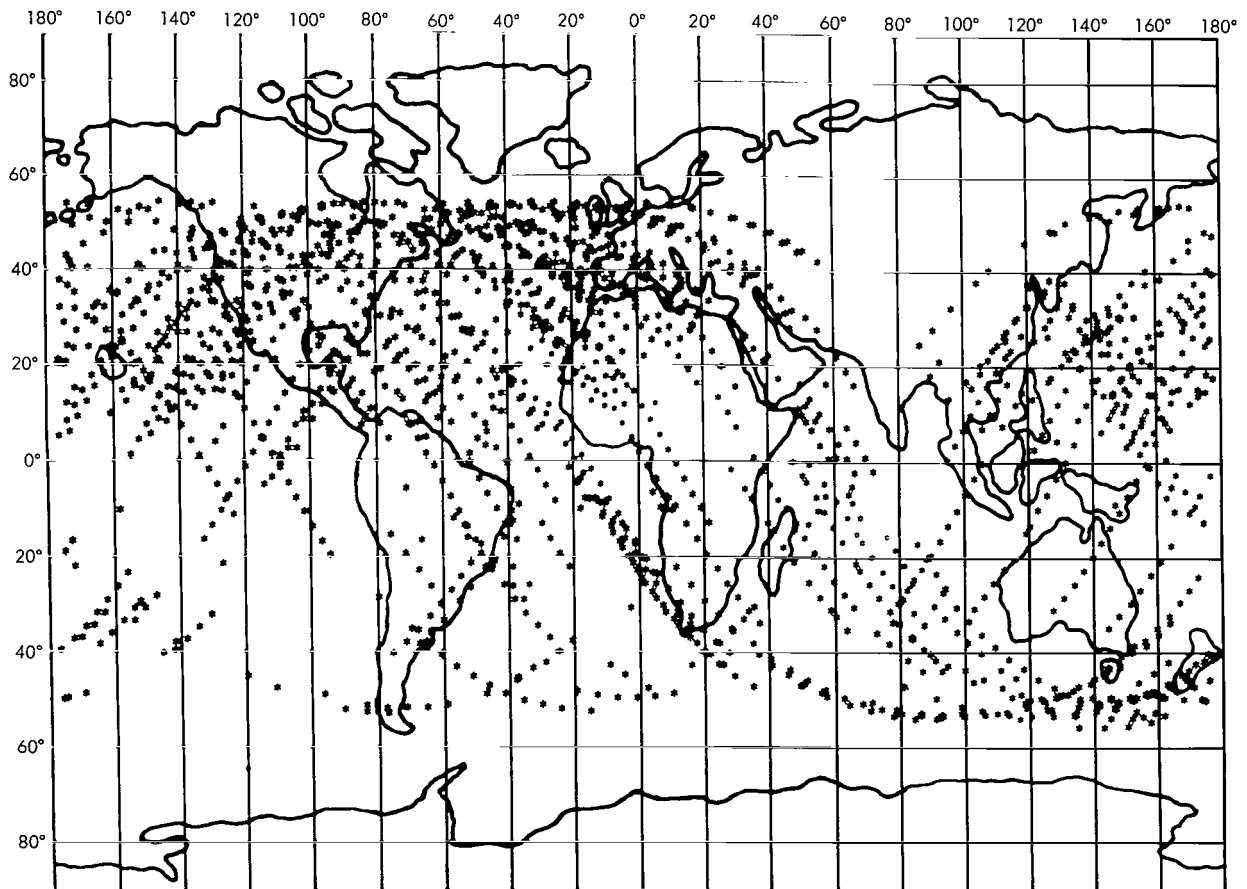


Figure 4—The geographical distribution of the 1447 Tيروس III pictures used in the analysis.

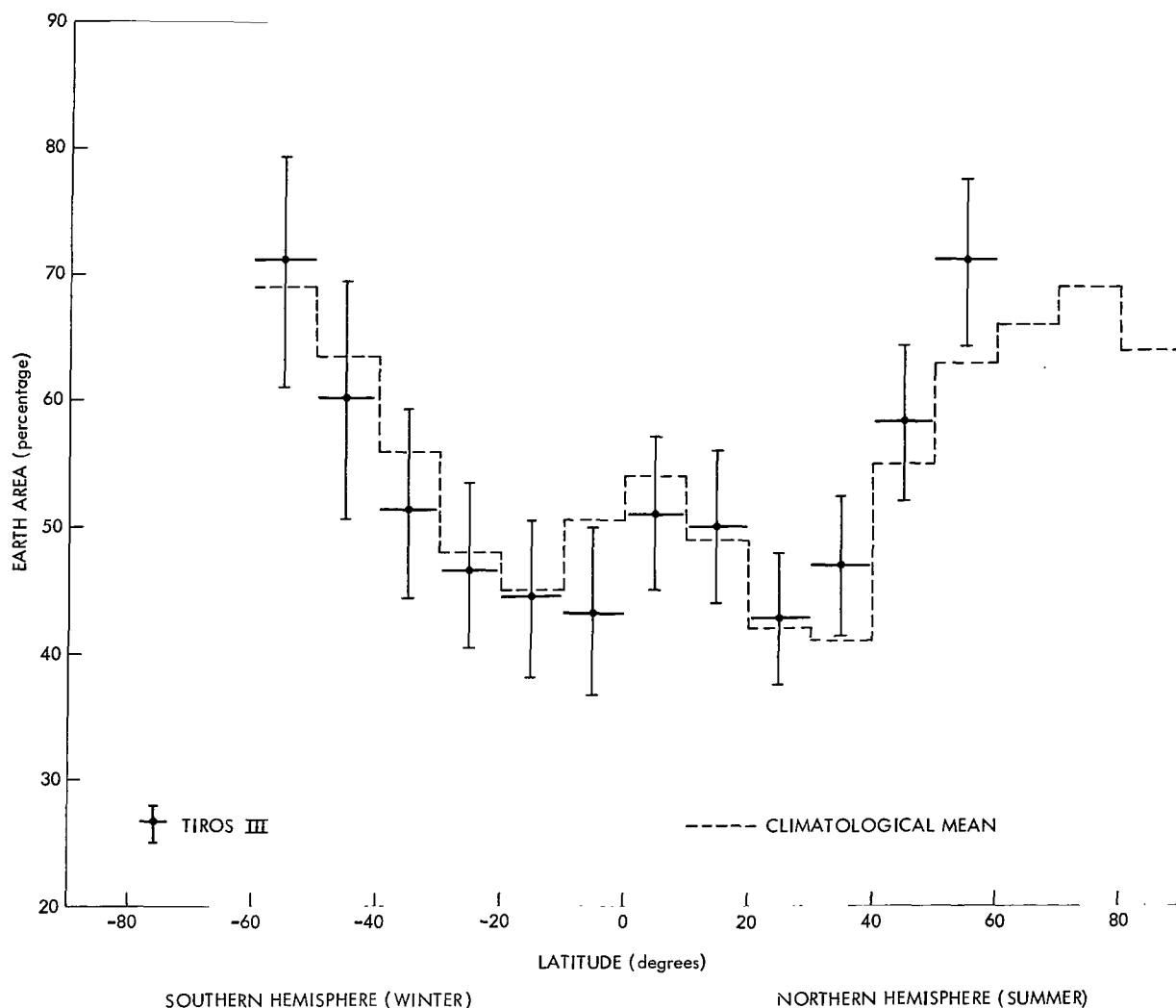


Figure 5—The latitudinal distribution of cloud cover. The solid horizontal bars are the results from Tiros III photographs from 12 July to 30 September 1961; the vertical lines show the estimated errors due to threshold determination. The dashed histogram represents the climatological mean cloud cover based upon ground observations, taken from Telegadas and London (Reference 2) for the Northern Hemisphere and from Landsberg (Reference 3) for the Southern Hemisphere.

lines passing through the bars indicate the uncertainty estimated to arise in the threshold determination. Possible errors due to statistical sampling are not shown.

The results in Figure 5 show that the cloud cover in middle latitudes is the same in the northern and southern hemispheres. However, in tropical latitudes there is an asymmetry, with a local maximum of the cloud cover in the tropics centered at 10°N latitude. This is the average position of the "thermal equator" during the period 12 July to 30 September.

The broad features of the latitudinal distribution of cloud cover obtained from the TIROS photographs are consistent with the known pattern of the general circulation (see, for example,

Reference 2). Air rising at the thermal equator produces condensation and a relative maximum in the cloud cover, while on the average there is downward motion of cool, dry air at 30° , which explains the relative minimum of cloudiness. The relationship between cloud cover distribution and vertical air currents suggests that the TIROS cloud cover statistics may have an important application in the determination of vertical motions in the atmosphere.

It is of considerable interest to compare the TIROS observations for the summer of 1961 with the climatological distributions of cloudiness found in the literature for the same season. Such distributions have been published by Haurwitz and Austin (Reference 2), Landsberg (Reference 3) and others for the globe; and, based on more extensive data, by Telegadas and London (Reference 4) for the Northern Hemisphere. The climatological results for the summer season are shown by the dashed histogram in Figure 5. The Northern Hemisphere data are taken from Telegadas and London (Reference 4); the Southern Hemisphere data are taken from Landsberg (Reference 3).

The TIROS results for 1961 are seen to be in good agreement with the long-term mean of cloud cover distribution obtained from ground observations. The degree of correspondence between our results and the ground based data gives us confidence in this method of analysis of satellite photographs. The availability of more data from subsequent satellites will permit the determination of the geographical distribution of cloud cover over short intervals of time. An increase in the density of observations, coupled with improvements in the techniques for picture analysis presently being developed, should eventually lead to the use of cloud cover pictures automatically analyzed on a computer, to provide the cloud cover distribution as a function of time for use in studies of atmospheric dynamics and long-term changes in climate.

ACKNOWLEDGMENTS

We wish to express our appreciation to Professor Julius London of the University of Colorado for suggesting the original investigation and for his detailed criticism. We are also grateful to Professors J. Charney and R. Goody for helpful suggestions and to Burton Kaufman, John Borgelt, and other members of the staff of Computer Applications, Inc., who developed the programs required for the reduction of the Tiros cloud cover tapes.

REFERENCES

1. Prabhakara, C., and Rasool, S. I., "Evaluation of TIROS Infrared Data," *Proceedings of the First International Symposium on Rocket and Satellite Meteorology*, Washington, D. C., April 23-25, 1962.
2. Haurwitz, B., and Austin, J. M., "Climatology," New York: McGraw-Hill, 1944.

3. Landsberg, H., "Climatology," in *Handbook of Meteorology*, F. A. Berry, Jr., et al. New York: McGraw-Hill, 1945, pp. 927-997.
4. Telegadas, K., and London, J., "A Physical Model for the Northern Hemisphere for Winter and Summer," College of Engineering, New York University, Research Division *Scientific Report No. 1*, 1954.

AN INTERPRETATION OF A ROCKET MEASUREMENT OF ELECTRON DENSITY IN THE LOWER IONOSPHERE

by

A. C. Aikin, Jr., J. A. Kane
Goddard Space Flight Center

and

J. Troim
Norwegian Defence Research Establishment

SUMMARY

A mid-latitude rocket measurement of electron density is presented for altitudes between 65 and 85 km. An interpretation of the profile indicates that the region between 70 and 85 km is ionized by the action of Lyman alpha radiation on nitric oxide rather than by 2-8 Å x-rays. Possible explanations are given for a minimum found in the electron density distribution in the vicinity of the mesopause.

INTRODUCTION

Current theories attribute the formation of the ionosphere below the mesopause to: (1) Ionization of the major atmospheric constituents by the highly variable 2-8 Å solar x-radiation; (2) Ionization of the minor constituent, nitric oxide, by Lyman alpha at 1215.6 Å; and (3) Cosmic rays, which extend the ionosphere below 70 km. The theoretical problem is further complicated by the possibility of a wide variety of electron loss processes including dissociative recombination of an electron-ion pair and the formation of negative ions.

A lack of quantitative data of the electron and ion density distribution and too few attempts to correlate observational results with the intensities of ionizing solar radiations, has made it difficult to check the validity of any theory. This paper will deal with the interpretation of a rocket measurement of electron density in the ionospheric D region. The profile was obtained at 1930 GMT on 8 March 1963 at Wallops Island, Virginia for a solar zenith angle of 48°.

EXPERIMENTAL RESULTS

An electron density profile (Figure 1) was obtained using a Faraday rotation technique involving transmission of a 3 Mc signal from the ground to the rocket. Each point is the average electron

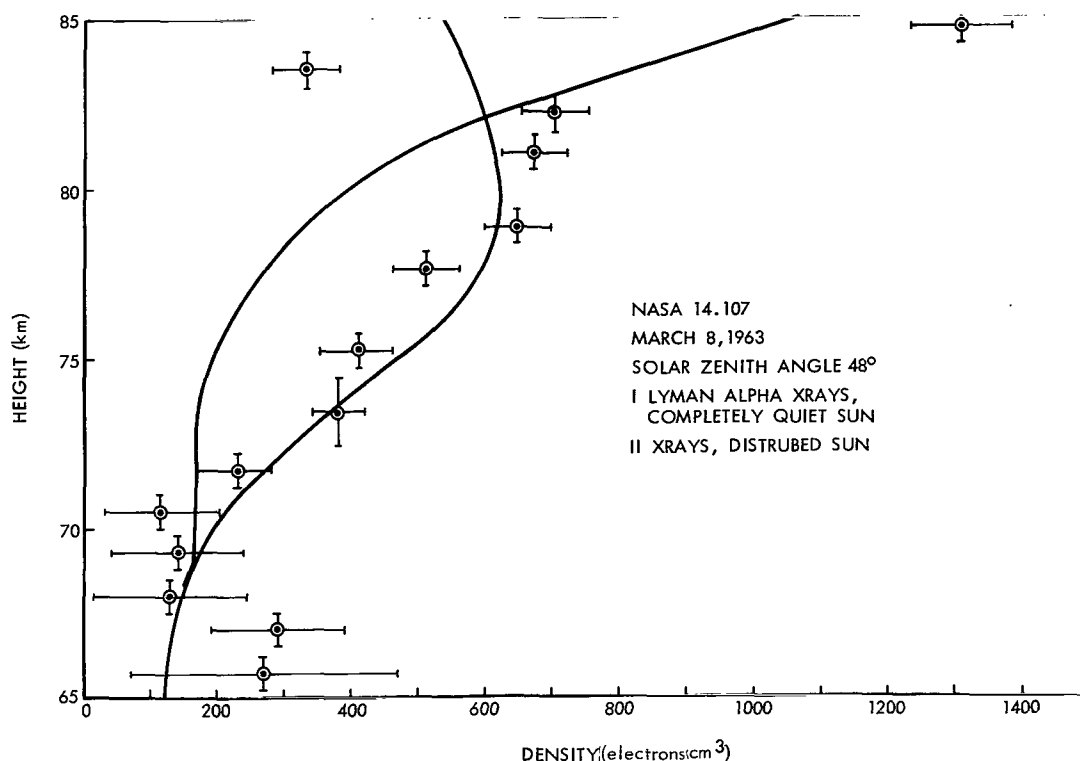


Figure 1—Observed electron concentration in the D region and two theoretical profiles (solid curves).

density in the height interval indicated by the vertical bar. The horizontal bar indicates the uncertainty in the determination of this average value. This uncertainty is due to random echoes from above the D region distorting the Faraday pattern.

Below 75 km a knowledge of electron collision frequency is necessary to deduce electron densities from a 3 Mc Faraday rotation experiment. The Faraday rotation experiment by itself allows the collision frequency to be determined at a single altitude. This follows from the fact that the sense of rotation of the plane of polarization is positive or negative for the collision frequency ν_m greater or less than the exploring frequency. By noting the altitude at which the reversal in the sense of the Faraday rotation is observed a value $\nu_m = 13.8 \times 10^6/\text{sec}$ at an altitude of 61 ± 2 km is deduced. The value is consistent with measurements made at Fort Churchill by Kane (Reference 1). Clearly discernible from the profile are: (1) The base of the E region, (2) The D region between 84 and 70 km; and (3) A region below 70 km which has been designated as the C region. The minimum in electron density at 83.5 km coincides with the mesopause. Additional evidence for the existence of the minimum has been obtained on previous rocket flights from Wallops Island.

INTERPRETATION OF THE ELECTRON DENSITY PROFILE

In order to interpret the electron density profile, it is necessary to consider the equations governing the distribution of ions and electrons as outlined by Nicolet and Aikin (Reference 2). Under conditions of equilibrium:

$$n(\text{NO}^+)n_e = \frac{n(\text{NO})K_{i\text{NO}}Q_{L\alpha}}{\alpha_{\text{DNO}} + \lambda \alpha_i}; \quad (1)$$

$$n(\text{O}_2^+)n_e = \frac{n(\text{O}_2)K_{i\text{O}_2}\epsilon Q_x + q_{\text{O}_2\text{CR}}}{\alpha_{\text{DO}_2} + \lambda \alpha_i}; \quad (2)$$

$$n(\text{N}_2^+)n_e = \frac{n(\text{N}_2)K_{i\text{N}_2}\epsilon Q_x + q_{\text{N}_2\text{CR}}}{\alpha_{\text{DN}_2} + \lambda \alpha_i}; \quad (3)$$

$$\lambda = \frac{n_-}{n_e} = \frac{1.5 \times 10^{-30} [n(\text{O}_2)]^2}{0.44}; \quad (4)$$

$$n(\text{NO}^+) + n(\text{O}_2^+) + n(\text{N}_2^+) = (1 + \lambda)n_e. \quad (5)$$

The number of Lyman alpha or x-ray photons at a given height h is represented by $Q_{L\alpha}$ and Q_x . These quantities should be measured simultaneously with the electron density. K_i is the ionization cross section and ϵ the efficiency of ionization. $q_{\text{O}_2\text{CR}}$ and $q_{\text{N}_2\text{CR}}$ represent the ionization rates due to cosmic rays and have been assigned the values of $10^{-17}n(\text{O}_2)$ and $10^{-17}n(\text{N}_2)$, respectively. The quantities $n(\text{O}_2)$, $n(\text{N}_2)$ and $n(\text{M})$ represent the number density cm^{-3} of molecular oxygen, nitrogen and the sum of all constituents. It will be assumed that the rates of dissociative recombination between positive ions and electrons of density, n_e , measured by Kasner, Rodgers and Biondi (Reference 3) are operative, namely $\alpha_{\text{DN}_2} = 6 \times 10^{-7} \text{cm}^3/\text{sec}$ and $\alpha_{\text{DO}_2} = 4 \times 10^{-7} \text{cm}^3/\text{sec}$. The effect of negative ions, n_- , is represented by λ which is the ratio between the rate of attachment of electrons to molecular oxygen and photodetachment. The coefficients involved were adopted from Chanin, Phelps and Biondi (Reference 4) and Burch, Smith and Branscomb (Reference 5). Negative and positive ions recombine at a rate α_i , which is taken to be $10^{-7} \text{cm}^3/\text{sec}$.

In order to determine the relative importance of 2-8 Å x-rays and Lyman alpha in the formation of the D region two cases are computed. One case (Curve 1) involves the ionization by solar x-rays whose intensity is representative of a completely quiet sun together with Lyman alpha acting on nitric oxide. The value of the Lyman alpha flux as measured above the D region on a subsequent flight is 2.4×10^{11} photons/ cm^2sec with a possible error of 25%. Good agreement is found with the experimental electron density data if it is assumed that $\alpha_{\text{DNO}} = 4 \times 10^{-8} \text{cm}^3/\text{sec}$ and $n(\text{NO}) = 1.5 \times 10^{-10}n(\text{M})$. However, these values are not unique, since it is only possible to determine the ratio $n(\text{NO})/\alpha_{\text{DNO}} + \lambda \alpha_i$ from the data.

Table 1 illustrates the distribution of x-ray energy assumed. Pounds* indicates that the intensity values assumed for the completely quiet sun case are in agreement with measurements made during this portion of the sunspot cycle. The second case considers ionization solely by

*K. A. Pounds, Private Communication.

x-rays which are characteristic of a disturbed sun. Since only a solar flare, which was not observed, would give sufficient intensity to fit the experimental data the observed profile is strong evidence for the Lyman alpha hypothesis.

The portion of the theoretical electron density profiles (Figure 1) below 70 km illustrates the effect of cosmic radiation. The observed electron densities between 65 and 70 km are not in accord with the theoretical prediction of a decrease in electron density below 70 km. However, in this region of the atmosphere the possible reactions between the various neutral constituents; species of ion and electrons are quite numerous and very few of the rates of these reactions are known even to within an order of magnitude.

Table 1
X-ray Intensities for Various Quiet and Disturbed Solar Conditions.

Wavelength (A)	X-ray intensity (erg/cm ² sec)	
	Quiet sun	Disturbed sun
2	10 ⁻⁸	10 ⁻⁶
4	10 ⁻⁷	10 ⁻⁵
6	10 ⁻⁶	10 ⁻⁴

Possible causes of the minimum at 83.5 km include a decrease in the concentration of nitric oxide in the region of decreasing temperature,

and the attachment of electrons to dust. The later hypothesis deserves more attention in view of the detection of dust in the vicinity of the mesopause by Soberman, Witt and Hemenway (Reference 6).

CONCLUSIONS

A measurement has been made at middle latitudes of electron density between 65 and 90 km. The D region was characterized by a layer of electron density which increases from 115 ± 35 electrons/cm³ at 70.5 km to 700 ± 50 electrons/cm³ at 82 km. These observations were in far better agreement with a theoretical model based upon the ionization of nitric oxide by Lyman alpha rather than with a model based upon ionization by 2-8 A x-rays. The nitric oxide density assumed was of the order of 10^{-10} the total particle density, and the dissociative recombination coefficient used in the calculation was 4×10^{-8} cm³/sec. A decrease in the electron density has been established in the vicinity of the mesopause.

REFERENCES

1. Kane, J. A., "Re-Evaluation of Ionospheric Electron Densities and Collision Frequencies Derived from Rocket Measurements of Refractive Index and Attenuation," *J. Atmos. Terrest. Phys.* 23:338-347, December 1961.
2. Nicolet, M., and Aikin, A. C., "The Formation of the D Region of the Ionosphere," *J. Geophys. Res.* 65(5):1469-1483, May 1960.
3. Kasner, W. H., Rogers, W. A., and Biondi, M. A., "Electron-Ion Recombination Coefficients in Nitrogen and in Oxygen," *Phys. Rev. Letters*, 7(8):321-323, October 15, 1961.

4. Chanin, L. M., Phelps, A. V., and Biondi, M. A., "Measurements of the Attachment of Low-Energy Electrons to Oxygen Molecules," *Phys. Rev.* 128(1):219-230, October 1, 1962.
5. Burch, D. S., Smith, S. J., and Branscomb, L. M., "Photodetachment of O_2 ," *Phys. Rev.* 112(1): 171-175, October 1, 1958.
6. Witt, G., Hemenway, C. L., and Soberman, R. K., "The Collection and Analysis of Particles from the Mesopause," presented at the IV International COSPAR Meeting, Warsaw, Poland, 1963.

LIFETIME AND TIME HISTORIES OF TRAPPED RADIATION BELT PARTICLES

by

Wilmot N. Hess

Goddard Space Flight Center

SUMMARY

In this paper recent advances in understanding the lifetimes of trapped radiation belt particles are surveyed. The problem of particle lifetimes has been one of the most important and perplexing in radiation belt work for several years. As a result of the past year's work, a good deal more is known about the natural Van Allen radiation belt and also the characteristics of the artificial belts produced by high altitude nuclear explosions. This increased knowledge is based on both observations and calculations of the artificial belts and Van Allen belt. This better understanding of particle lifetimes is a substantial step forward in forming an overall picture of the radiation belt in that we now have a basis for selecting source and loss processes more realistically and therefore making better models of the belt.

Electron lifetimes based on data collected from the high altitude explosions of the U.S. and U.S.S.R., and proton lifetimes in the Van Allen belt are also discussed.

INTRODUCTION

The first of the four artificial radiation belts made in 1962 resulted from the explosion of a 1.4 megaton nuclear bomb by the U.S. 400 kilometers above Johnston Island in the Pacific on July 9. This generated a new belt of trapped electrons resulting mainly from the decay of fission fragments, but possibly involving other processes as well. Measurements by Injun, 1961 02, (Reference 1) which had been in orbit about a year, showed clearly that at 1000 km a marked increase in electron flux occurred. A GM counter on Injun shielded with about 4 gm/cm² of Pb, counting electrons of several Mev via bremsstrahlung, mapped out the high energy electron distribution in space up to 1000 km. A GM counter on Traac, 1961 072, (Reference 2) shielded by 0.66 gm/cm² and counting electrons of $E > 1.6$ Mev also observed the early effects and mapped the particle distribution. A GM counter on Ariel, 1962 01, (Reference 3) showed that the explosion produced high energy electrons out to $L \sim 5$. The most complete mapping of the belt was made by Telstar, 1962 01, (Reference 4) which went considerably higher than the others to an apogee of 5630 km. Telstar unfortunately did not get launched until the day after the explosion. Telstar had a four channel solid state detector counting electrons out past $L = 2$.

Comparing the several detector count rates at about 1000 km showed that the new electrons had roughly an equilibrium fission energy spectrum identifying them as coming from β -decay of fission fragments (Reference 5).

The difference between the more extensive Telstar flux map and the Injun flux map has caused some questions in the past, but it is starting to be understood now in terms of variations of the electron energy spectrum with L . Both the Injun and Telstar contours are correct, but they must be interpreted in terms of different energy electrons.

Most of the information about the electron lifetimes obtained recently has come from watching the decay of this population of particles from Starfish.

$L < 1.7$

For $L < 1.7$ the decay of the electrons introduced by the Starfish explosion is quite slow and appears to be controlled by the atmosphere. Coulomb scattering of the electrons by the atmospheric atoms will result in changing the direction of motion of the electron and therefore changing the pitch angle, α (the angle between \mathbf{B} and \mathbf{v} , the electron velocity). This scattering will result in changing the mirror point altitude. This can be seen from inspection of the mirror equation

$$\frac{\sin^2 \alpha}{B} = \frac{1}{B_m} \quad .$$

If at some point with magnetic field B , the pitch angle α is changed, then B_m the value of the magnetic field at the mirror point is also changed. This means the mirror altitude is changed. A series of Coulomb scatters will move a particle mirror point up and down a field line, but out of this process a net loss of particles into the atmosphere will occur. This loss can be understood physically at low altitudes. If a scatter occurs very near a particle's mirror point, it can only lower the mirror point. At, and only at, the mirror point the particle's motion is perpendicular to the field line so any scattering at this point either up or down which makes the motion not perpendicular to the field line can only lower the mirror point (Figure 1).

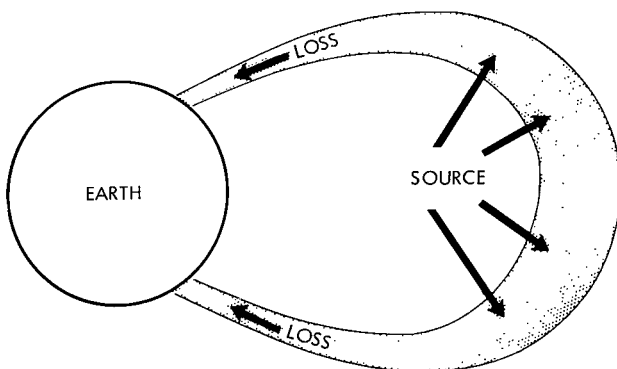


Figure 1—The Steady State Model of the Radiation Belt.

The effect of repeated Coulomb collisions can be calculated by using a Fokker-Plank equation (Reference 6) which describes how a distribution of particles $U(B, t, E)$ in a tube of force changes with time as the result of Coulomb collisions:

$$\frac{\partial U}{\partial t} = - \frac{\partial}{\partial B} \left[\langle \delta B \rangle U \right] - \frac{\partial}{\partial E} \left[\langle \delta E \rangle U \right]$$

$$+ \frac{1}{2} \frac{\partial^2}{\partial B^2} \left[\langle (\delta B)^2 \rangle U \right] \quad .$$

Where the terms in $\langle \rangle$ are the average time rates of time of the quantities. This has been integrated on a computer (Reference 7). A tube of force is divided into 100 space cells of equal ΔB and the fission energy spectrum into 9 groups and an initial mirror point distribution is selected. The $\langle \rangle$ terms are evaluated for each cell and group by averaging the scattering events over a bounce period. In doing this the atmospheric model taken to calculate the scattering was that of Harris and Priester (Reference 8) averaged in local time and in longitude. The variation of the particles' altitude with longitude is quite important in doing this average. Then the equation is integrated a time step, dt , first for scattering and then for energy loss, and the process repeated a large number of times in order to see the distribution change.

The time history of the population for $L = 1.25$ is shown in Figure 2 for $E = .75$ Mev

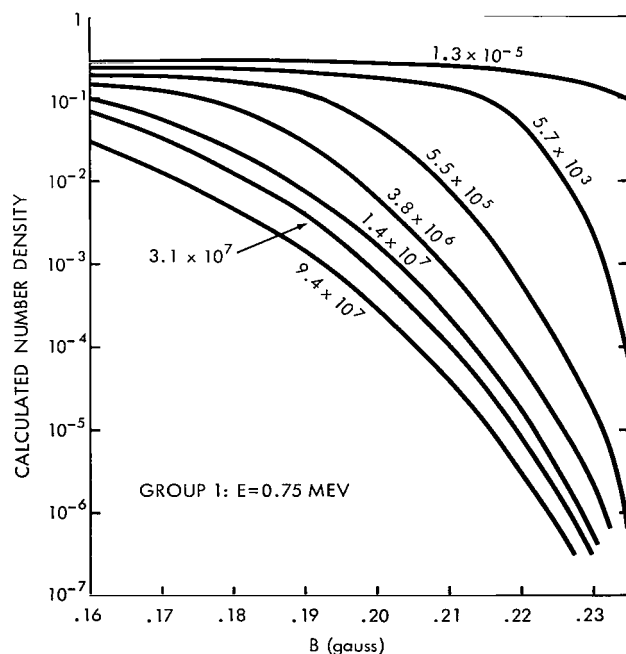


Figure 2—Calculated number density of $E = .75$ Mev electrons for $L = 1.25$ for various times after injection (Reference 2).

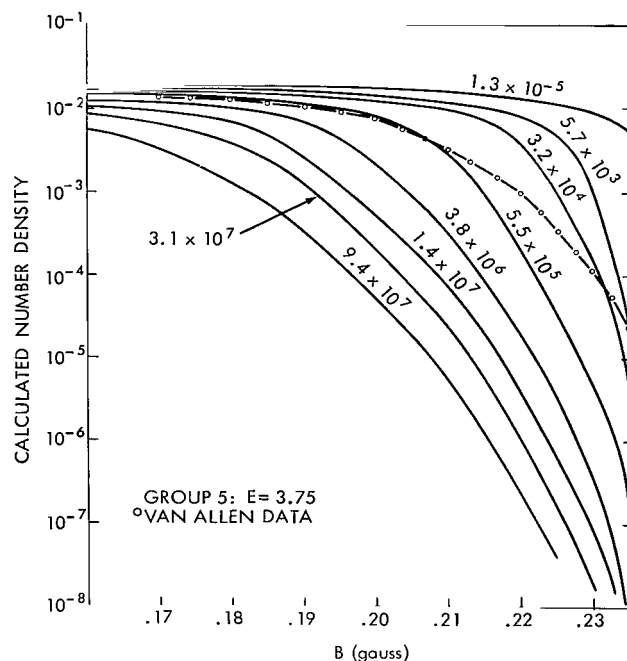


Figure 3—Calculated number density of $E = 3.75$ Mev electrons for $L = 1.25$ for various times after injection (Reference 7). The dotted curve labeled Van Allen Data is a smooth curve drawn through the Injun data (Reference 1) and is for $t \sim 10^5$ sec.

and in Figure 3 for $E = 3.75$ Mev. As is expected, the first particles to be lost are the ones at high B (or low altitude). Gradually the decay rate slows and the spatial distribution eventually reaches an equilibrium shape. For the equilibrium situation, scattering down the line is nearly balanced by scattering up the line so the decay proceeds slowly, being dominated by the scattering rate at the equator. Van Allen, Frank and O'Brien (Reference 9) on Injun I and Injun III (1962 β -2) have measured the decay of the Starfish electrons over a period of 4000 hrs (Figure 4). Also, McDiarmid, Burrows, Budzinski and Rose (Reference 10) have measured the decay of the Starfish electrons of $E > 3.9$ Mev by a GM counter on the Alouette satellite and this is shown in Figure 5. They find a decay constant of about 550 days for $B = .18$ and $L = 1.32$. The characteristics of the

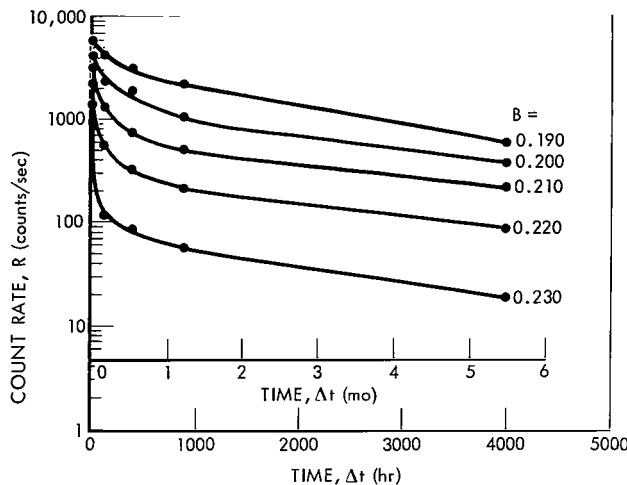


Figure 4—Experimental decay curves of the Starfish electrons for $1.25 \leq L \leq 1.35$ from Injun I and Injun III (Reference 9).

experimentally observed decay agreed with that which is expected from atmospheric decay.

During the process of atmospheric scattering the energy spectrum of the electrons changes. The lower energy electrons are more easily scattered and therefore lost first. Because of this, the fission energy spectrum hardens with time until an equilibrium spectrum is developed which has a peak at about 1.5 Mev. This process of spectral change is shown in Figure 6 for $L = 1.18$, as calculated by Welch, Kaufmann and Hess (Reference 7).

$L > 1.7$

The time history of the electrons for large L values after Starfish is quite different than for $L < 1.7$. The solid state detector on Telstar counting electrons of $E \sim .5$ Mev showed the time history given in Figure 7 (Reference 11) starting on July 10, which was the Telstar launch day and the day after Starfish. These decay curves are each for a narrow range of B of about .06 gauss. Figure 7 shows very clearly the time decay of a transient particle population down to something resembling a steady state population in a period of about three months. So even though Telstar did not observe the particle populations before the Starfish event, one can tell from its record that a large transient population was produced out past $L = 2.5$ at about the time of Starfish.

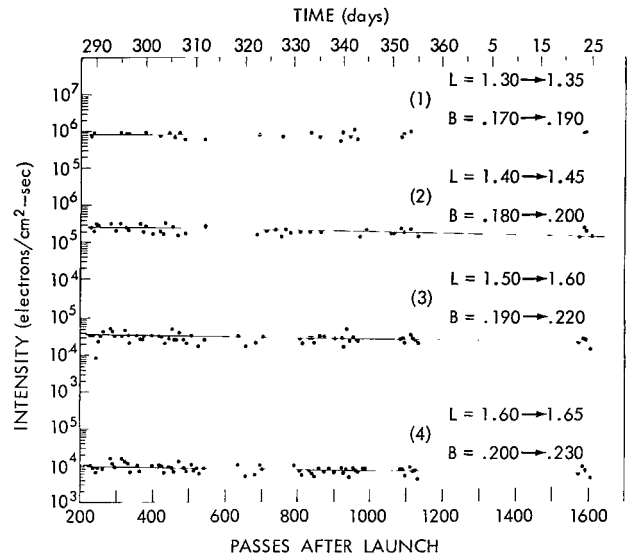


Figure 5—Experimental decay curves of the Starfish electrons for Alouette (Reference 10).

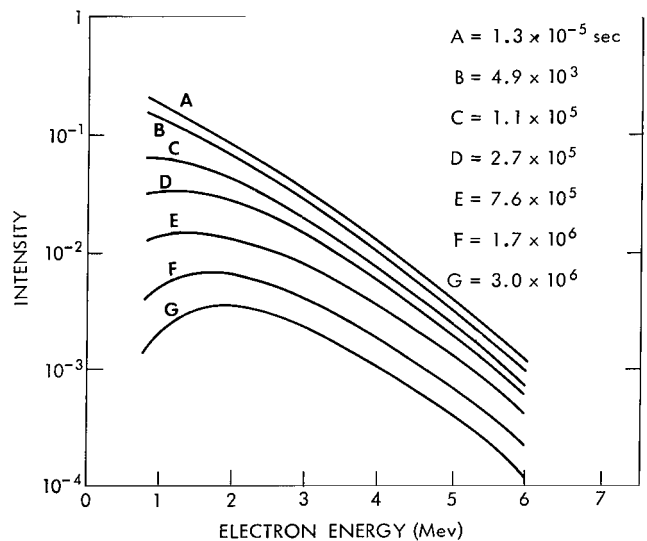


Figure 6—The calculated electron energy spectrum for $L = 1.18$ and $B = .20$ at various times after injection of a fission spectrum (Reference 7).

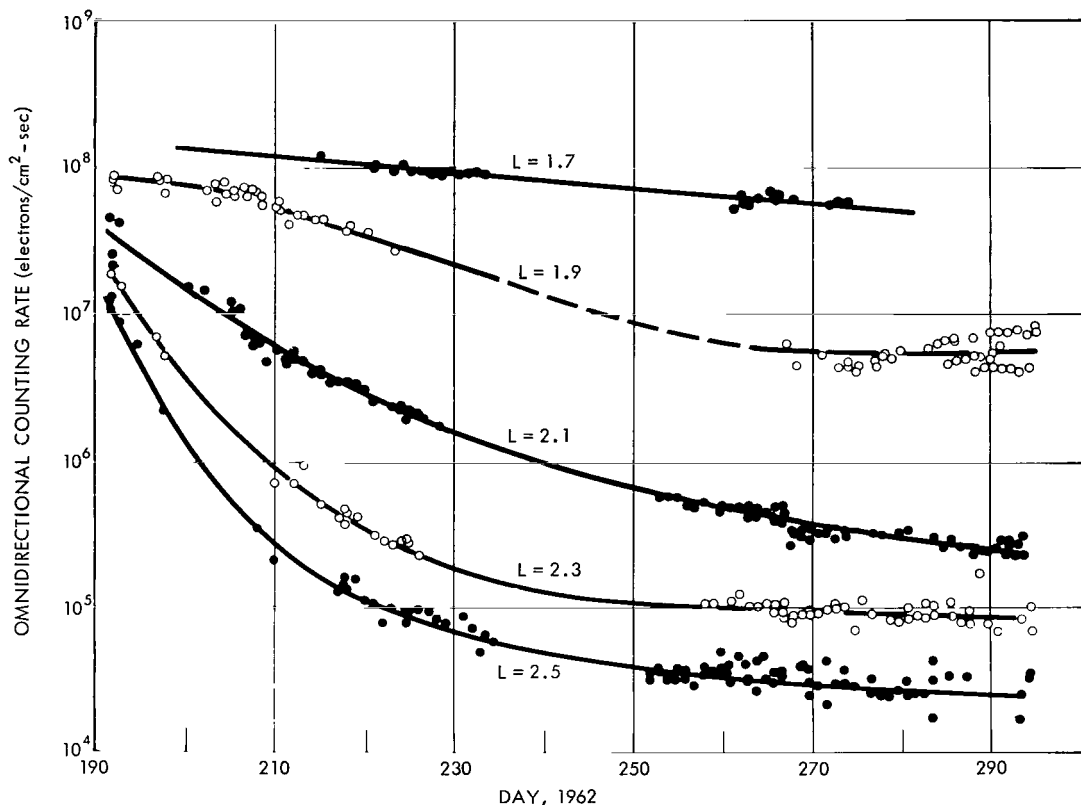


Figure 7—Experimental time histories of electrons of $E \sim 0.5$ Mev as measured by Telstar (Reference 11) for $L > 1.7$ starting on July 10, 1962.

Brown and Gabbe (Reference 4) calculated decay constants for $L > 2.0$ based on the initial slopes of the Figure 7 decay curves. Figure 8 shows values of the decay constant τ at different L values. At $L \sim 2.5$ the electron's mean life is only a few days. This is very different from the particle lifetime of years at $L \sim 1.4$. For $L > 1.7$ the decay rate gets markedly shorter than values expected from atmospheric decay. In Figure 8 the increase in τ for $L > 3$ may not be physically real, but may result from the fact that not many new particles were injected at these large L values by Starfish. In a region where no particles were added and a steady state population existed there would be no decay observed and $\tau \rightarrow \infty$.

There is no good explanation as to why the electron lifetimes are so short for $L > 1.7$. The process responsible for this seems to have a quite sudden onset at $L \sim 1.7$, and by $L \sim 2.2$, the electron lifetimes has been decreased roughly three orders of magnitude from that expected from atmospheric decay. The best candidate for this loss process is magnetic scattering. Welch and Whitaker (Reference 12) suggested that magnetic disturbances might break down the first adiabatic invariant and the particles would be magnetically scattered and lost. This requires frequencies of the disturbances of nearly a megacycle. Parker (Reference 13) has suggested that breakdown of the longitudinal invariant due to magnetic disturbances moving the particles mirror point would remove particles from the belt. This effect can be caused by waves of a few cps and therefore

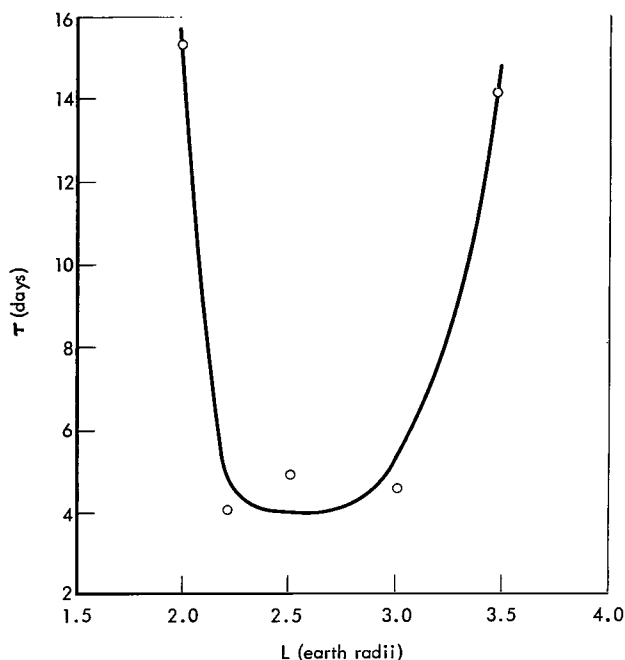


Figure 8—Experimental decay constants for Starfish electrons as measured in July 1962 by Telstar (Reference 4).

might be easier to make work. But whether such a process would have the sharp variation with L observed is uncertain. There is now no quantitative explanation for the short lifetime.

Brown and Gabbe (Reference 11) also observed the particles injected into the belt by the three USSR high altitude nuclear explosions of October 22, October 28, and November 1, 1962. Their instruments on Telstar studied the three explosions. Also, their instruments on the Explorer XV (1962 $\beta\lambda 2$) satellite launched on October 27 observed the October 28 and November 1 USSR explosions. The time histories for this period for their detector of $E > 1.9$ Mev on Explorer XV are shown in Figures 9, 10, and 11 for $L = 1.75$, 2.0 and 2.4 respectively. These time histories show a quite similar decay to the Telstar decay curves after Starfish. There is an initial redistribution of the flux along a field line for the low L

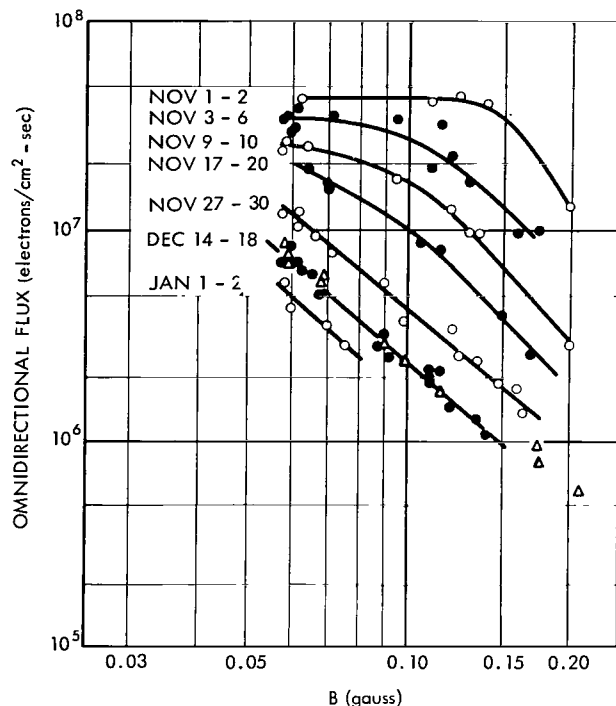


Figure 9—Experimental time histories of electrons of $E > 1.9$ Mev from Explorer XV (Reference 11) for $L = 1.75$. The triangles are for October 28 through 31 before the third USSR explosion.

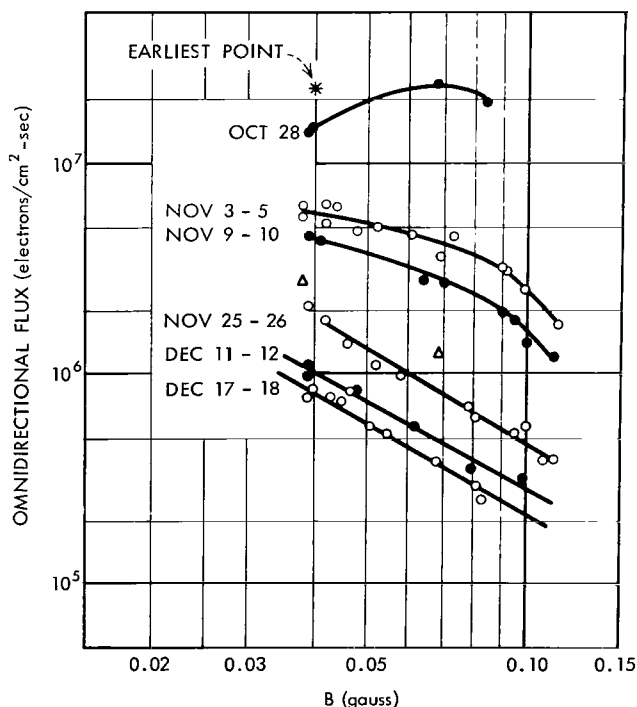


Figure 10—Experimental time histories of electrons of $E > 1.9$ Mev from Explorer XV (Reference 4) for $L = 2.0$.

lines followed by a decay with rather similar τ values to Figure 8. It seems that this decay is due to a usual condition in the magnetosphere and does not depend upon solar storms or other occasional events although such events may also be important.

PROTONS

It is well established that the high energy protons in the inner belt have long lifetimes. Freden and White (Reference 14) in an analysis of proton tracks in emulsion stacks deduced the proton lifetimes shown in Figure 12. But in spite of these long lifetimes, time changes have been seen in the heart of the inner belt. At $L = 1.3$ a gradual increase of a factor of three in the protons flux was observed during the year 1960 (Reference 15). This flux change can be understood in terms of the change in exospheric density during the solar cycle (Reference 16). We have calculated the solar cycle changes expected for $L = 1.25$ for several values of B .^{*} We start with the continuity equation (Reference 17):

$$\frac{dN(E)}{dt} = S(E) - L(E) + \frac{\partial}{\partial E} \left[N(E) \frac{dE}{dx} \frac{dx}{dt} \right],$$

but we will not assume equilibrium, so

$$\frac{dN(E)}{dt} \neq 0.$$

For the source term $S(E)$ we use the energy data from Hess, Canfield and Lingenfelter (Reference 18) and the time behavior from McDonald and Webber (Reference 19):

$$S(E) = \frac{.8E^{-2.0}}{\gamma^v \tau} f(t).$$

For the loss term, following Freden and White (Reference 14), we take

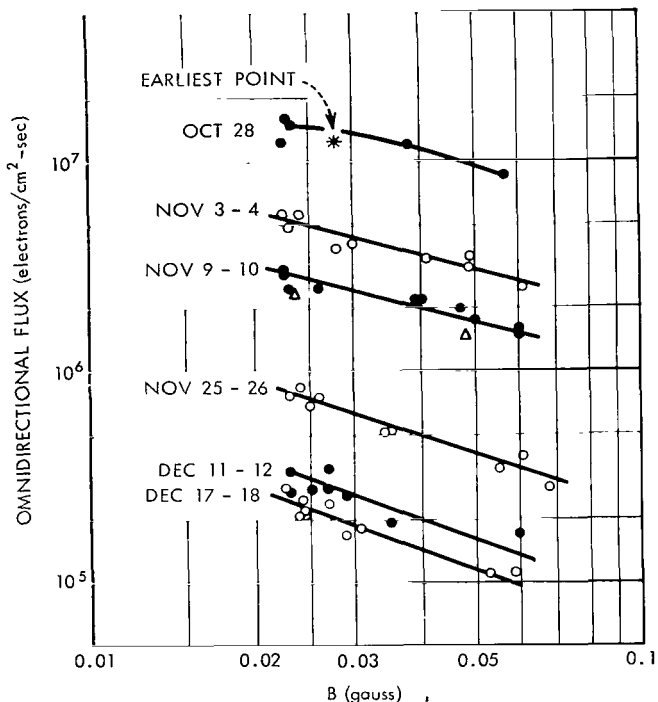


Figure 11—Experimental time histories of electrons of $E > 1.9$ Mev from Explorer XV (Reference 4) for $L = 2.4$.

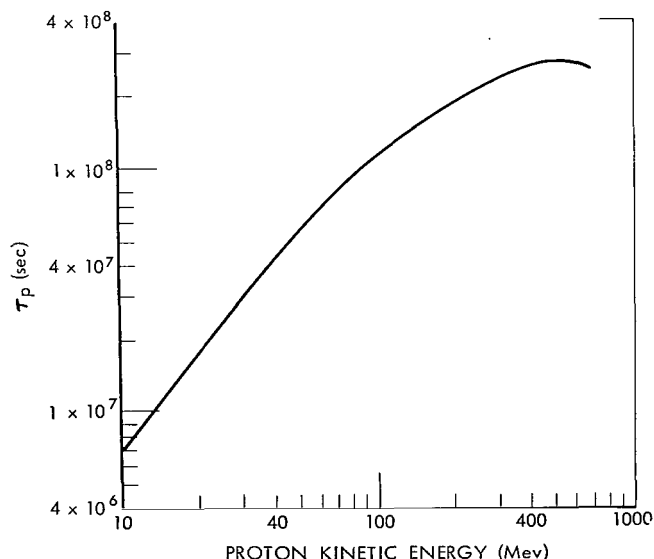


Figure 12—Decay constants of high energy Van Allen belt protons calculated by Freden and White (Reference 14).

^{*}R. Blanchard and W. N. Hess, Private Communication, 1963.

$$L = N(E) \sum_i n_i \sigma_i ,$$

where n_i is the atomic density of component i and σ_i is the inelastic cross section of component i .

We take the rate of energy loss,

$$\frac{dE}{dx} = \left(\frac{\rho}{\rho_N} \right) \left. \frac{dE}{dx} \right|_N$$

where dE/dx_N is the energy loss rate for NTP air of density ρ_N given in Aron, Hoffman, and Williams (Reference 20) and ρ is the actual average atmospheric density encountered by the protons. We have used the Harris and Priester (Reference 8) atmosphere and have averaged in local time and in longitude for each value of B and L and averaged along the bounce of the particle. These average densities ρ vary with time of the solar cycle.

Using this $\rho(t)$ we have calculated $N(E, t)$ from the equation for $dN(E)/dt$. Plots of $N(E, t)$ are shown in Figure 13 for several energies starting from $N = 0$ at $t = 0$. For high altitude > 2000 km the time variations are small because the protons lifetime is long compared to the solar

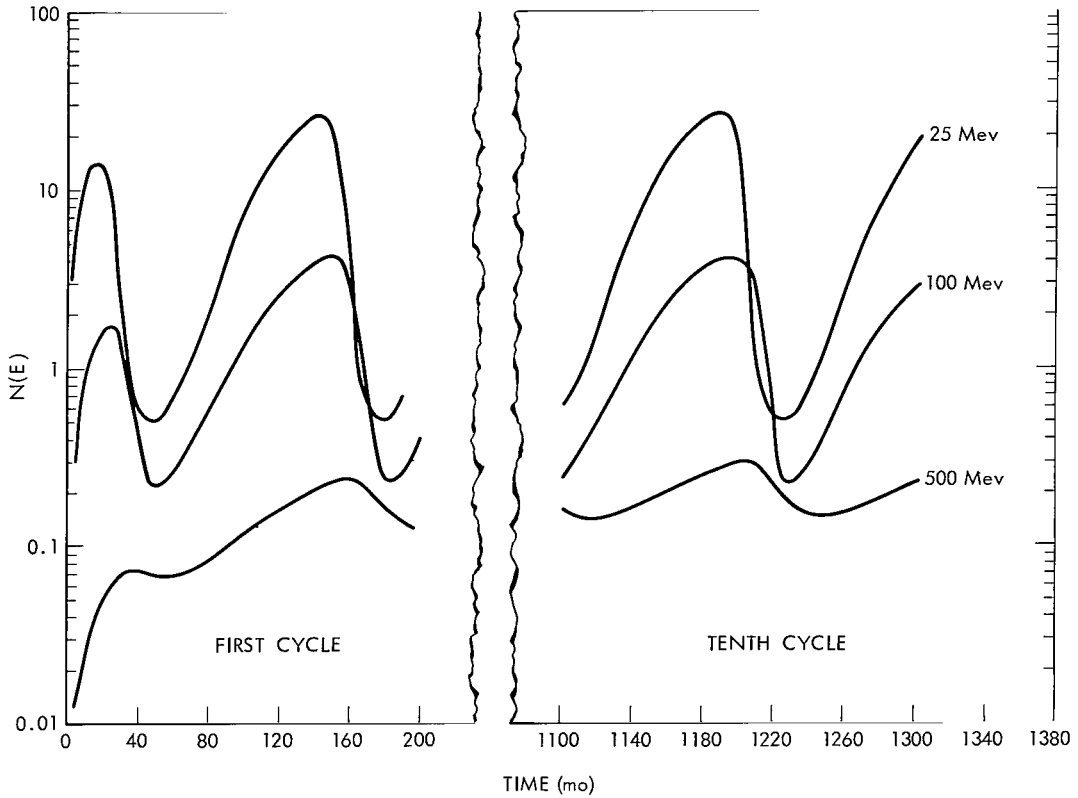


Figure 13—Time histories of protons of different energies for $L = 1.25$, $B = .209$, $h^{\min} = 400$ km starting from no flux and following the flux build up through the first solar cycle and also the tenth solar cycle (Blanchard and Hess 1963)*

*R. Blanchard and W. N. Hess, Private Communication, 1963

cycle. For low altitudes > 200 km the atmosphere does not change much with the solar cycle, so no large flux variations are seen. But for middle altitudes important changes do take place. The energy spectrum also changes significantly during the solar cycle. Figure 14 shows the spectrum at solar maximum and solar minimum for $B = .199$. Figure 15 shows the amplitude of the solar cycle flux variation for $L = 1.25$ for values of B and E . These fluctuations must take place if the protons have long lives because we know the exospheric density changes with time. The details of the changes will depend on the detailed characteristics of the atmosphere. The Harris and Priester atmosphere gives the best current values of the effect. There is not currently available very complete experimental information to use to

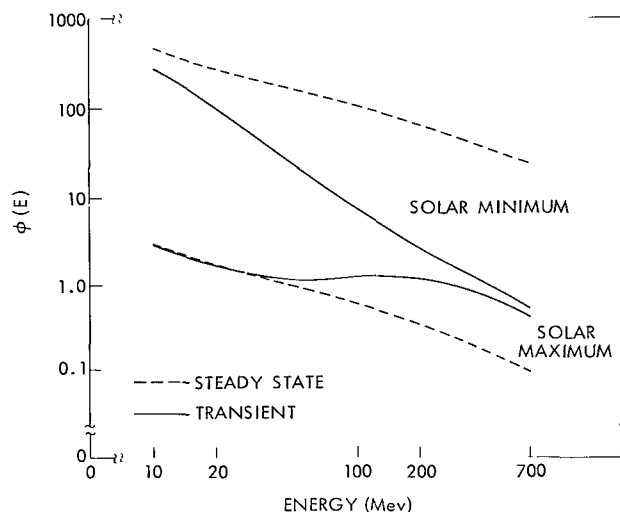


Figure 14—The proton energy spectrum at solar max and solar min for $L = 1.25$, $B = .199$, $h^{min} = 500$ km. The dashed curves are the spectra that would exist if the solar max and solar min atmospheres existed for long enough times for the problem to come to equilibrium (Blanchard and Hess 1963).*

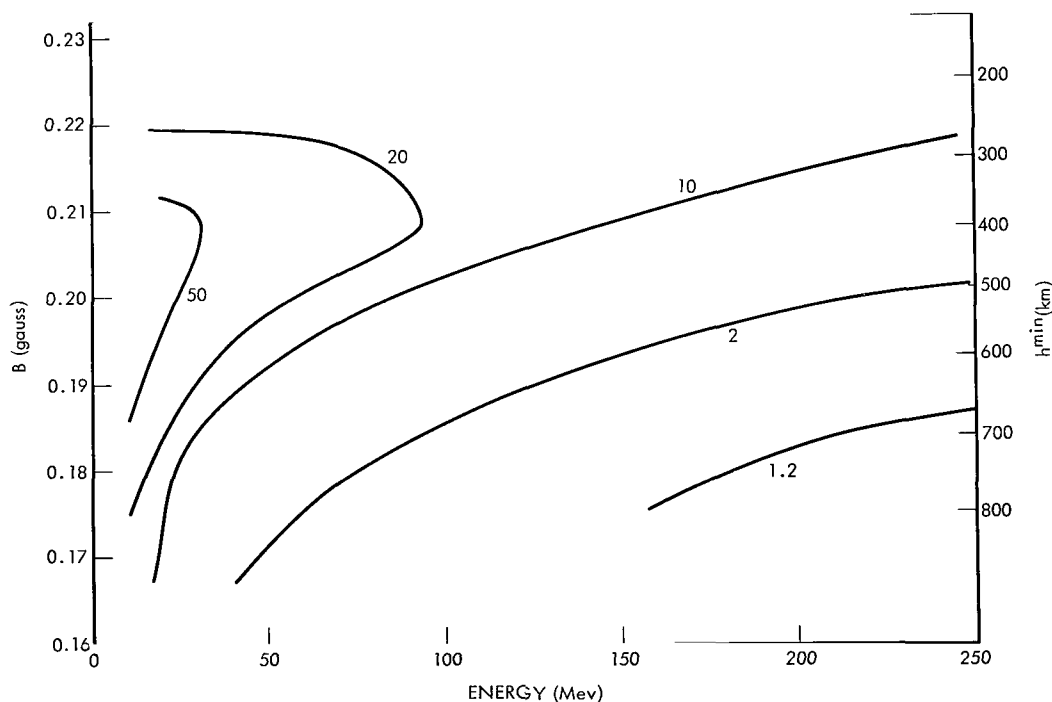


Figure 15—The amplitude of the solar min/solar max flux ratio for protons of different energies at different values of B for $L = 1.25$ (Blanchard and Hess 1963).*

*R. Blanchard and W. N. Hess, Private Communication, 1963.

compare with these calculations. When such data becomes available it may help improve the understanding of the upper atmosphere.

Filz, Holeman, and Yagoda (Reference 21) have analyzed nuclear emulsions flown on several low altitude satellites and found that the proton flux for $E_p > 55$ Mev was increased about a factor of 5 at 400 km shortly after Starfish. This is probably due to a redistribution of a small fraction of the trapped high energy protons by some process related to the explosion. This increase in proton population was temporary and the flux decayed back to the steady state value in a few months. Filz, Holeman, and Yagoda give the time for the 55 Mev protons to decay by a factor of 10 at 420 km as 110 days or a mean life $\tau \sim 5 \times 10^6$ sec.

If we assume most of the flux was encountered in the South Atlantic magnetic anomaly at $B = .210$, $L \sim 1.3$ and using the Harris and Priester $S = 100$ averaged atmospheric density $\rho = 10^6$, we get the lifetime for a 70 Mev proton from Freden and White (Reference 14):

$$\tau = \frac{7.5 \times 10^{10}}{\rho} E^{1.31} = 2 \times 10^7 \text{ sec}.$$

This gives only fair agreement with the experimental proton lifetime. It is also uncertain whether the decay at different altitudes proceeded at different rates, as it should according to the theory.

It is well established that cosmic ray neutrons produce the high energy protons in the inner Van Allen zone. Measurements show that these high energy protons are not present in the outer zone although there the neutron source will still make them. Some additional loss process must operate to remove them more rapidly from the outer zone than from the inner zone. Garmire (Reference 22) has recently analyzed the count rate of the Cerenkov counter on the Explorer XI (1961 ν 1) satellite to study protons of $E_p > 350$ Mev. This is part of the detector used to study high energy γ -rays in space, but it also responds to trapped high energy protons. Garmire compared his count-rate contours with those of McIlwain (Reference 23) for $E_p > 43$ Mev to show that there are relatively fewer high energy protons at large L values. One process which could produce such a situation would be a breakdown of the first adiabatic invariant J_μ involving the constancy of the particles magnetic moment. Welch and Whitaker (Reference 12) first suggested that hydromagnetic waves might break down this invariant. Lenchek and Singer (Reference 24) following calculations of Garren, et. al. (Reference 25) proposed that for high enough energy protons in a static dipole field the Alfven approximation might not hold and the particles would be lost.

Garmire (Reference 22) has numerically computed trapped-proton orbits in a dipole field and also in a Finch and Leaton field and has obtained an effective cutoff energy for trapped protons in both fields as a function of position in the field (Figure 16). It happens, interestingly, that the cutoff energies are considerably lower for the Finch and Leaton field. Garmire's comparison of the cutoff energy calculations with the experimental data shows that this process of the breakdown of J_μ very likely contributes to the loss of high energy protons at large L . This might even be the sole loss process if the variation with L is rapid enough. If this process is responsible for the loss of high energy outer zone protons then the outer edge of the inner zone should not change appreciably with time in the solar cycle because this loss process is not time dependent.

CONCLUDING REMARKS

Last year, for the first time, we have obtained definitive information on trapped electron lifetimes:

1. For $L < 1.7$ the dominant loss process is atmospheric scattering and the particle lifetimes are long. At $L = 1.3$ the electrons' mean life is about a year. The scattering process creates an equilibrium flux distribution along a field line and an equilibrium energy spectrum;

2. For $L > 1.7$ the electrons' lifetimes get much shorter than that expected from atmospheric scattering. At $L = 2.5$ the electrons mean life is about one week. The loss appears to be gradual in time and an equilibrium flux distribution appears for $1.7 < L < 2.5$. The nature of the loss process operating here is not understood.

New information also helps understanding of proton time histories. Inner zone protons made by neutron decay have long lifetimes, but they will show time changes too:

3. At several hundred kilometers altitude calculations show that the proton population should change more than an order of magnitude during the solar cycle due mostly to changes in the exospheric density. This process also changes the proton energy spectrum. At high altitudes the proton lifetime is long compared to the solar cycle and the effect is averaged out. Fragmentary experimental information tends to confirm this.

4. A direct measurement at 420 km of the lifetime of $E > 55$ Mev protons displaced by the Starfish explosion agrees only fairly well with the lifetime value calculated on the basis of atmospheric slowing down.

5. High energy protons do not appear in the outer zone. Calculations show now that they may be lost because their Störmer orbits are not trapped. The non-dipolar nature of the field is important in carrying out these calculations. The result of the calculations agrees reasonably well with experimental data from Explorer XI. This loss process would be constant in time and so the outer edge of the inner belt should not vary much during the solar cycle.

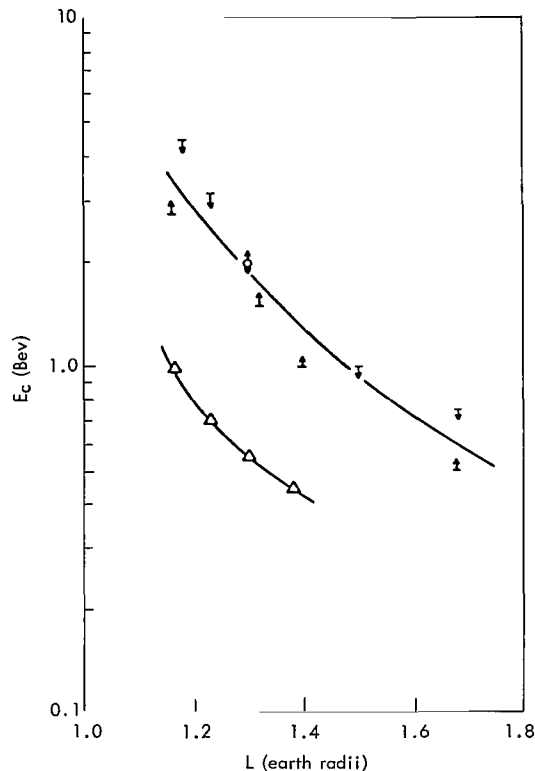


Figure 16—Computed values of the cut-off energy E_c for high energy trapped protons for a dipole field and for a Finch and Leaton field (Reference 22).

REFERENCES

1. O'Brien, B. J., Laughlin, C. D., and Van Allen, J. A., "Geomagnetically Trapped Radiation Produced by a High-Altitude Nuclear Explosion on July 9, 1962," *Nature*, 195(4845):939-942, September 8, 1962.
2. Pieper, G. F., Williams, D. J., and Frank, L. A., "Traac Observations of the Artificial Radiation Belt from the July 9, 1962, Nuclear Detonation," *J. Geophys. Res.* 68(3):635-640, February 1, 1963.
3. Durney, A. C., Elliot, H., Hynds, R. J., and Quenby, J. J., "Satellite Observations of the Energetic Particle Flux Produced by the High-Altitude Nuclear Explosion of July 9, 1962," *Nature*, 195(4848):1245-1247, September 29, 1962.
4. Brown, W. L. and J. D. Gabbe, Electron Distribution in the Earth's Radiation Belts during July 1962 as Measured by Telstar, *J. Geophys. Res.* 68(3):607-618, February 1, 1963.
5. Hess, W. N., Bloom, S., Mann, L., Seward, F., and West, M., "Electron Loss Rate from the Outer Radiation Belt," in *Space Research III*, ed. by W. Priester, Amsterdam: North-Holland Publishing Co., 1963, pp. 477-485.
6. MacDonald, W. M., and Walt, M., "Distribution Function of Magnetically Confined Electrons in a Scattering Atmosphere," *Ann. Phys.* 15(1):44-62, July 1961.
7. Welch, J. A., Jr., Kaufmann, L., and Hess, W. N., "Trapped Electron Time Histories for $L = 1.18$ to $L = 1.30$," *J. Geophys. Res.* 68(3):685-700, February 1, 1963.
8. Harris, I., and Priester, W., "Theoretical Models for the Solar-Cycle Variation of the Upper Atmosphere," NASA TN D-1444, August 1962.
9. Van Allen, J. A., Frank, L. A., and O'Brien, B. J., "Satellite Observations of the Artificial Radiation Belt of July 1962," *J. Geophys. Res.* 68(3):619-627, February 1, 1963.
10. McDiarmid, I. B., Burrows, J. R., Budzinski, E. E., and Rose, D. C., "Satellite Measurements in the "Starfish" Artificial Radiation Zone," Div. of Pure Physics, National Research Council, Ottawa, Canada (To be published 1963).
11. Brown, W. L., Gabbe, J. D., and Rosenzweig, W., "Results of the Telstar Radiation Experiments," *Bell Systems Technical Journal* 42(4, pt. 2):1505-1559, July 1963.
12. Welch, J. A., Jr., and Whitaker, W. A., "Theory of Geomagnetically Trapped Electrons from an Artificial Source," *J. Geophys. Res.* 64(8):909-922, August 1959.
13. Parker, E. N., "Effect of Hydromagnetic Waves in a Dipole Field on the Longitudinal Invariant," *J. Geophys. Res.* 66(3):693-708, March 1961.
14. Freden, S. C., and White, R. S., "Particle Fluxes in the Inner Radiation Belt," *J. Geophys. Res.* 65(5):1377-1383, May 1960.

15. Pizzella, G., McIlwain, C. E., and Van Allen, J. A., "Time Variations of Intensity in the Earth's Inner Radiation Zone," *J. Geophys. Res.* 67(4):1235-1254, April 1962.
16. Hess, W. N., "Discussion of Paper by Pizzella, McIlwain, and Van Allen 'Time Variations of Intensity in the Earth's Inner Radiation Zone. October 1959 Through December 1960'," *J. Geophys. Res.* 67(12):4886-4887, November 1962.
17. Singer, S. F., "Trapped Albedo Theory of the Radiation Belt," *Phys. Rev. Letters* 1(5):181-183, September 1, 1958.
18. Hess, W. N., Canfield, E. H., and Lingenfelter, R. E., "Cosmic-Ray Neutron Demography," *J. Geophys. Res.* 66(3):665-677, March 1961.
19. McDonald, F. B., and Webber, W. R., "A Study of the Rigidity and Charge Dependence of Primary Cosmic Ray Temporal Variations," *J. Phys. Soc. Japan* 17 (Suppl. A II):428-435, January 1962.
20. Brown, W. L., and Gabbe, J. D., "The Electron Distribution in the Earth's Radiation Belts During July 1962 as Measured by Telstar," *J. Geophys. Res.* 68(3):607-618, February 1963.
21. Filz, R., Holeman, E., and Yagoda, H., "Variation of the Directional Flux of Slow Trapped Protons," *AGU Trans.* 44(1):78, March 1963.
22. Garmire, G., "Geomagnetically Trapped Protons with Energies Greater than 350 Mev," *J. Geophys. Res.* 68(9):2627-2638, May 1, 1963.
23. McIlwain, C. E., "Coordinates for Mapping the Distribution of Magnetically Trapped Particles," *J. Geophys. Res.* 66(11):3681-3691, November 1961.
24. Lenchek, A. M., and Singer, S. F., "Geomagnetically Trapped Protons from Cosmic-Ray Albedo Neutrons," *J. Geophys. Res.* 67(4):1263-1287, April 1962.
25. Garren, A., Riddell, R. J., et al., "Individual Particle Motion and the Effect of Scattering in an Axially Symmetric Magnetic Field," in *Proc. Second U.N. Internat. Conf. on Peaceful Uses of Atomic Energy. Theor. and Exper. Aspects of Controlled Nuclear Fusion, Geneva: United Nations, p. 65, 1958.*

THE SOLAR SPECTRUM FROM 50 A TO 400 A

by

W. M. Neupert, W. E. Behring and J. C. Lindsay

Goddard Space Flight Center

SUMMARY

A scanning monochromator, mounted as a pointed experiment on OSO-1, has been used for observations of solar extreme ultraviolet radiation from 50 to 400 A. The period of observation was sufficient to observe a slowly varying component having a period of approximately 27 days and correlating with solar activity. The enhancement of radiation during periods of activity was observed to vary from line to line in the spectrum, depending upon the origin of the line in the solar atmosphere. Data showed an increase (33%) in the He II Lyman-alpha (304 A) flux, integrated over the entire solar disk during a period when the Zurich Provisional Relative Sunspot Number increased from zero (11 March 1962) to a maximum of 94 (22 March 1962). Enhancements of approximately a factor of four were observed for the 284 A (Fe XV) and the 335 A (Fe XVI) lines.

INTRODUCTION

A grazing incidence spectrometer has been flown as a pointed experiment on OSO-1 (1962 $\zeta 1$) to monitor the extreme ultraviolet spectrum of the sun. Over six thousand spectra were obtained at the rate of about 100 per day from March through May 1962, corresponding to nearly three solar revolutions. Intermittent operation has subsequently provided spectra more than one year. This paper presents, in a condensed form, the variations observed in three of the more reliably identified lines of the spectrum: 284 A (Fe XV), 304 A (He II) and 335 A (Fe XVI).

The schedule of reduction of telemetry records was designed to provide a coarse look (several orbits per day) throughout the three month period of continuous observation. This approach is not suited for the detailed study of a particular event for which one must have continuous data over a period of hours. Therefore, transient phenomena on the sun are only now being studied as data reductions become more complete and the results will be presented in a future paper.

DESCRIPTION OF SPECTROMETER

During operation the spectrometer was pointed at the center of the solar disk, within approximately two minutes of arc. At this orientation, radiation from the entire solar disk and inner

corona passed directly through the entrance slit and struck a concave grating mounted in grazing incidence, the angle of incidence being 88° . The grating, an original ruled in a special glass by the Nobel Institute in Stockholm, had 576 lines per millimeter on a blank with one meter radius of curvature. The exit slit and detector were mounted on a carriage which was driven on a circular rail so that the exit slit scanned along the Rowland Circle, where the spectrum was focused, from 10 - 400 Å. The plane of the exit slit was approximately perpendicular to the diffracted ray at all positions along the track, thereby keeping the spectral passband nearly constant for all angles of diffraction. The $50\ \mu$ entrance and exit slits provided a spectral passband of 1.7 Å and permitted resolution of lines 0.85 Å apart. The detector was a windowless photomultiplier developed by the Bendix Corporation specifically for use in this spectrometer. A tungsten photocathode was chosen to minimize response to wavelengths above 1500 Å, and to reduce changes in sensitivity due to variations in the emission properties of the cathode.

CALIBRATION OF THE SPECTROMETER

The instrument was calibrated by: (1) exposing the entire spectrometer to a beam of monochromatic radiation of known intensity; or (2) by evaluating the essential components of the spectrometer (grating, detector, etc.), and then computing the sensitivity of the instrument. The first method was used at 44 Å using a proportional counter for determining the source intensity. The second method was applied at longer wavelengths (80-400 Å).

In addition, a comparison was made of the solar fluxes obtained against the fluxes measured by Hall, Damon and Hinteregger (Reference 1) with a calibrated rocket instrument. The comparison could only be made in the region of overlap, 250 to 400 Å, and would be meaningful only if the solar radiation was the same. The 2800 Mc mean daily flux recorded by the National Research Council, Ottawa, Canada, was used as an independent estimate of solar flux to choose the satellite data for the comparison.

A best fit was made between these methods of obtaining a calibration and yielded values of 8.0×10^5 photons/cm²-count at 335 Å and 4.2×10^5 photon/cm²-count at 284 Å.

PRESENTATION OF DATA

Figure 1 presents a typical scan obtained over the region, 170 to 400 Å. Several factors reduce the usable spectral range of the spectrometer from its nominal range of 10 to 400 Å. At wavelengths below 100 Å the decreasing sensitivity of the spectrometer combined with an increase in scattered light upon approaching the central image made it impossible to distinguish a reliable spectrum on a single scan. However, a combination of several scans, using cross-correlation techniques, has shown the apparent existence of a line emission spectrum in the region from 50 to 100 Å. At wavelengths above 342 Å the second order images of intense spectral lines (observed in the first order above 171 Å) obscure a considerable amount of interesting data. In Figure 1 this effect is indicated by cross-hatching those first order lines which have strong second order

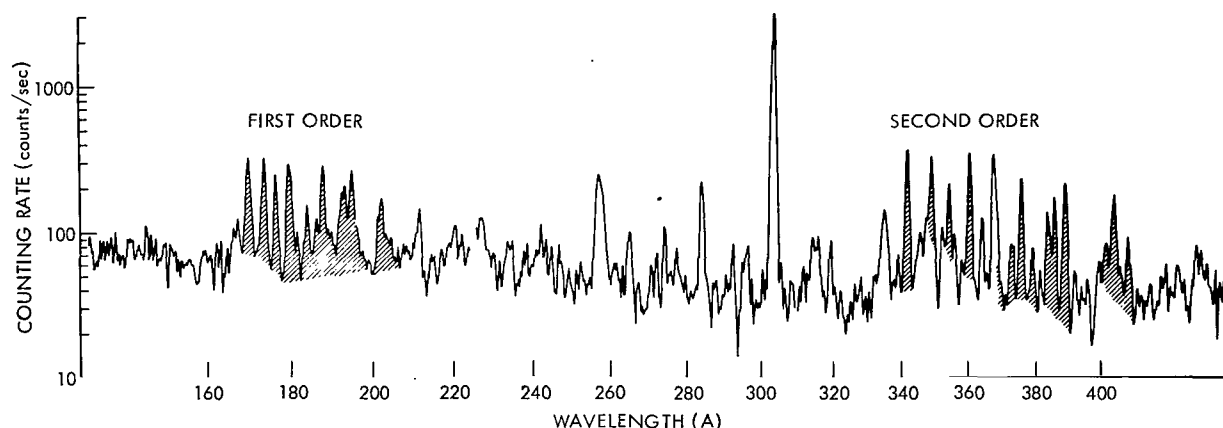


Figure 1—Solar spectrum from 170 to 400 Å with second order line images indicated.

counterparts in the recorded spectrum. These second order images were less prominent in earlier rocket results, thus there is considerable dissimilarity between the rocket and satellite spectra above 342 Å (Reference 2). For these reasons the obviously usable range of the instrument can be considered to be from 170 to 340 Å—a range which can be extended, with special precautions, to cover the interval from 50 to 400 Å.

The brightest emission line in the region from 170 to 340 Å is the Lyman-alpha line of ionized helium at 304 Å. In addition, numerous other emission lines appear with combined flux comparable to, or somewhat greater than, that of the helium line. Resonance lines of heavy ions (Mg through Fe) are expected in this region, leading to attempts (References 2 and 3) to identify the more prominent features of the spectrum in terms of such lines. The difficulty of positive identification can be appreciated more if, for example, we realize that the resonance lines of all stages of ionization of iron from Fe X through Fe XVI, with the exception of Fe XV, are expected in the small wavelength interval from 335 to 390 Å (Reference 2). The overlapping of these resonance multiplets combined with second order contamination of shorter wavelengths makes positive identification a formidable task. The resonance lines of Fe X through Fe XIV have not been identified in the extreme ultraviolet (EUV) spectrum although their intensity as predicted by Ivanov-Kholodny and Nikolsky (Reference 4) should permit their observation. Tousey (Reference 5), working with a spectrum having higher resolution, reports that no Fe XIV multiplet can be found in his record. Because of these difficulties, discussion will center around three of the more intense and more reliably identified lines of the spectrum: the Fe XV ($3s^2\ ^1S_0 - 3s\ 3p\ ^1P_1$) line at 284 Å; the Fe XVI ($3s\ ^2S_{1/2} - 3p\ ^2P^0_{3/2}$) line at 335 Å; and, in addition, the He II ($1s\ ^2S_{1/2} - 2p\ ^2P^0_{3/2, 1/2}$) line at 304 Å. The location of these lines is indicated in Figure 2.

TIME VARIATIONS OF THE EUV SPECTRUM

The months of March and April 1962 were auspicious for a study of the solar EUV spectra in that observations could be made on both a quiescent and a disturbed solar atmosphere. During the

second week in March the sun was especially quiet—the sunspot number being zero on 11 March. As the month progressed the solar rotation carried several centers of activity across the visible hemisphere of the sun. Definite enhancements in the solar spectrum were associated with these centers of activity.

Figure 2 presents two scans of the EUV spectrum which were obtained approximately ten days apart. During the first of these observations (13 March) only one small region of activity was present on the solar disk. In spite of this low level of activity it is observed that the Fe XV and Fe XVI lines persist as two of the more prominent features of the spectrum. The second spectrum

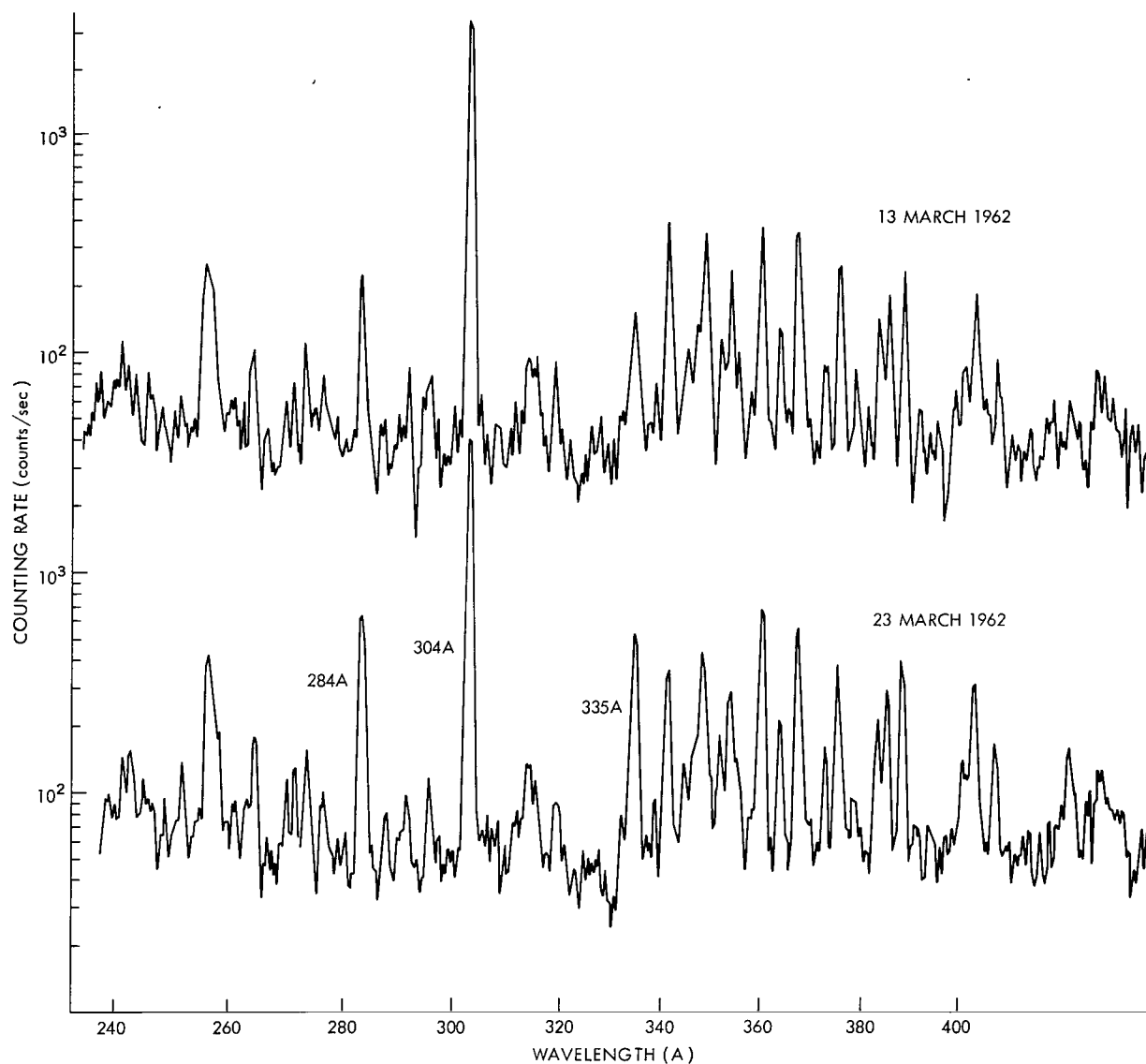


Figure 2—Comparison of two spectral scans taken under different solar conditions.

(23 March) was obtained while several large and well developed centers of activity were present on the disk. Comparing these two spectra we observe that the emission lines have increased in intensity but not all by the same amount. The Fe XV and XVI lines, already prominent even in the absence of solar activity, have increased in intensity appreciably more than any other line observed with certainty in this spectral range. The He II line has also increased, but by a lesser amount.

Time variations of these three lines as observed for the first 1066 orbits of operation are given in Figure 3, in which each datum point represents the average of one orbit's observations

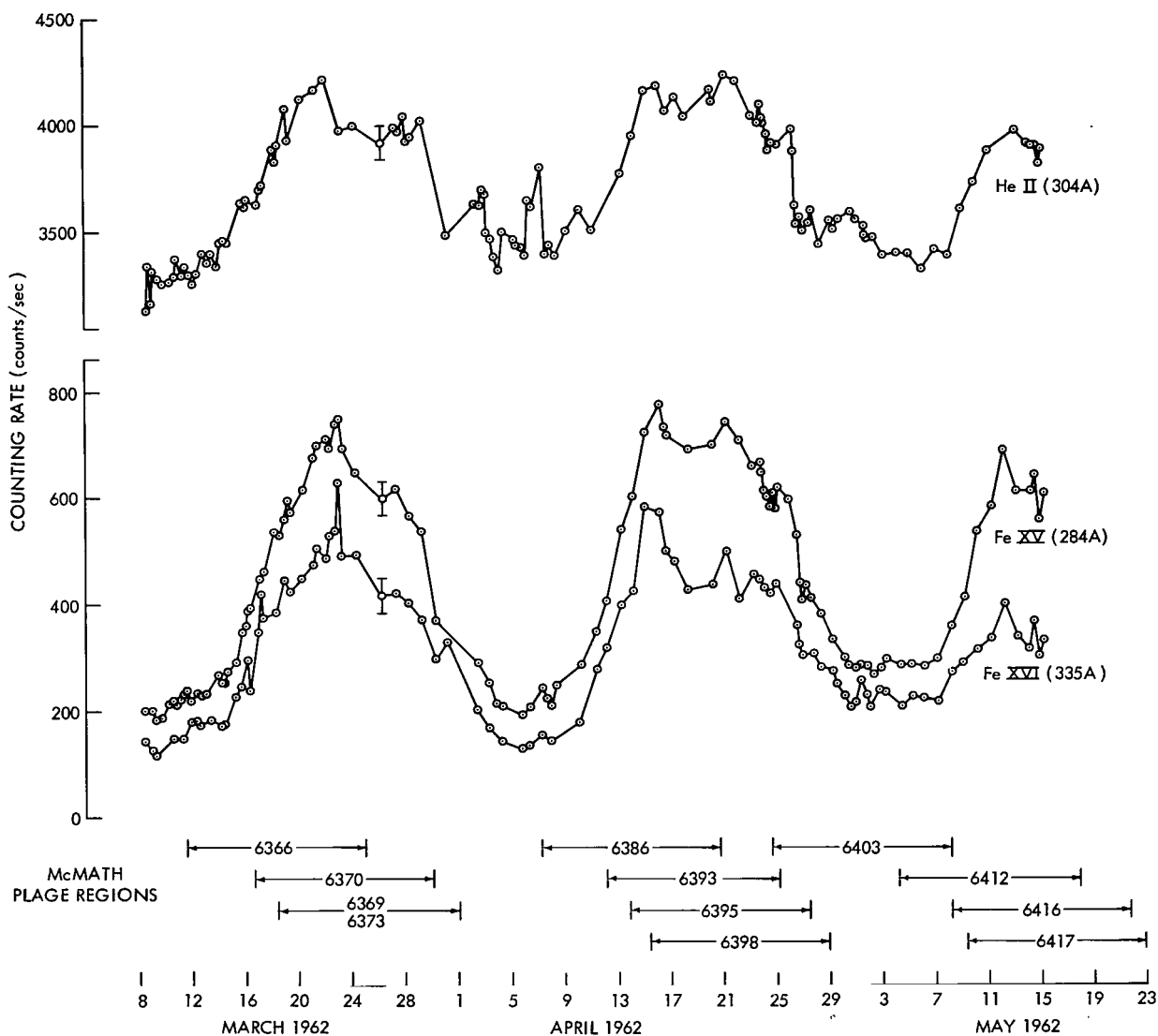


Figure 3—OSO-1 data for three spectral lines compared with the appearance and disappearance of major plage areas.

(six to eight scans). Error bars indicating one standard deviation in the data are given for each wavelength. Also indicated are the times of appearance and disappearance of the major plage areas as cataloged by the McMath-Hulbert Observatory. The first increase in the counting rates above the "quiet sun" values is associated with the appearance of McMath Plage No. 6366 on the east limb on 11 March. The slope of the He II curve is observed not to change appreciably on 17 March as several more prominent plages appear on the limb, although their appearance is obvious in the radio data. The counting rate for the He II (304 Å) line increases gradually to a maximum on 23 March, after which it drops rather abruptly to an apparent plateau. This sudden drop cannot be unambiguously attributed to the disappearance of plage region 6366 on the west limb, for it follows quite directly after an unusual flare of importance 3 observed in plage region 6370 on 22 March, for which data are not given in Figure 3. A gradual decline in readings is observed from 29 March to 7 April. A similar enhancement, followed by a return to near pre-plage rates, occurred in April. Since the spectrometer did not carry an internal standard (e.g., radioactive source) it is impossible to state positively that its counting characteristics did not change over the period of observations. The consistent behavior of the data, however, as demonstrated in Figure 3, leads to the conclusion that no significant change in sensitivity occurred throughout the period of observation. (Subsequent analysis of real time data after one year in orbit supports this conclusion, even for the longer time interval.)

Also shown in Figure 3 are the variations with solar activity of the coronal Fe XV (284 Å) and Fe XVI (335 Å) lines, the relative increases being considerably larger than for the He II (304 Å) line. A definite, although small, enhancement associated with the appearance of plage No. 6366 is observed in both the Fe XVI and Fe XV lines. The possibility exists that the coronal emissions appear slightly earlier as might be expected since the coronal emission must take place at greater heights than the calcium radiation. The most obvious increase in intensity of these lines is associated with the appearance, in succession, of plage areas numbered 6370, 6369, and 6373 on 17 March through 19 March. The counting rates then increased gradually throughout this period indicating that the enhanced emission was not from a point source but rather from an extended volume having as its base an area at least as large as the underlying calcium plage. The disappearance of area 6366 on 25 March results in a slight decrease in counting rates, followed by a general decline from 29 March through 3 April as the other plage areas are carried off the visible hemisphere of the sun by the solar rotation.

Although the horizontal scale in Figure 3 is inadequate for the display of transient phenomena, at least one interesting event, associated with a flare of importance 3, on 22 March, can be discerned. This flare was unusual in that the ionospheric effects produced by it were more nearly characteristic of a small (importance one) flare. An enhancement was observed at 304 Å (not plotted) simultaneously with the visible flare, but not at 335 Å or 284 Å. However, at the latter wavelengths a significant enhancement was noted one or two orbits after the visible maximum. The peak point at 335 Å lies at eight standard deviations from the mean of the day's observations before the flare and represents a nearly certain change in the EUV flux. Further analysis of this event covering the major lines of the spectrum will be presented in a future paper.

The relationship of these observed counting rates to several ground-based measurements of solar activity is presented in Figures 4 and 6. In Figure 4, the He II radiation is compared with daily values of the solar flux at 2800-Mc, and with the Zurich Provisional Relative Sunspot Number (ZPRSN). Also shown is an estimate of the calcium plage area, each area being weighted by the estimated intensity of the area on a scale from 1 to 5. Values for this computation were supplied by the McMath-Hulbert Observatory.

A more detailed comparison is made in Figure 5 in which the radio and He II fluxes have been adjusted by dividing each observation by the rate observed for the "quiet sun". In addition, the Ca^+ plage intensity has been adjusted to coincide with the 2800 Mc enhancement on 21 March. This

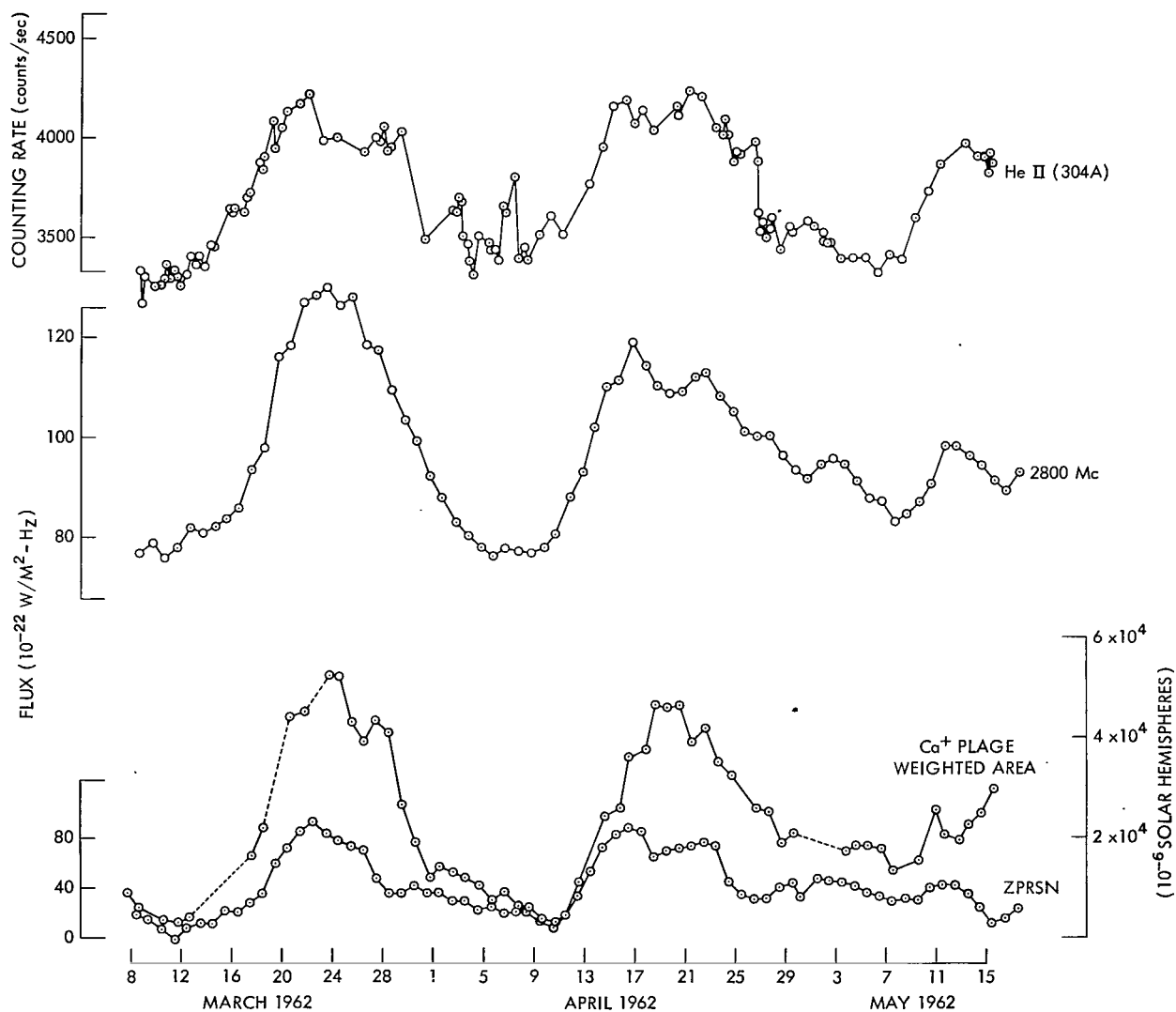


Figure 4—Relationship of observed counting rates for the He II Lyman-alpha line to ground-based measurements of solar activity.

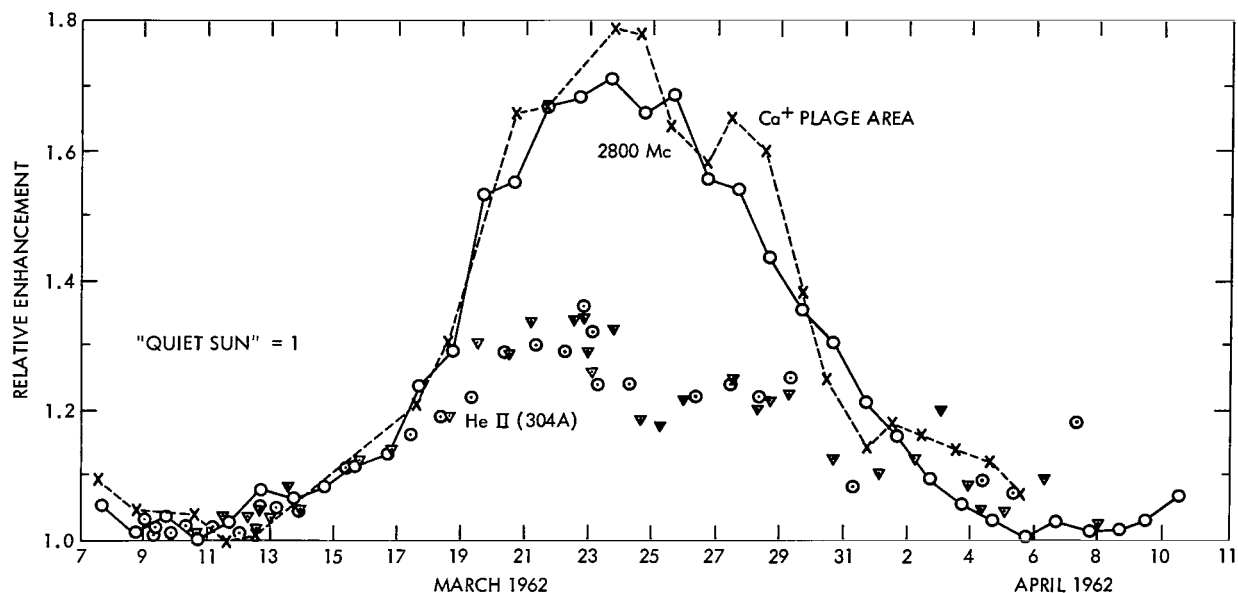


Figure 5—Comparison of 304 Å data, normalized for a "Quiet Sun", with calcium plage data and 2800 Mc radio observations.

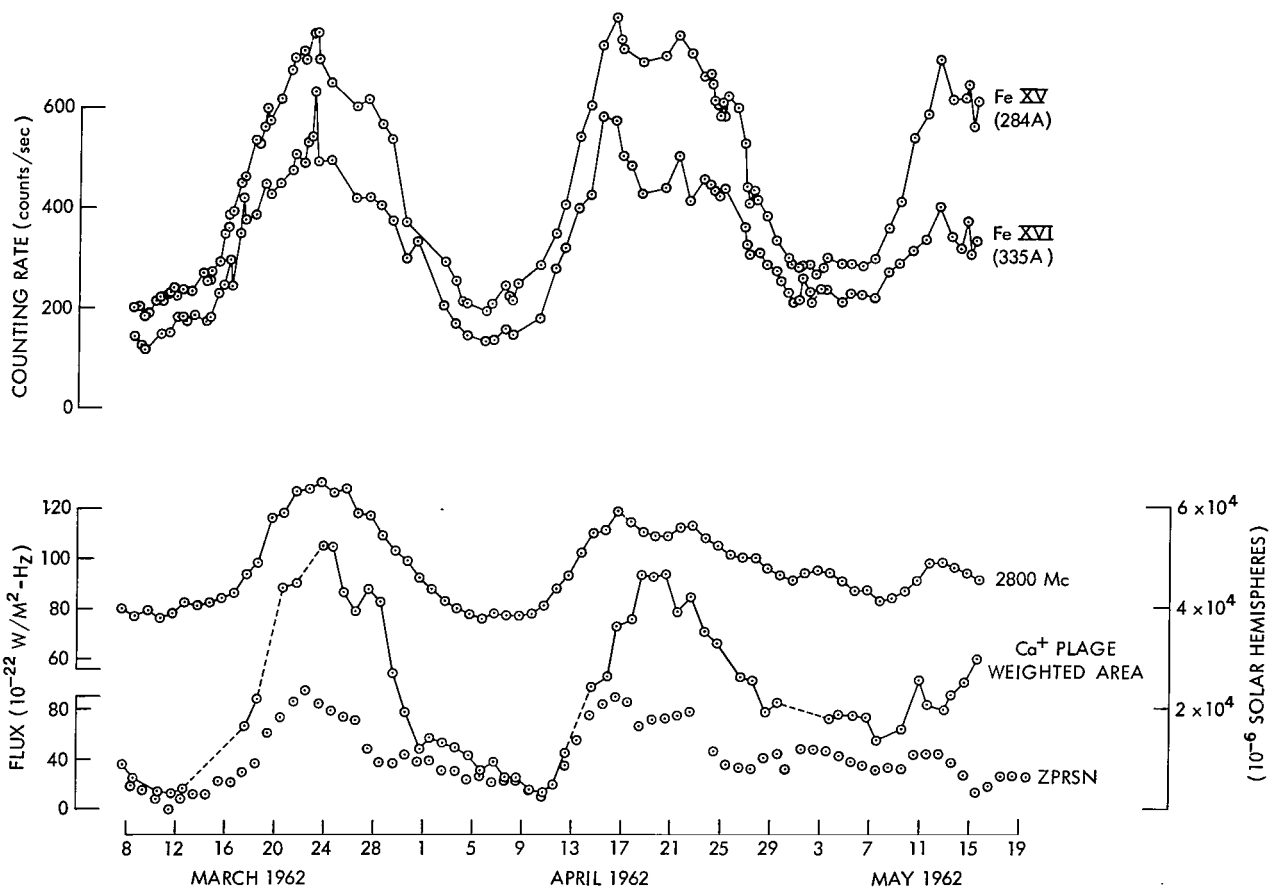


Figure 6—Relationship of observed counting rates for the 284 Å and 335 Å lines to ground-based observations.

plot shows more clearly the close relationship which has been known to exist for some time between the 2800-Mc radiation and the plage areas. The divergences of the He II (304 Å) line from both of these curves is also shown. In Figure 6 the daily values of solar flux at 2800 Mc and the Zurich Provisional Relative Sunspot Number are compared with radiation due to the coronal lines of Fe XV (284 Å) and Fe XVI (335 Å). The estimated calcium plage intensity is also given.

DISCUSSION

The spectral lines chosen for presentation here were selected because they are reliably identified with particular ions, not because they convey better than any other line in the spectrum the plage-associated changes in solar flux. In terms of fractional changes in intensity, these three lines represent the extremes which have thus far been observed in the spectral region from 171 to 400 Å; only a few faint lines have smaller non-flare variations than the He II Lyman-alpha line, while no other lines have increases as great as those observed for 284 and 335 Å. A summary of the average increases in counting rates for the period from 9 March to 23 March 1962, a period of increasing solar activity, is given in Table 1. The increase, weighted by the intensity of each line, is computed for the range from 171 to 305 Å, using sixty reliably observed lines. The increase in the range from 305 to 400 Å can only be estimated because of the masking effect of second order images above 342 Å. The values given in Table 1 are, of course, appropriate only for the particular interval of time for which they were computed.

The initial analysis of only three lines (He II 304 Å, Fe XV 284 Å, Fe XVI 335 Å) already indicates that the relative prominence of spectral lines may depend upon the age of the center of activity which is responsible for the increased radiation. As an example, the maximum emission in the Fe XV (Figure 6) apparently occurs later in time than the maximum for the 2800 Mc radio flux or for the plage areas observed during March, April, and May. In addition to such a slowly changing effect, one may note that localized perturbations appear (7-9 March and 16-17 April) for which the relative increases are considerably different for the helium and the iron lines. It appears that in these instances we are observing phenomena localized at particular levels in the solar atmosphere.

CONCLUSIONS

Observations of the solar spectrum between 170 and 340 Å have been made over a time interval corresponding to approximately three solar rotations. The observations have shown:

Table 1
Increases in Solar EUV Spectrophotometer Counting Rates, 9 March 1962 to 23 March 1962.

Spectral Range (Å)	Average Counting Rate Increase (Percent)
171 - 228	55
229 - 300	80
229 - 305	52
305 - 400	50 (estimated)

1. That the He II (304 Å) emission is enhanced by a factor of about 33 percent during a period when the Zurich Provisional Relative Sunspot Number increased from zero to a maximum of 94 and the 2800 Mc flux varied from approximately 76×10^{-22} to 125×10^{-22} w/m²-H_z.

2. The Fe XV (284 Å) and Fe XVI (335 Å) coronal lines were enhanced during the same period by a factor of approximately four.

3. The enhancement of He II (304 Å) and Fe XV (284 Å) and Fe XVI (335 Å) due to plage activity was larger than enhancements due to flares that occurred during the three-month interval of the observations.

4. The variations in intensity of the He II (304 Å), Fe XV (284 Å) and Fe XVI (335 Å) represent the extremes observed. If sixty of the reliably observed lines between 171 and 342 Å are averaged, the enhancement is between 50 and 80 percent for the time interval 9 to 23 March.

5. Although there appears to be a gross correlation between solar activity indices (such as 2800 Mc flux) and the He II, Fe XV and Fe XVI fluxes, there are indications that the relative prominence of the spectral lines may depend upon the age of the center of activity.

REFERENCES

1. Hall, L. A., Damon, K. R., and Hinteregger, H. E., "Solar Extreme Ultraviolet Photon Flux Measurements in the Upper Atmosphere of August 1961," *Space Research III*, ed. by W. Priester. Amsterdam: North-Holland Publishing Co., 1963, pp 745-759.
2. Neupert, W. M., and Behring, W. E., "Solar Observations with a Soft X-Ray Spectrometer," *J. Quan. Spectr. Radiat. Trans.* 2:527-532, October-December 1962.
3. Zirin, H., Hall, L. A., and Hinteregger, H. E., "Analyses of the Solar Emission Spectrum from 1300 to 250 Å as Observed in August 1961," *Space Research III* ed. by W. Priester. Amsterdam: North-Holland Publishing Co., 1963, pp 760-771.
4. Ivanov-Kholodnyi, G. S., and Nikol'skii, G. M., "A Prediction of Solar Line Emission in the Extreme Ultraviolet" (In Russian), *Astron. Zh. USSR*, 38(5):828-843, 1961.
5. Tousey, R., "The Extreme Ultraviolet Spectrum of the Sun," *Space Sci. Rev.* 2(1):3-69, July 1963.

EMISSION OF EXTREME ULTRAVIOLET RADIATION FROM SOLAR CENTERS OF ACTIVITY

by

Werner M. Neupert

Goddard Space Flight Center

SUMMARY

Line emissions at 284 Å, 304 Å, and 335 Å in the solar extreme ultraviolet spectrum observed by OSO-1 have been compared with 2800 Mc emission and other indicators of solar activity. Increases in these ultraviolet fluxes can be localized to active regions on the solar disk. Changes in the intensities of the lines are discussed in terms of changes in electron temperature and electron density of the active regions. Certain assumptions made in the calculation of a coronal electron temperature from the relative populations in two stages of ionization of an element are examined, with the conclusion that this calculation may not be valid for the particular case of the solar corona, yielding a fictitiously low value if there is an outward expansion of ions from the base of the corona into a region of higher electron temperature. A non-equilibrium formulation for the distribution of ions is presented which may better describe the actual ion distribution in the corona. An approximate calculation shows that an average radial velocity, outward, and small compared with the average thermal velocity of the ions, is sufficient to explain the observed increase in height of the maxima of emission of the Fe ion sequence with increasing stages of ionization in the undisturbed corona.

INTRODUCTION

A grazing incidence spectrometer, operating as a pointed experiment on OSO-1 (1962 ζ1), has provided the first observations of variations of solar extreme ultraviolet (EUV) fluxes due to the presence of solar centers of activity on the sun's surface. In another paper presented at this conference,* these variations have been compared with fluctuations observed in other ranges of the solar electromagnetic spectrum; in this paper, the variations in EUV fluxes will be discussed in terms of changes in coronal electron densities and coronal temperatures that may be derived from them. Since the spectrometer has no inherent spatial resolution, this discussion will center around a comparison of EUV fluxes from the entire solar disk, when no disturbed regions are present, with fluxes observed when a well defined center of activity is present on the disk. The discussion is further restricted to three of the more reliably identified lines in the spectral range of the instrument: 284 Å (Fe XV), 304 Å (He II), and 335 Å (Fe XVI).

*"The Solar Spectrum from 50 Å to 400 Å," pp 53-62.

VARIATIONS IN SELECTED EUV EMISSION LINES

A summary of the non-flare variations observed in the above mentioned lines is given in Figures 1 and 2, in which each datum point represents the average of one orbit's observations (six to eight spectral scans). The error bars indicate one standard deviation in the data. The relationship which these observed counting rates have to several ground-based measurements of solar activity is also presented. In Figure 1, the He II Lyman-alpha radiation is compared with daily values of the solar flux at 2800 Mc (National Research Council, Ottawa, Canada) and with the Zurich Provisional Relative Sunspot Number (ZPRSN). Also shown is an estimate of the calcium plage intensity, computed for each day by summing over the observed (foreshortened) areas of all plages, each area being weighted by the estimated intensity of the plage, on a scale from 1 to 5.

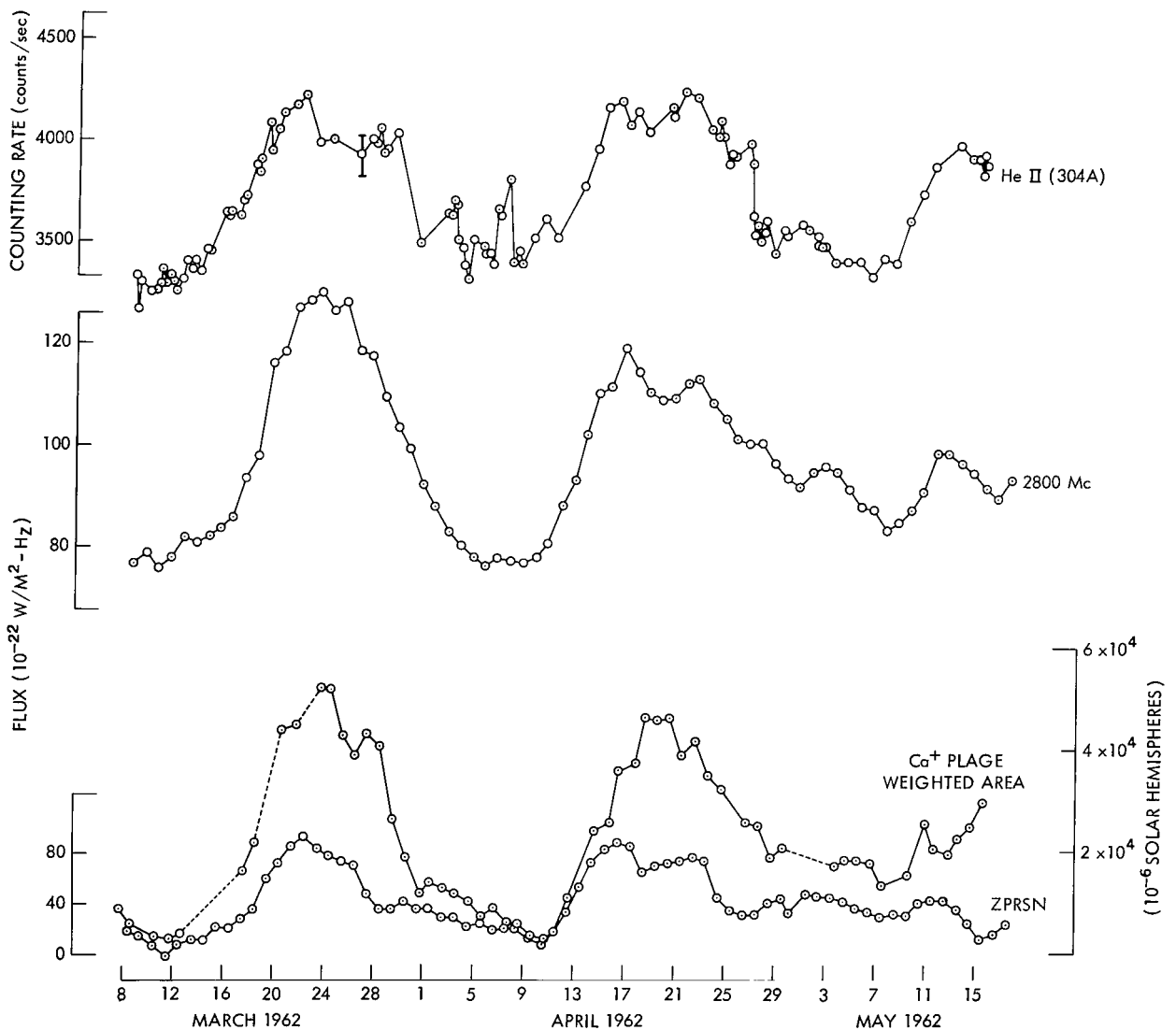


Figure 1—Comparison of the He II (304 A) line with measurements made at radio and optical wavelengths.

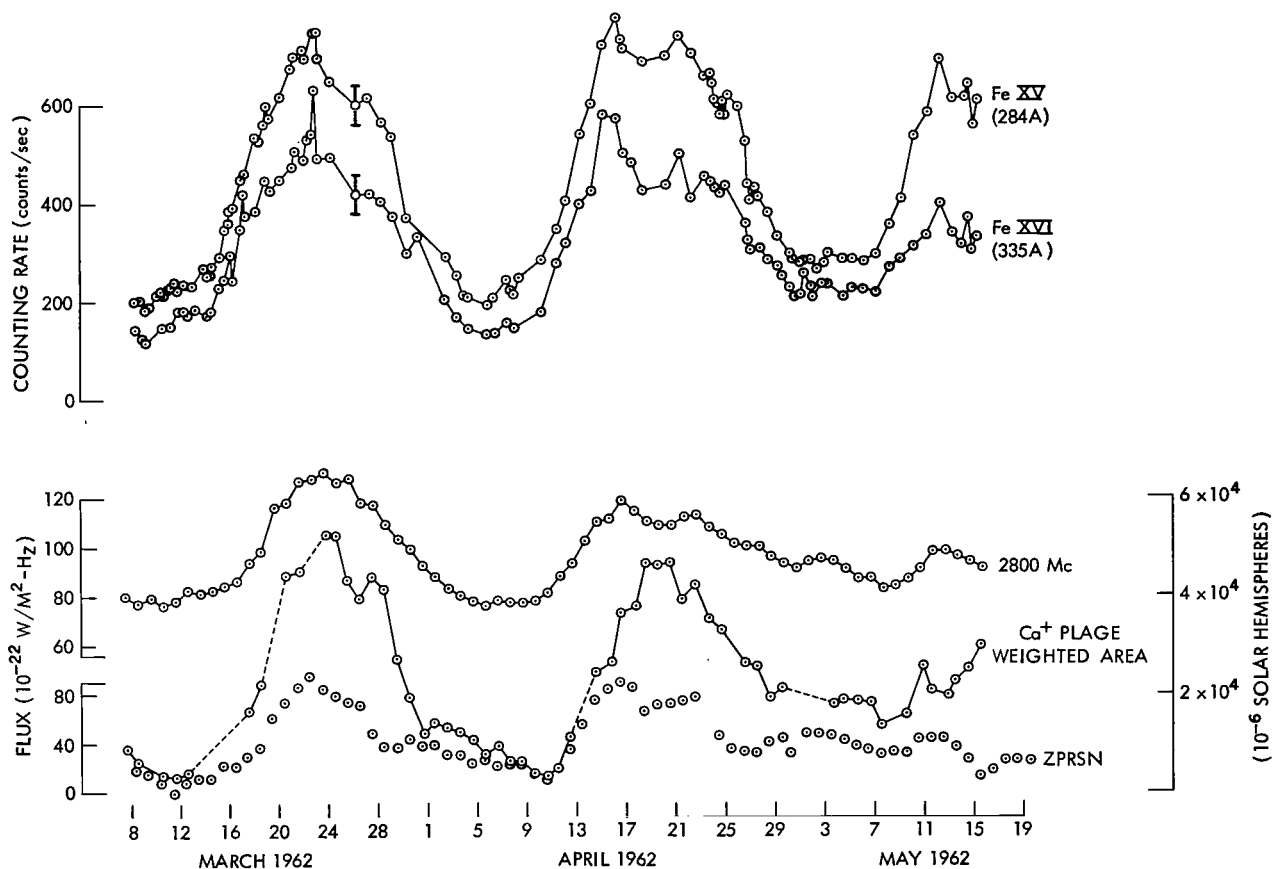


Figure 2—Comparison of Fe XV (284 A) and Fe XVI (335 A) lines with measurements made at radio and optical wavelengths.

Areas were taken in millionths of the solar hemisphere. Values for this computation were supplied by the McMath-Hulbert Observatory.

A similar presentation is made in Figure 2 for observations of the coronal lines of Fe XV and Fe XVI. Two methods were applied for estimating the instrument sensitivity at 284 A and 335 A. In the first of these, solar fluxes observed at those wavelengths by Hall, Damon, and Hinteregger (Reference 1), whose instrument had been calibrated, were compared to counting rates obtained by the GSFC instrument on days of comparable solar activity. The 2800 Mc daily flux was used as an index of this activity. In the second, the sensitivity was computed from estimated values of the grating reflectivity and detector efficiency. Sensitivities of 4.2×10^5 photons/cm²-sec-count at 284 A and 8×10^5 photons/cm²-sec-count at 335 A, representing averages of the values given by the two methods, were adopted and satisfied the need for a relative calibration at the two wavelengths. Their use as absolute values of the sensitivity is not recommended because of the limited validity of the calibration procedure.

DISCUSSION OF THE DATA

Observation of the Quiet Corona

The use of OSO-1 as a long-term stable platform has permitted the acquisition of a solar EUV spectrum which can tentatively be associated with a corona not disturbed by visible centers of activity. This situation presented itself for a short period of time on 11 March, when a ZPRSN of zero was reported. The American Relative Sunspot Number was reported as zero on both 10 March and 11 March. In addition, no large active regions had been associated with the face of the sun turned toward the earth on 11 March during the preceding six months. A careful analysis of the more intense emission lines, made for the period from 7 March to 5 April, demonstrates that the lowest counting rates of the period were indeed observed when the sunspot number was near zero and the calcium plage area on the sun was also at a minimum. However, it is also clear from an examination of Figures 1 and 2 that no close correlation can be assumed to exist between the EUV fluxes and any of the ground-based observations. As Figure 2 shows, counting rates from the iron lines were lower on 1 May, when the Sunspot Number was 49, than on 15 May, when it was at 13. Likewise, although the agreement between the radio data and EUV coronal fluxes at times is striking, (as for instance in the interval from 13 April to 25 April, a period of considerable solar activity), this similarity is not consistent, as the data taken from 29 April to 15 May shows: A small maximum observed at 2800 Mc on 1 May to 5 May does not appear at 284 Å whereas on the succeeding days, 9 May to 15 May, a larger peak is observed at 284 Å than at radio wavelengths. The anomaly can be eliminated, at least in this particular instance, by observing that the flux at each wavelength depends on the age of the center of activity being observed. The region under observation on 1 May to 5 May is a center of activity approximately 1 solar rotation old whereas the plage areas observed on 9 May to 15 May are remnants of active regions 4-5 rotations old. The trend in the data is consistent with a model for a center of activity (CA) described by De Jager (Reference 2), in which the center is initially localized in the lower altitudes of the solar atmosphere and gradually expands into the quiet corona. After the spot phase of the CA has passed, the region remains as a magnetic bipolar region which may have quiescent filaments and perhaps coronal rays associated with it. The continued enhancement of the Fe XV and Fe XVI lines after all sunspots have vanished in the region may be an indication of remaining coronal rays. In any event, these observations suggest that it is necessary to have knowledge of the recent past history of solar activity as well as current data in order to make a correlation with the EUV radiation.

Having established an emission spectrum corresponding as nearly as the data permit to an undisturbed corona as observed approximately four years after sunspot maximum, we may compute an electron temperature for the quiet corona which is implied by the observed spectrum. The reason for choosing an undisturbed spectrum for this calculation is that we are forced to make an assumption of the spherical symmetry of the corona since the spectrometer has, inherently, no spatial resolution and this assumption is best satisfied when large scale structures, as evidenced by EUV enhancements, are absent. An electron temperature may be derived (Reference 3) from the observed ratio of intensities of two spectral lines originating from two different ionic species of the same element. Such a calculation has validity only if both radiations originate in the same region

of the corona at some well-defined electron temperature, and only if the ionization-recombination equilibrium assumed by the theory is actually present. These assumptions will be examined in the following sections.

The ionization formula used to relate the relative populations in adjacent states of ionization was that of Elwert (References 4 and 5). Excitation cross-sections were computed from the expression derived by Woolley and Allen on the basis of the classical Thompson atom. The oscillator strengths were taken from Varsavsky (Reference 6). It is found that an electron temperature of 1.75 million degrees in that part of the corona assumed to be the source of both the Fe XV and Fe XVI radiations best fits the observed data. The estimated possible error in this value arising from uncertainty in the relative sensitivity of the spectrometer at the two wavelengths is $100,000^{\circ}\text{K}$. This result contrasts sharply with the value of $800,000^{\circ}\text{K}$ usually obtained from observation of the forbidden lines of Fe X and Fe XIV. Since both results are ultimately based on the same theory of ionization equilibrium, we are forced either to question the validity of the ionization equilibrium assumed or to postulate that a range of electron temperature exists in the corona. Indeed the very observation of six stages of ionization of iron, from Fe X through Fe XV, excepting Fe XII in the visible, coupled with the Fe XVI resonance transitions in the ultraviolet, leads to the same conclusion.

EUV Radiation from Solar Centers of Activity

A discussion of the sources of radiation from Fe XV and Fe XVI may be extended to include centers of activity and plages since it appears from the data that emission from these two ions is intimately associated with these disturbances. In this section we will consider whether or not a unique change in electron temperature or density or both can be obtained for the corona above plages from the EUV data. A tentative analysis has been made for changes observed in the 284 Å and 335 Å counting rates between 11 March (ZPRSN equal to zero) and 25 March (ZPRSN equal to 74). Although the latter date does not represent the period of greatest deviation of the spectrum from quiet sun conditions, it was chosen because of the relatively well-defined configuration of three plage areas near the central meridian at that time. During this period the Fe XVI radiation increased by a factor of 3.85, the Fe XV radiation by 3.37, and the Fe XIV radiation (as estimated from optical observations of λ 5303) by 2.50. It is obvious that the center of activity represents a more complex change than simply an increase in density in a volume having a uniform and non-changing electron temperature. On the other hand, it is also impossible to explain the changes in emission as exclusively due to an increase in electron temperature in a homogeneous volume of the corona; that is, no one unique increase in electron temperature of the center of activity above that of the quiet corona can explain the observed spectral variations. From the nearly constant Fe XVI/Fe XV ratio there is only a small temperature increase, $100,000^{\circ}\text{K}$, whereas the increase implied by the Fe XV/Fe XIV ratio (using λ 5303 data) is more than two and one-half times as large. The inability to obtain consistent results under the assumption of an isothermal center of activity again suggests that not all spectral lines are emitted uniformly from the corona but that those regions (or region) emitting Fe XV and Fe XVI radiation from the quiet corona become relatively more predominant over centers of activity and plages.

EFFECT OF A CORONAL EXPANSION ON THE CALCULATION OF AN ELECTRON TEMPERATURE

Discussion of the Ionization Equation

The inconsistencies discussed in the foregoing sections, as well as the long standing discrepancy between the electron temperature of the quiet corona obtained from forbidden emission line intensity ratios and other values computed from the electron density gradient has led to an analysis of the ionization theory upon which the former value is based. It appears that a combination of two physical conditions may exist in the corona which may produce this discrepancy:

1. An average time between ionizations or recombinations which is large compared with the time for equipartition of energy between the ions and the coronal electrons;
2. A mass motion of ions through a region having a high electron temperature gradient in a period of time equal to or less than the above mentioned time between ionizations.

First consider the existence of each of these effects in the lower corona and their influence on a theory with ionization equilibrium assumed. An estimate of the time between ionizations can be obtained using values of the ionization cross-section for iron ions given and discussed by Firor and Zirin (Reference 7). These cross-sections are found to increase only slightly with temperature (from 0.21×10^{-12} cm³/sec at 1.0×10^6 °K to 6.4×10^{-12} cm³/sec at 2.6×10^6 °K for Fe XII). The change with stage of ionization at a given temperature is still less sensitive, decreasing, for example, from 5.3×10^{-12} cm³/sec for Fe X to 2.0×10^{-12} cm³/sec for Fe XIV at 2.0×10^6 °K. A measure of the time between successive ionizations is then given by

$$\tau_{ion} = \frac{N_i}{N_i N_e S(T)} = \frac{1}{N_e S(T)}$$

where N_i is the ion density, N_e is the electron density and $S(T)$ is the ionization rate in cm³/sec. Taking a value for N_e of 3.5×10^8 /cm³ at a height of $1.02 R_\odot$ (where R_\odot is the solar radius) and a $S(T)$ of 3.0×10^{-12} cm³/sec we find that a time of the order of 1000 sec is required to ionize (without recombinations) an assemblage of ions from stage i to stage $i + 1$. On the other hand, the time required to establish equipartition of energy between electrons and heavy ions in the coronal plasma is considerably shorter. This characteristic time can be computed from an equation given by Spitzer (Reference 8) and is of the order of 20 sec for Fe XIII-electron equilibrium at an electron density of 3.5×10^8 /cm³ and temperature of 2.0×10^6 °K. The time for equipartition is again inversely proportional to the electron density, which leads to the relation

$$\tau_{ion}/\tau_{equi} \approx \text{constant} \gg 1$$

for a given ion anywhere in the solar corona.

In considering the second condition stated above we must restrict ourselves to regions of low magnetic field, thereby permitting an expansion of the corona which results in the corpuscular

stream deduced by Biermann (Reference 9) from his work on comet tails and was more recently discussed by Parker (Reference 10). Using the continuity equation we can compute the average solar wind velocity at any height in the corona once its velocity and particle density at another height have been defined. Using as initial parameters (Reference 11) for $r = 1.43 R_{\odot}$, a proton density of $1.8 \times 10^7/\text{cm}^3$ and a solar wind velocity of 66 km/sec, we find at $1.02 R_{\odot}$, where the density is approximately $3.5 \times 10^8/\text{cm}^3$, a velocity of about 7 km/sec. From these figures we may conclude that an ion may travel radially outward at a distance of 10^3 to 10^4 km in the lower corona before undergoing further ionization.

The result of fulfilling both of the above conditions is that an ion, in traveling along a positive electron temperature gradient or in crossing a steep gradient representing a large change in electron temperature, very quickly attains an average thermal velocity characteristic of the higher temperature (Condition 1) but carries with it, for a much longer time and radial distance, a history of any previous ionization equilibrium (Condition 2). Under such circumstances no theory which postulates equilibrium between ionization and recombinations can furnish a valid value for the electron temperature of the region even if the predominant ionization mechanism is electron impact, and recombination is by radiative capture. A kinetic temperature derived from line broadening may still be valid, however. Because of the large increase in temperature over a distance of 10,000 km or less in the lower solar corona it appears that the situation described herein may well occur throughout the lower corona where most of the coronal radiation is observed.

At any height in the corona, we then must replace the equilibrium equation

$$N_i N_e S_i^{i+1}(T) = N_{i+1} N_e Q_{i+1}^i(T) ,$$

where $Q(T)$ is the recombination rate in cm^3/sec^1 , with the more general equation

$$\nabla \cdot \mathbf{F}_i \geq 0$$

where \mathbf{F}_i is the flux of ions in stage i of each element.

For an optically thin corona of low density in which photoionizations and three-body recombinations are assumed to be negligible we obtain

$$\nabla \cdot \mathbf{F}_i = N_{i-1} N_e S_{i-1}^i(T) - N_i N_e (Q_i^{i-1}(T) + S_i^{i+1}(T)) + N_{i+1} N_e Q_{i+1}^i(T) ,$$

for each stage of ionization i of each element present, together with

$$N(r) = \sum_i N_i(r) ,$$

where N is the number density in each stage of ionization. The summation is made over all stages of ionization of the particular element being considered.

For a spherically symmetric corona expanding with velocity of magnitude $v(r)$ we have, for the total flux of a particular ion crossing a shell of radius r ,

$$F_i = 4\pi r^2 N_i(r) v(r) .$$

By requiring a steady state outward flow (i. e., all ions moving outward with the same average velocity), we obtain

$$\begin{aligned} F_0 &= \sum_i F_i \\ &\approx 4\pi r^2 N_e(r) v(r) = \text{constant} \end{aligned}$$

In this case the summation includes all elements present.

Using the notation P_i for the relative population in each stage of ionization,

$$P_i = \frac{N_i(r)}{N(r)} ,$$

we obtain

$$\frac{d}{dr} P_i = \frac{N_e^2}{F_0} \left[P_{i-1} S_{i-1}^i(T) - P_i (Q_i^{i-1}(T) + S_i^{i+1}(T)) + P_{i+1} Q_{i+1}^i(T) \right]$$

for each element and each stage of ionization.

It is possible to discuss the general behavior of the system by considering the expansion of an assemblage of ions from a region of low electron temperature of 10^5 °K to a hotter region of 10^6 °K, the change in electron temperature taking place over a distance of only a few thousand kilometers. Examination of the equation for the lowest stage of ionization present at 10^5 °K indicates that the relative population will decrease, in the absence of recombinations, by a factor of $1/e$ in a distance of

$$\frac{F_0}{\frac{4\pi r^2}{N_e^2 S(T)}}$$

which is of the order of 10^4 km. Including recombinations will increase this distance. Higher stages of ionization will become more populated with increasing height above the photosphere,

reaching an ionization equilibrium characteristic of the higher temperature only in a distance of a few tens of thousands of kilometers. It is precisely in this height range that most of the coronal radiation is observed.

Comparison with Observations

A small amount of observational evidence is available which appears to support the scale computed. Beginning with the lower stages of ionization of iron observed in the corona, it has been found for the undisturbed corona that:

1. The maximum in Fe XI emission occurs below 10,000 km above the photosphere (25 February 1952 eclipse; Reference 12).
2. The maximum in Fe XIV occurs (statistically) at about 18,000 km (Reference 13).
3. The intensity of the Fe XV line at 7059 Å decreases much more slowly with distance from the limb than do the lines of Fe X (6374 Å) and Fe XI (7891 Å) (15 February 1961 eclipse; Reference 14). Based on the observation by OSO-1 that the intensity of emission from Fe XVI requires emission from 0.1 to 0.5 of the solar corona we might hypothesize, in accordance with the model being presented here, that the maximum in emission of Fe XVI occurs at about 40,000 km. Because of the rapidly decreasing electron density with height in the lower corona the maximum in intensity of an ion may be very broad and need not be coincident with the maximum in relative population.

It is also of interest to reverse the problem by using the experimental data to estimate the radial velocity that would be required to achieve the observed separations of maximum emission assuming again that excitations are produced primarily by electron collisions. Using an average time between ionizations of 1000 sec for stages Fe XI through Fe XIV and 2000 sec for Fe XV and Fe XVI we obtain:

For the radial velocity of Fe XI through Fe XIV,

$$\bar{v} \approx 10,000/3000 = 3.3 \text{ km/sec ;}$$

For the radial velocity of Fe XV and Fe XVI,

$$\bar{v} \approx 20,000/4000 = 5 \text{ km/sec}$$

These values are comparable to the solar wind velocity of the lower corona computed on page 7. By comparison, the average thermal velocity for Fe ions at 2.0×10^6 °K is 16 km/sec. Since only limb observations of the corona are possible at visible wavelengths, little or no shift in the emission lines, due to their outward velocity, should be observable.

SUMMARY

Intensity variations of three spectral lines observed in the solar EUV spectrum have been presented together with a discussion of the slowly varying component of solar activity which

accompanied these changes. The Fe XV and Fe XVI lines are found to be prominent in the solar spectrum even in the absence of solar activity—a fact not expected on the basis of observations of forbidden lines of iron in the visible spectrum. It is found that a general correlation with solar activity exists, with the suggestion that an increase in these coronal radiations occurs subsequent to appearance of a center of activity as observed at 2800 Mc and may linger in the presence of diminishing Ca+ plages after the cessation of solar activity in an active region. The enhancement at 284 Å and 335 Å is nearly the same which implies little or no temperature increase in active regions having no yellow line (Ca XV) emission. These observations are consistent with a model for active regions which postulates both an increase in electron density and an increase in the vertical range over which radiation from Fe XV and Fe XVI is emitted. The discrepancy observed between the electron temperature obtained from ion ratios and that inferred from electron density profiles for the quiet corona has led to the suggestion that the former method may yield a fictitiously low value if there is a streaming outward of ions from the base of the corona. An approximate calculation shows that a radial velocity outward (small compared with the average thermal velocity of the ions) is sufficient to explain the observed increase in the maximum height of emission of the Fe ion sequence with increasing stages of ionization.

REFERENCES

1. Hall, L. A., Damon, K. R., and Hinteregger, H. E., "Solar Extreme Ultraviolet Proton Flux Measurements in the Upper Atmosphere of August 1961," in *Space Research III*, ed. by W. Priester, Amsterdam; North-Holland Publishing Co., 1963, pp 745-759.
2. de Jager, C., "The Development of a Solar Center of Activity," in "Vistas in Astronomy," v. 4 (A. Beer, ed.), 143-183, New York: Pergamon Press, 1961.
3. Woolley, R. v. d. R., and Allen, C. W., "The Coronal Emission Spectrum," *Roy. Astron. Soc. Mon. Not.* 108(3):292-305, 1948.
4. Elwert, G., "The Continuous Emission Spectrum of the Solar Corona in the Far U. V. and the Adjacent X-Radiation," (In German), *Z. Naturforsch.* 7a:202-204, February 1952.
5. Elwert, G., "Ionization and Recombination Processes in a Plasma, and the Ionization Formula for the Solar Corona," (In German), *Z. Naturforsch.* 7a:432-439, June 1952.
6. Varsavsky, C. M., "Some Atomic Parameters for Ultraviolet Lines," *Astrophys. J. Suppl. Ser.* 6(53):75-108, March 1961.
7. Firor, J., and Zirin, H., "Observations of Five Ionization Stages of Iron in the Solar Corona," *Astrophys. J.* 135(1):122-137, January 1962.
8. Spitzer, L., Jr., "Physics of Fully Ionized Gases," New York: Interscience Publishers, 1956.
9. Biermann, L., "Remarks on the Law of Rotation in Terrestrial and Stellar Zones of Instability," *Z. Astrophys.* 28(3):304-309, 1951.

10. Parker, E. N., "The Hydrodynamic Theory of Solar Corpuscular Radiation and Stellar Winds," *Astrophys. J.* 132(3):821-826, November 1960.
11. Parker, E. N., "The Solar Wind," in "Space Astrophysics," (W. Liller, ed.), 157-170, New York: McGraw-Hill Book Company, 1961.
12. Athay, R. G., and Roberts, W. O., "Coronal Line Intensities at the Khartoum Eclipse," *Astrophys. J.* 121(1):231-240, January 1955.
13. Petri, W., Forschungsber. Obs. Wendelstein No. 2, 1952.
14. Wlerick, G., and Fehrenbach, C., "Premiers Résultats Concernant les Spectres Infrarouges de la Couronne Obtenus pendant l'eclipse du 15 Février 1961," *Proc. I.A.U. Symposium* 16, 1963.

PRELIMINARY SOLAR FLARE OBSERVATIONS WITH A SOFT X-RAY SPECTROMETER ON THE ORBITING SOLAR OBSERVATORY

by

W. E. Behring, W. M. Neupert, and J. C. Lindsay

Goddard Space Flight Center

SUMMARY

A spectrometer carried by Orbiting Solar Observatory I and used for observing the solar spectrum from 10 to 400 Å is described. The instrument utilizes a concave grating mounted in grazing incidence, and an open window photomultiplier. Resolution of approximately 1 Å is obtained throughout the wavelength region covered. Solar spectra obtained with this instrument during a rocket flight are shown, and tentative identification of the origins of observed spectral lines is listed. Preliminary satellite results obtained during a solar flare are discussed.

INTRODUCTION

The prime experiment flown on the first Orbiting Solar Observatory (1962 ζ1) was a soft x-ray spectrometer designed specifically to measure the solar spectrum from 10 to 400 Å. As a result of the successful launch of the satellite into a near circular earth orbit (550 km perigee and 600 km apogee) and the subsequent successful operation of the experiment, the first long term measurements of the soft x-ray solar spectrum have been obtained. The purpose of this paper is to describe briefly the instrument, to illustrate its performance by data obtained from a rocket launch and to present some very preliminary satellite data obtained before and during the solar flare of 13 March 1962.

THE SPECTROMETER

The angular aperture of the spectrometer is approximately 1.2° by 2.2° . Hence, with moderately accurate pointing (within plus or minus a few minutes of the center of the solar disc), the spectrometer responds to the total light intensity emitted by the sun. The orientation of the spectrometer is such that the sunlight falls perpendicularly on the front face of the instrument (Figure 1), passes through the entrance slit and strikes a concave grating mounted in grazing incidence (the angle of incidence being 88°). The original grating was lightly ruled in a special glass by the Nobel Institute in Stockholm at 576 lines/mm on a one-meter radius of curvature blank. No reflecting

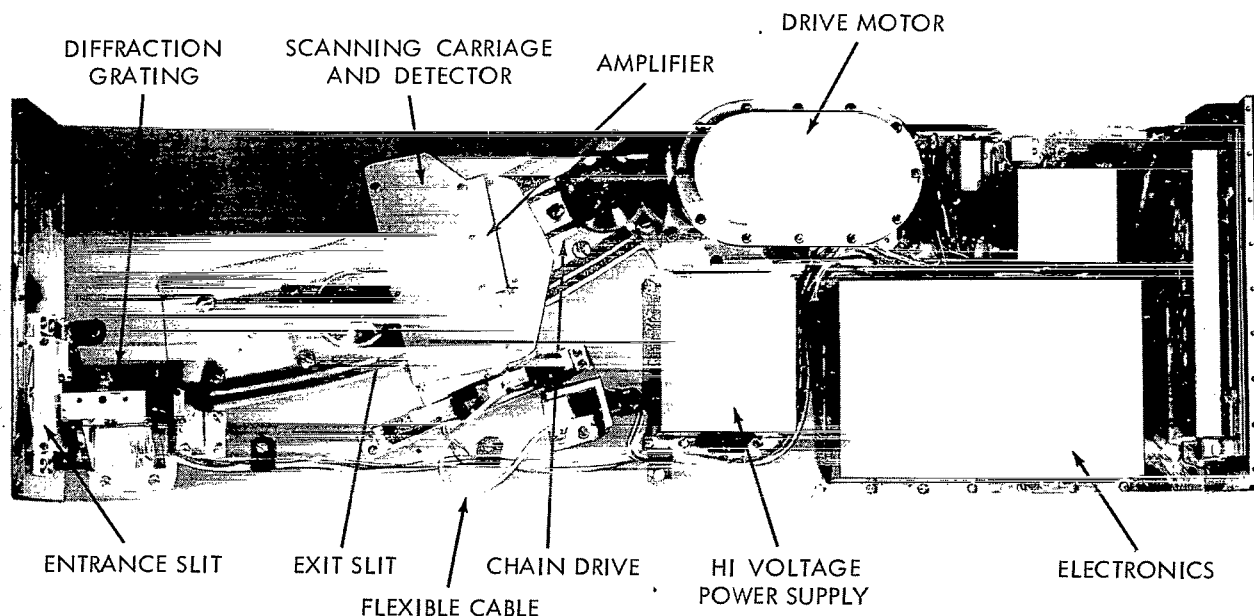


Figure 1—The OSO-1 Spectrometer.

coatings of any kind were used on this grating. The diffracted rays continue to the exit slit in front of the detector. The detector is mounted on a carriage, which moves on a circular rail so that the exit slit follows along the Rowland circle where the spectrum is in focus. The plane of the exit slit stays approximately perpendicular to the diffracted ray at all positions along the rail, thereby keeping the spectral passband nearly constant for all angles of diffraction. The 50μ entrance and exit slits provide a spectral passband of 1.7 \AA and permit resolution of lines 0.85 \AA apart.

The detector used was an open window multiplier phototube developed by the Bendix Corporation specifically for use in this spectrometer and designated the M-306. Photoelectrons from the tungsten cathode move along cycloidal paths in crossed electric and magnetic fields between two glass strips, each coated with a semi-conducting, secondary-emitting oxide layer. One of the glass strips serves as a continuous dynode. Each photoelectron is multiplied into a pulse of approximately 10^6 electrons at the anode. These electrical pulses are amplified and, after coding to compress bandwidth, are recorded on a tape recorder for later transmission to a ground station.

The spectrometer uses about 1.3w supplied by the satellite at 18v dc. About one watt of this goes to the oscillator powering the three-phase synchronous motor which requires about 300 mw at 137 cps to yield 100 mw of mechanical output power. The remainder of the power is used in the multiplier and pulse handling circuitry.

All of the materials exposed inside the spectrometer were tested at a pressure of about 10^{-6} mm Hg to eliminate any material which had a high vapor pressure. Because the electronic circuits were potted in a compound having a high vapor pressure, they were enclosed in sealed boxes which were vented to the outside through holes in the spectrometer base plate. During assembly all the parts exposed to the interior were carefully cleaned to be free of oil, grease, and other contaminants.

The temperature of the instrument is controlled by the radiation balance. Most of the outer case was polished. The central section was painted black in order to tie the temperature closely to that of the satellite.

Alignment of the spectrometer using only visible light was accomplished by means of a fixture with a radius rod pivoted at the center of the Rowland circle. The procedure was developed on the basis of the method described by Rathenau and Peerlkamp (Reference 1). Alignment tests were performed using a source of carbon K radiation. A separate Bendix photomultiplier was used to provide a monitor on the stability of this source. The response to scattered hydrogen Lyman-alpha radiation was checked using a closed hydrogen discharge lamp. The grating used was selected by means of comparative tests performed on several gratings by Professor Tombouliau at Cornell University.

THE ROCKET FLIGHT

The solar spectrum obtained with a similar instrument during an Aerobee rocket flight using a Ball Brothers rocket pointing control is shown in Figure 2. In this spectrum the wavelength regions of 120 to 170 Å and 220 to 240 Å represent the average of data taken in three different scans in an attempt to improve the reliability of faint lines and to provide continuity in the region originally containing wavelength marker pulses. In the region below 100 Å evidence of spectral lines is inconclusive. Comparison of the observed counting rates with laboratory scattered light measurements indicates that for the rocket flight the signal attributable to the first order spectrum becomes lost in the scattered light below about 60 Å.

An attempt has been made to identify the resonance lines of highly ionized atoms of the heavier elements. Lines produced by several stages of ionization of C, N, O, and also by Mg, Si, Ne and Fe

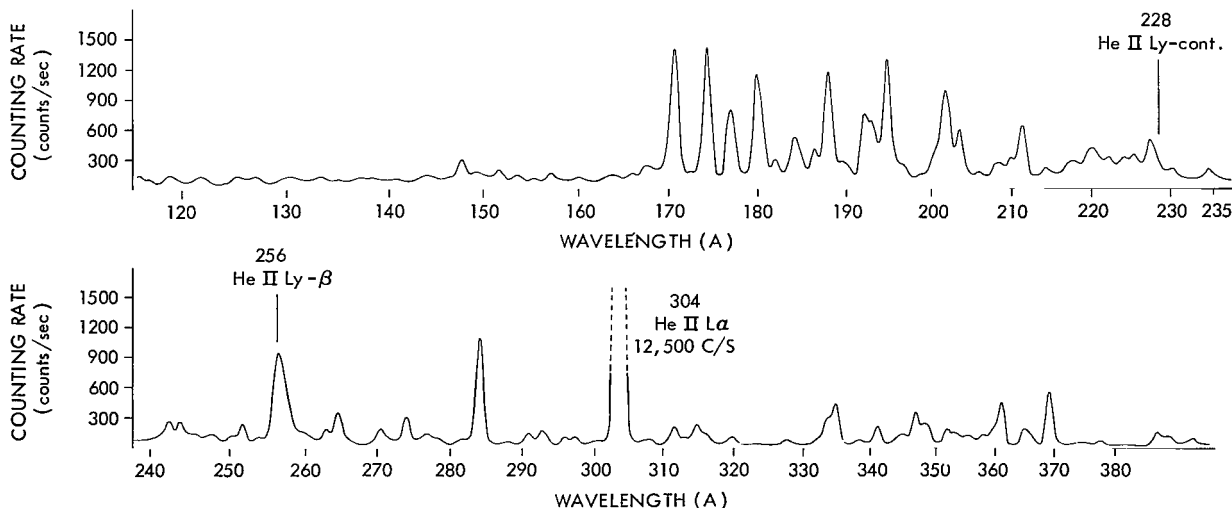


Figure 2—The solar spectrum, 30 September 1961. Time 14:33 (GMT); altitude 201-216 km.

Table 1
Wavelengths of Some Strong Lines
and Tentative Identification of
their Origins.

Ion Identified	Wavelength (A)
Fe XIV, Fe XII	370
Fe X	366
	365
Fe XVI	361
Fe XII	360
Ni XV, Fe X	347
Fe XIV	345
	341
Fe XVI	335
Ni XV	333
	320
Ni XV	316
	315
	312
He II	304
	293
Fe XV	284
Cu XIX	274
	271
S X	264
A XIV	263
He II, Ni XVII	256
A XIV	250
He II	244
	243
He II	234
Ca XV	227
S IX	220
	211
	204
	202
	195
	193
	192
A XI	188
A XI	186
C1 IX	184
	182
C1 IX	180
	177
	174
	171

have already been found at longer wavelengths. The extension of isoelectronic sequences to heavier elements leads to resonance lines with wavelengths below 400 A. The wavelengths of some of the strong lines observed are shown in Table 1, along with tentative identifications of their origin. The tabulation of emissions compiled by Varsavsky (Reference 2) was used in this work.

Criteria for making assignments were: (1) Agreement with theoretically extrapolated values of the spacing and relative intensities of members of a multiplet, assuming, for the intensities, an optically thin corona; (2) Approximate agreement in wavelength with theory for lines not yet observed under laboratory conditions; and (3) Observation of more than one stage of ionization.

A preliminary analysis of the spectrum was made for ions known to exist in the solar atmosphere: Fe, Ni, and, with lesser abundances, Ca and A. Identification of iron multiplets on the basis of one observation is made difficult by the presence of strong second order lines as well as the superposition of the multiplets themselves. Only the Fe XV line has been calculated with accuracy by Edlen (Reference 3), and has been identified with a strong line at 284 A. The resonance lines of Ca XII and Ca XIII (two ions observed in the visible coronal spectrum) cannot be associated with any of the emissions in the far ultraviolet spectrum. Neither is a correlation observed, although it is expected, for A X.

All of the foregoing assignments must be regarded as tentative and are presented as "work in progress." It is expected that application of satellite observations and further theoretical analyses can be combined to achieve more reliable identifications.

Long term observations from the satellite will permit additional conditions to be applied: (1) Constancy in time of the ratio of intensities of members of a multiplet, assuming no change in the opacity of the corona with time; (2) Regularity in the variations

of intensity over the observed stages of ionizations; and (3) For each stage of ionization, agreement in variations of intensity with corresponding variations in visual coronal lines.

PRELIMINARY SATELLITE OBSERVATIONS

The Orbiting Solar Observatory was launched at 1606 UT, 7 March 1962. The sun was unusually quiet until 13 March when a small flare occurred. The H_α flare (Figure 3), shows sun in H_α at 15:43:22, was classified as a 2+ by Wendelstein, the onset being recorded under very poor observing conditions at 1448 UT with the duration observed as 73 minutes. The heliographic coordinates were recorded as E66, NO6. Climax first observed the flare in progress at 1502 UT, estimating the importance as 1+ and recorded the ending at 1615 UT. The heliographic coordinates were recorded as E63, NO3.

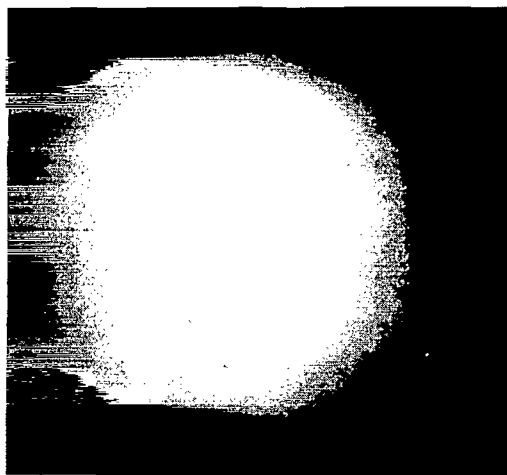


Figure 3—The H_α flare at 1543:22;
13 March 1962.

A typical short wave fadeout (SWF) was recorded at NERA at 1448 UT with importance 2 (Scale 1-3, similar to that for flares). HAO gives 1455-1634 UT for the duration and 3 for the importance. Type III radio bursts were recorded by HAO on 22-41 Mc from 1519-1550 UT. Major radio bursts occurred on 108 Mc from 1450-1510 UT and on 200 Mc from 1450-1505 UT. There was no evidence of energetic particle fluxes.

In the time available, it has been possible to reduce only partially the satellite data for the six orbits that surrounded the beginning of the visual flare. Three spectral lines were chosen for analysis: He II, Lyman alpha at 303.8 Å, 284 Å (tentatively identified as an Fe XV line). These data are shown in Figure 4, from which we observe:

1. Increased emission coinciding with or preceding visual observations or other indicators;
2. Possible continued enhancement after cessation of other indicators.

Using values for these two lines before the onset of the flare and during the flare, we find the maximum enhancements for the lines were as follows: 304 Å, 15%; 283 Å, 28%. Typical error flags are shown with the data. Practically all of the error is statistical, and is due to the relatively small number of photons counted. The changes in the observed line intensities are larger than the expected errors, and are believed to represent real changes associated with the flare.

As of 13 April OSO-1 had made approximately 550 orbits around the earth with the result that some 3500 spectra of the sun in the 10-400 Å region have been collected. During this time fourteen flares of varying importance occurred; the largest a Class 3 on March 22. We believe these data will:

1. Aid in identifying the spectral lines.

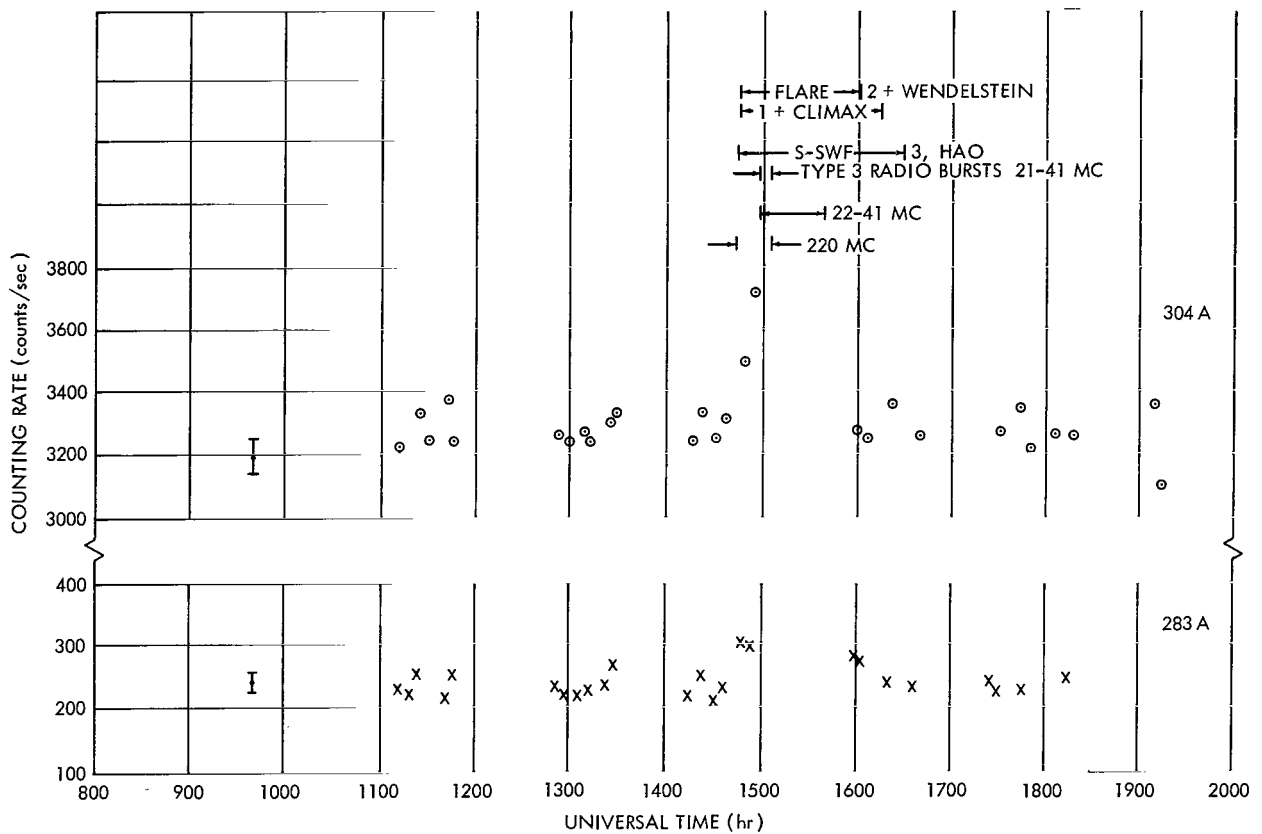


Figure 4—Relative solar flux at 304 and 283 A encompassing the 13 March 1962 flare.

2. Allow limits to be placed on the continua in this wavelength region, for a quiet sun as well as during solar activity.

3. Allow quiet sun line intensity measurements with some certainty. From our preliminary measurements, it can be seen that a rocketborne instrument would have encountered enhancement several hours after the visual flare was over.

4. Determine line intensity enhancement, if any, before and during, and following visual flare activity.

5. Determine enhancement, if any, associated with other solar activity, i. e., plage areas and spot groups.

6. Determine short time fluctuations in line intensities not associated with other easily observable phenomena.

Analysis and interpretation of these results should throw light on the energy transport in the corona and the relaxation time of the corona as well as form the basis for a more complete model of the chromosphere.

ACKNOWLEDGMENTS

So many people played an important part in the development of this spectrometer that it is not possible to mention all of them. However, the authors would like especially to thank Professor D. H. Tombouliau, Cornell University, who developed and carried out the tests of the gratings on the basis of which the flight gratings were selected. We are indebted also to Mr. Kennard Saffer and Mr. Paul Kraft, Naval Weapons Plant, Washington, D. C., for executing the design and supervising the construction of the spectrometer; Mr. W. A. Nichols, Goddard Space Flight Center, who carried out the modifications required for the rocket spectrometer and assisted in the development of the satellite spectrometer.

REFERENCES

1. Rathenau, G., and Peerlkamp, P. K., "Adjustment of a Concave Grating at Grazing Incidence," (In German), *Physica*, 2:125-143, February 1935.
2. Varsavsky, C. M., "Some Atomic Parameters for Ultraviolet Lines," *Astrophys. J. Suppl. Ser.* 6(53):75-108, March 1961.
3. Firor, J., and Zirin, H., "Observations of Five Ionization Stages of Iron in the Solar Corona," *Astrophys. J.* 135(1):122-137, January 1962.

SOLAR X-RAYS: SLOW VARIATIONS AND TRANSIENT EVENTS

by

William A. White
Goddard Space Flight Center

SUMMARY

Solar x-ray flux integrated over the interval 0.1-10 Å was measured from the OSO-1 satellite in early 1962 using a xenon-filled ion chamber with a thin beryllium window. A slowly-varying component of x-ray flux was observed which correlates well with the slowly-varying component of 2800 Mc solar radiation. The component of the x-ray flux can be accounted for by postulating localized sources having the same horizontal extent as Ca plages with thicknesses proportional to their diameter; and having an electron temperature of about $2.8(10)^6$ °K and an electron density of about $5(10)^9$ electrons/cm³. A further conclusion is that for these conditions the ratio of line emission to continuum emission is at least 10:1 and more probably 30:1.

In addition to a slowly varying component, transient events (x-ray flares) lasting from 10 minutes to a few hours were frequently observed. Correlations with H-α flares, with SID's, and with 2800 Mc transients have been investigated; the results show that as an indicator of local solar activity, the OSO-1 x-ray experiment was more sensitive by a large factor than indicators based on ionospheric effects or than indicators based on observations of solar flux in visible or radio wavelengths. X-ray flares were frequently observed to be associated in groups possessing a characteristic pattern; the implications are discussed.

INTRODUCTION

With the launching of the OSO-1 (1962 ζ1) on 7 March 1962, it became possible for the first time to point instruments at the sun accurately and continuously for entire daylight portions of a satellite orbit; for the 550-km orbit of OSO-1 these observing time intervals were the order of 1 hr, separated by darkness intervals of about 2/3 hr. The observing periods were long enough to disclose some interesting dynamic effects which would be difficult to study otherwise.

SENSOR CHARACTERISTICS

OSO-1 provided coverage of the solar x-ray radiation near a wavelength of 10 Å by means of an ion chamber whose characteristics are given in Table 1. The conversion efficiency as a function of wavelength is shown in Figure 1.

Table 1
Sensor Characteristics.

Characteristic	Value
Window Material	Beryllium
Window Thickness	0.005 inch
Total Window Area (Two chambers in parallel)	3.38 cm ²
Absorbing Gas	Xenon
Gas Pressure	780 mm
Ion Chamber Depth at Normal Incidence	2.19 cm
Ion Paris/erg	2.8(10) ¹⁰

The full scale sensitivity is, of course, dependent upon the shape of the input spectrum. It will be shown that for non-flare periods it is reasonable to assume a spectral shape consistent with a $2.8(10)^6$ °K plasma; for such a spectrum, wavelengths contributing to the output current lie in the interval 3-11 Å; the full-scale sensitivity at such times is $1.8(10)^{-3}$ erg/cm²-sec within this wavelength region. For comparison with earlier measurements (Reference 1) over bandwidths specified as 2-8 Å, the full-scale sensitivity over a band is $3.6(10)^{-4}$ ergs/cm²-sec.

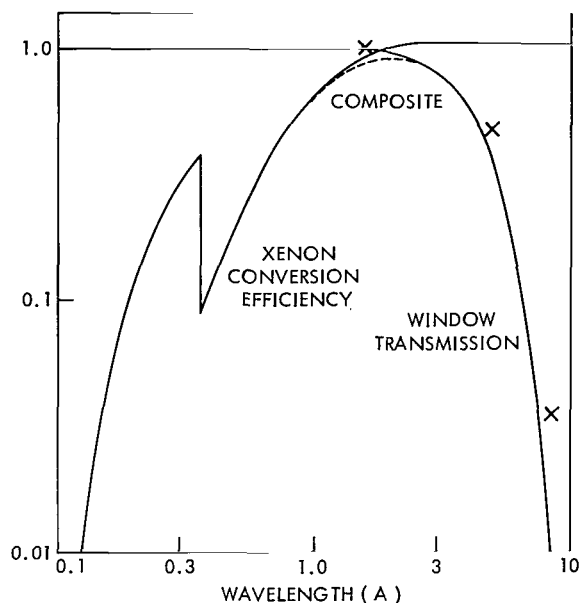


Figure 1—OSO-1 ion chamber conversion efficiency as function of wavelength: The solid line represents the theoretical values and the crosses experimental data.

INPUT SPECTRUM ASSUMPTIONS

Both of the full-scale flux values mentioned above are computed for an input spectrum shape equivalent to a $2.8(10)^6$ °K plasma. The basis for this choice is threefold:

1. A direct measurement of spectral shape between 7 and 11 Å was made by Pounds, Willmore, et al. (Reference 2) from the satellite Ariel (1962 σ1) on 27 April 1962, at 2110 UT, two hours prior to a small visible flare. The spectrum obtained by this group fits a $2.8(10)^6$ °K plasma; integrating their absolute flux values between 7 and 11 Å gives a value for the integral of $1.2(10)^{-3}$ ergs/cm²-sec. At this time the OSO-1 x-ray ion-chamber experiment was off-scale, implying an integrated flux over the same wavelength interval (that is, 7-11 Å) of $\geq 1.7(10)^{-3}$ ergs/cm²-sec⁻¹, for the same spectral distribution. The agreement between OSO-1 and Ariel for the solar x-ray flux of 27 April 1962 is thus probably within a factor of 2.

2. An assumed temperature appreciably less than $2.8(10)^6$ °K would require too high an electron density to produce the x-ray fluxes measured by OSO-1. This statement is true either if the x-ray source is spread uniformly over the entire corona or localized in centers of activity. If we compute the continuum flux to be expected at these wavelengths from the entire solar corona (assumed isothermal at a somewhat lower temperature, say $2.4(10)^6$ °K) we find that to produce the lowest flux value measured by OSO-1, the integral of the square of the electron density taken over

the entire corona is $55.3(10)^{49}$. This value should be compared with the value of $4.6(10)^{49}$ obtained by Shklovskii (Reference 3) using the coronal model of Allen (Reference 4), or with the value of $3(10)^{49}$ obtained by Elwert (Reference 5), (Reference 6). Thus the theoretical flux in the continuum for an isothermal corona with Allen's electron density profile at $2.4(10)^6$ °K falls short of the lowest value measured on OSO-1 by a factor of order 15. In fact, we must place the entire corona at a temperature in excess of $3.5(10)^6$ °K to meet the lowest OSO-1 flux using such an all-continuum model. If the contribution from line emissions were allowed to exceed the flux from continuum emission by a factor of 15, the corona in its entirety would have to be at a temperature of about $2.4(10)^6$ °K; but this, remember, is for the lowest flux measured by OSO-1. For more than 50 percent of the time the OSO-1 flux exceeded this lowest value by at least a factor of 10.

3. An assumed temperature appreciably greater than $2.8(10)^6$ °K would be inconsistent with concurrent OSO-1 observations of the Fe XV to Fe XVI ratio made by Neupert.*

SPATIAL DISTRIBUTION OF X-RAY SOURCES

From the fact that most of the time the measured flux from OSO-1 was much larger than the lowest value measured (which is already uncomfortably high for an isothermal corona with uniform density profile), we can only conclude that the previously observed spatial localization of sources of x-rays of somewhat longer wavelength must also exist for wavelengths less than 10 Å, and inquire as to the conditions of temperature and electron density likely to be found in such local densifications. The observations of Billings (Reference 8) show that occasionally temperatures as high as $4.2(10)^6$ °K and electron densities as high as $2(10)^{10}/\text{cm}^3$ are found; more usual values† run $T_e < 3.5(10)^6$ °K and $n_e < 7(10)^9/\text{cm}^3$.

SLOWLY VARYING COMPONENT

A comparison of the slowly varying part of the 10 Å x-rays with 2800 Mc radiation confirms that the localized sources of solar x-rays are in some way associated with centers of activity such as Ca plages and/or sunspot groups. Figure 2 shows the time history of both fluxes for about 2.5 solar rotations in the early life of OSO-1. It can be seen that the smoothed x-ray flux correlates fairly well with the excess 2800 Mc flux above a background of about 75 flux units appropriate for the "quiet" sun at that phase of the solar cycle (Reference 8).

The lowest x-ray flux (which may be considered an upper bound on the x-ray flux from the quiet sun) measured by OSO-1 (on 6 April 1962) for $\lambda < 8$ Å was $3.6(10)^{-5}$ erg/cm²-sec; for $\lambda < 11$ Å, $1.8(10)^{-4}$ ergs/cm²-sec. This flux occurred at a time when only 3 plages of area ≥ 1000 millionths of a solar hemisphere were visible on the disk. The nearest plage behind the west limb had set three days previously, and the nearest behind the east limb was not to rise until 1.5 days later. If we now assume that the x-ray emission is coming from 3 "pillbox" volumes, one associated

*See pages.

†D. E. Billings, Private communication.

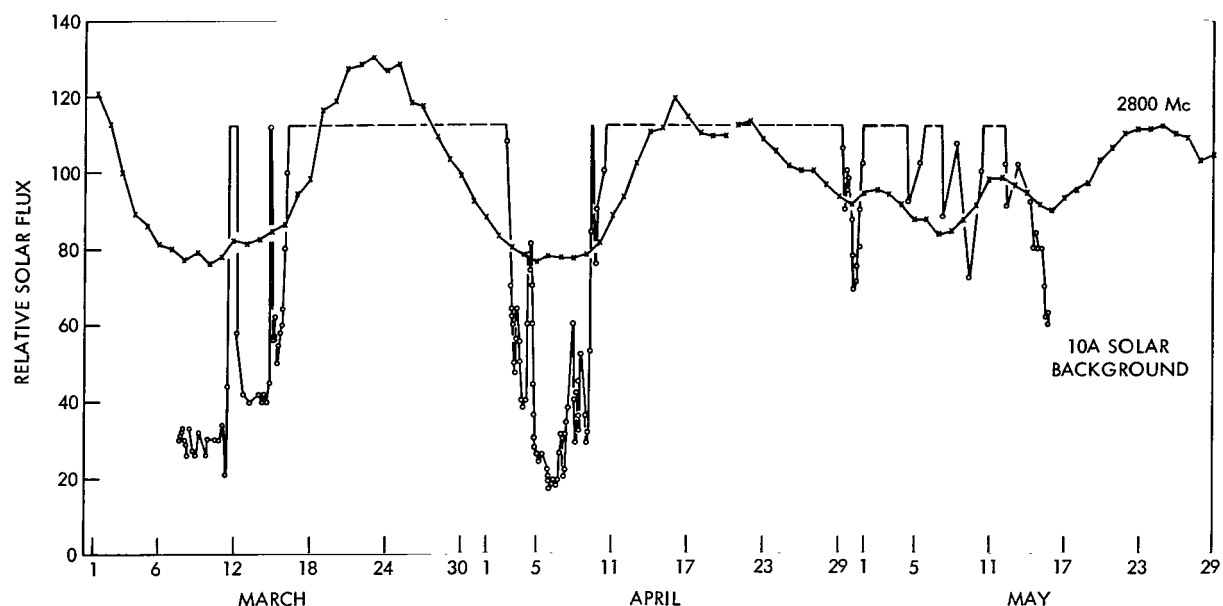


Figure 2—Slowly varying components of 2800 Mc solar flux and of $\lambda < 11 \text{ \AA}$ solar x-rays.

with each of the 3 plages, each having its base area equal to the plage area and furthermore having a height equal to one-half the diameter of its base, we have the situation shown in Table 2. Using the total source volume obtained from Table 2, Table 3 gives the value of $\int n_e^2 dv$ required to fit the observed x-ray flux of 6 April 1962 for several assumed temperatures, and shows the resulting values of n_e for various assumptions regarding the relative contribution of line emission (Reference 6). The volume above plage 6379 was observed by Billings* on 9 April 1962 to have a faint continuum enhancement from which he estimated $n_e = 0.5(10)^{10}$. If this was indeed the correct electron density, and if (as is most likely from such a weak source*) the electron temperature was not greater than $3.0(10)^6 \text{ }^\circ\text{K}$, Table 3 indicates the ratio of line emission to continuum emission was at least 10:1. If T_e was no greater than the $2.8(10)^6 \text{ }^\circ\text{K}$, the value obtained from the Ariel spectrum of 27 April, the ratio of line emission to continuum emission must have been around 30:1.

*D. E. Billings, Private communication.

Table 2
Plages for 6 April, 1962.

Observed Calcium Plage		Assumed X-Ray Source		
McMath Plage Number	Area (millionths of solar hemisphere)	Area (cm^2)	Height (cm)	Volume (cm^3)
6377	1600	$4.90(10)^{19}$	$3.95(10)^9$	$1.94(10)^{29}$
6378	1000	$3.06(10)^{19}$	$3.12(10)^9$	$0.954(10)^{29}$
6379	1000	$3.06(10)^{19}$	$3.12(10)^9$	$0.954(10)^{29}$
Total Volume				$3.85(10)^{29}$

X-RAY FLARES

Up to now we have discussed only the slowly varying component of the x-ray emission: in addition to these quasi steady-state conditions, transient events (x-ray flares) lasting usually from 10 minutes to a couple of hours were frequently observed. Such an event is shown in Figure 3, and should be compared with the quiet period of similar duration shown in Figure 4. The particular event of Figure 3 contains a total energy below 11 Å of $2(10)^{27}$ ergs.

Table 3
Electron Density for Plages of 6 April, 1962.

T_e (10^6 °K)	$\int n_e^2 dv$ (if a continuum)	n_e (10^{10} electrons/cm ³)			
		Ratio of line emission to continuum			
		1:1	3:1	10:1	30:1
2.4	$55.3(10)^{49}$	2.68	1.90	1.14	0.68
3.0	$11.9(10)^{49}$	1.25	0.88	0.53	0.32
3.5	$4.9(10)^{49}$	0.80	0.56	0.34	0.20

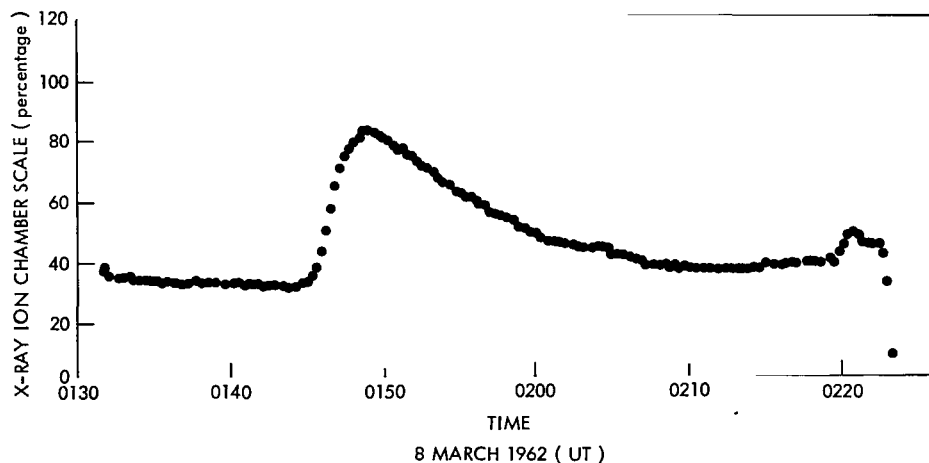


Figure 3—Typical small x-ray flare.

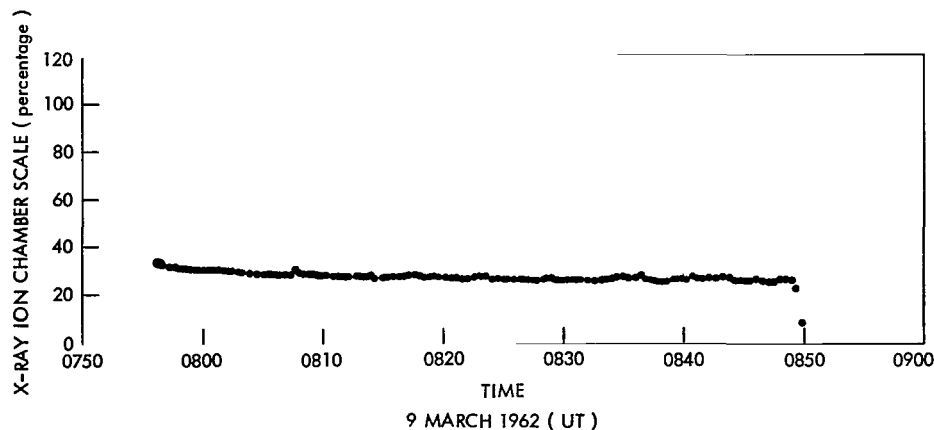


Figure 4—Typical "quiet" period.

Correlation with H- α Flares

During the 9 day interval between launch and March 16, 1962 (at which time the rising of plage 6370 on the east limb supplied enough x-ray emission to carry the experiment off-scale), approximately 60 x-ray flare events lasting from 10 minutes to 1 hour were seen, and 4 events were seen to last about 5 hours.

During this same interval (1620 UT 7 March 1962, to 1620 16 March 1962) some 33 H- α flares were reported by ground based observatories. Of these H- α flares, 6 would have been unobservable from OSO-1 for various reasons (satellite night, failure to command data storage readout, etc.). Of the remaining 27 H- α flares, 3 occurred while the x-ray experiment was still off-scale because of a previous large event. This leaves 24 H- α flares which can be tested for correlation with the x-ray flares. Of this group of 24, it appears that 11 correlate well, 3 definitely have no counterpart in x-rays, and the remaining 10 are doubtful because of insufficient data or an excessive time difference (greater than 10 minutes). Conversely, there are 6 full scale or greater x-ray events for which no H- α flare was reported even though observations were presumably being made at the time. Certainly more observations will be required before a definite statement can be made regarding a correlation or lack thereof between H- α flares and x-ray flares.

Correlation with SID's

In looking for correlations with Sudden Ionospheric Disturbances (SID), all x-ray events exceeding the full-scale saturation level were barely detectable (if observing conditions permitted) in Sudden Phase Anomaly (SPA) data for VLF transmissions via the D layer. Only the large event of 13 March was seen in ionospheric indices other than SPA's.

Correlation with 2800 Mc Transients

Correlation with transients in the 2800 Mc solar flux is good; but again, full-scale x-ray events are represented by extremely small events (1-2 flux units) in the 2800 Mc data.

Grouping of X-ray Flares

Several apparent associations of certain x-ray flares into groups displaying a definite pattern were observed; Figure 5 shows such a grouping. Similar groupings are present in the data for the first week in April; in fact, the one particular March group shown in Figure 5 has an exact April counterpart 27.1 days later with identical time separations between events and with identical peak excursions above mean background level. The envelope joining the peaks of the flares within a group is found: (1) to be a straight line, and (2) to have the same slope (with either positive or negative sign) from group to group.

These characteristics of the flare groups indicate a constant time-rate-of-change of x-ray source strength. Source strength is a function of electron density, of temperature, and of volume;

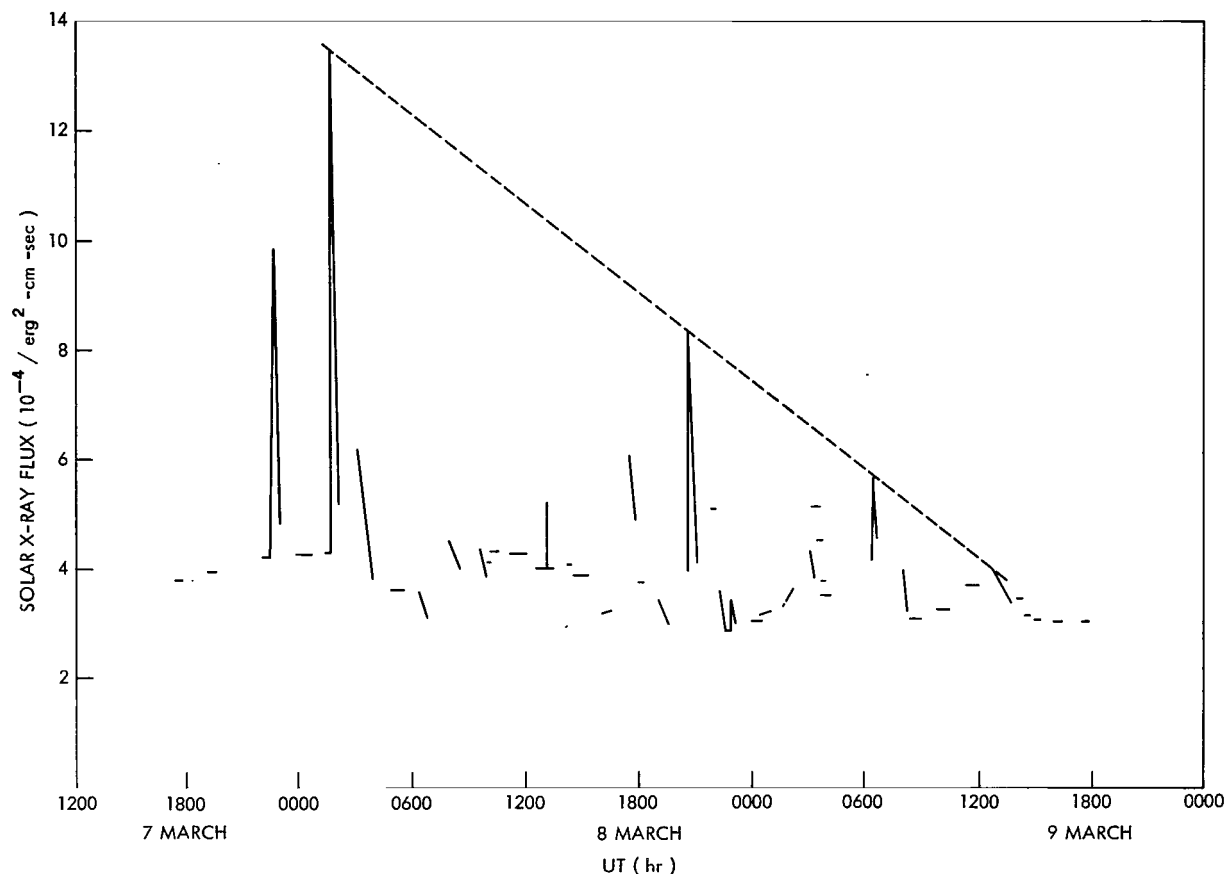


Figure 5—Solar x-rays for $\lambda < 11 \text{ \AA}$, 7-9 March 1962 showing grouping of the x-ray flares.

furthermore, it is difficult to see why any time variation of either electron density or temperature would be of such a particular non-linear nature as to constrain the source strength to vary linearly with time. We are left with the concept of a *volume* which is either growing or diminishing at a constant rate, and which on occasion serves as a reservoir of high-temperature electrons and ions interacting to produce the x-ray flares.

SUMMARY

A slowly varying component has been found in the solar x-ray flux below 11 \AA which correlates with the slowly varying component of the 2800 Mc solar radiation. A model for these quasi-stable x-ray sources which fits the OSO-1 data postulates localized sources having the same horizontal extent as Ca plages with thicknesses proportional to their diameter, and having an electron temperature of about $2.8(10)^6 \text{ }^\circ\text{K}$ and an electron density of about $5(10)^9 \text{ electrons/cm}^3$. For these conditions it is also necessary that the ratio of line emission to continuum emission be at least 10:1 and more probably 30:1.

In addition to a slowly varying component, transient events (x-ray flares) lasting from 10 min to a few hours were frequently observed. Correlation with SID's and with 2800 Mc transients has been obtained; correlation has been attempted with H- α flares with somewhat ambiguous results. X-ray flares were frequently observed to be associated in groups possessing a characteristic pattern; the concept of a source volume varying linearly with time is invoked to account for the linear envelope of a flare group.

ACKNOWLEDGMENTS

The author gratefully acknowledges the help of many of his associates at the Goddard Space Flight Center, and in particular, Alfred Stober and Robert Young who perfected the fabrication method for the ion chambers.

REFERENCES

1. Kreplin, R. W., Chubb, T. A., and Friedman, H., "X-Ray and Lyman-Alpha Emission from the Sun as Measured from the NRL SR-1 Satellite," *J. Geophys. Res.* 67(6):2231-2254, June 1962.
2. K. A. Pounds, A. P. Willmore, P. J. Bowen, K. Norman, and P. W. Sanford; *Proc. Roy. Soc.* (In Press).
3. Shklovskii, I. S., "The Ultraviolet Radiation and Soft X-Rays of the Sun," *Uspek. Fiz. Nauk*, 75:351-388, October 1961; Trans. in *Sov. Phys. - Uspek.* 4(5):812-834, March-April 1962.
4. Allen, C. W., "The Spectrum of the Corona at the Eclipse of 1940 October 1," *Roy. Astron. Soc. Mon. Not.* 106(2):137-150, 1946.
5. Elwert, G., "The Soft X-Radiation from the Undisturbed Solar Corona," (In German) *Z. Naturforsch.* 9a:637-653, July-August 1954.
6. Elwert, G. "Theory of X-Ray Emission of the Sun," *J. Geophys. Res.* 66(2):391-401, February 1961.
7. Billings, D. E., "Profile of the Yellow Coronal Line 5694," *Astrophys. J.* 125(3):817-821, May 1957.
8. Covington, A. E., and Harvey, G. A., "The Visibility of the 10-cm Radio-Emissive Region and Its Application in Finding the 10-cm Quiet Sun," *Astrophys. J.* 132(2):435-451, September 1960.

217/AV
CB

"The aeronautical and space activities of the United States shall be conducted so as to contribute . . . to the expansion of human knowledge of phenomena in the atmosphere and space. The Administration shall provide for the widest practicable and appropriate dissemination of information concerning its activities and the results thereof."

—NATIONAL AERONAUTICS AND SPACE ACT OF 1958

NASA SCIENTIFIC AND TECHNICAL PUBLICATIONS

TECHNICAL REPORTS: Scientific and technical information considered important, complete, and a lasting contribution to existing knowledge.

TECHNICAL NOTES: Information less broad in scope but nevertheless of importance as a contribution to existing knowledge.

TECHNICAL MEMORANDUMS: Information receiving limited distribution because of preliminary data, security classification, or other reasons.

CONTRACTOR REPORTS: Technical information generated in connection with a NASA contract or grant and released under NASA auspices.

TECHNICAL TRANSLATIONS: Information published in a foreign language considered to merit NASA distribution in English.

TECHNICAL REPRINTS: Information derived from NASA activities and initially published in the form of journal articles.

SPECIAL PUBLICATIONS: Information derived from or of value to NASA activities but not necessarily reporting the results of individual NASA-programmed scientific efforts. Publications include conference proceedings, monographs, data compilations, handbooks, sourcebooks, and special bibliographies.

Details on the availability of these publications may be obtained from:

SCIENTIFIC AND TECHNICAL INFORMATION DIVISION
NATIONAL AERONAUTICS AND SPACE ADMINISTRATION
Washington, D.C. 20546